

FABRICATION OF ROOM TEMPERATURE OPERATING LPG SENSOR BASED ON
 Fe_2O_3 -CNT COMPOSITE FILMS



A THESIS SUBMITTED IN PARTIAL FULFILLMENT
OF THE REQUIREMENT FOR THE DEGREE OF
DOCTOR OF ENGINEERING IN ELECTRICAL ENGINEERING
SCHOOL OF ENGINEERING
KING MONGKUT'S INSTITUTE OF TECHNOLOGY LADKRABANG

2021

KMITL-2021-EN-D-018-054

This material is reserved for educational use only, not allowed for commercial use.

Forbidden to modify the content, and cite the document when use.



COPYRIGHT 2021

SCHOOL OF ENGINEERING

KING MONGKUT'S INSTITUTE OF TECHNOLOGY LADKRABANG

This material is reserved for educational use only, not allowed for commercial use.

Forbidden to modify the content, and cite the document when use.

หัวข้อวิทยานิพนธ์	การประดิษฐ์เซ็นเซอร์วัดแอลพีจีที่อุณหภูมิห้อง โดยใช้ฟิล์มวัสดุผสม Fe ₂ O ₃ -CNT
นักศึกษา	นางสาวบัววรรณ ไชยงรัตน์
รหัสประจำตัว	60601159
ปริญญา	วิศวกรรมศาสตรดุษฎีบัณฑิต
สาขาวิชา	วิศวกรรมไฟฟ้า
พ.ศ.	2564
อาจารย์ที่ปรึกษาวิทยานิพนธ์	รศ.ดร.สุธิชัย ชัยสิทธิ์ศักดิ์

บทคัดย่อ

เซ็นเซอร์แอลพีจี เป็นอุปกรณ์ที่มีความสำคัญในการป้องกันอันตรายจากการเกิดไฟไหม้และการระเบิดของแก๊สแอลพีจี ฟิล์มบางวัสดุผสมเหล็กออกไซด์และคาร์บอนนาโนทิวป์ (Fe₂O₃-CNT) เป็นวัสดุที่ได้รับความสนใจนำมาสร้างเป็นเซ็นเซอร์ เนื่องจาก มีความไวสูง เวลาการตอบสนองและเวลาการคืนกลับสภาพเดิมรวดเร็ว สามารถวัดแก๊สได้ที่อุณหภูมิห้อง ในวิทยานิพนธ์นี้ นำเสนอการประดิษฐ์เซ็นเซอร์จากฟิล์มบางวัสดุ Fe₂O₃-CNT เพื่อใช้วัดแอลพีจีที่อุณหภูมิห้อง โดยใช้ฟิล์มบาง Fe-CNT เป็นวัสดุเริ่มต้น ข้อดีคือ Fe-CNT เป็นฟิล์มบางอยู่ก่อนแล้ว ซึ่งจะช่วยลดขั้นตอนการสร้างฟิล์มของ Fe₂O₃-CNT โดยฟิล์มบาง Fe-CNT สังเคราะห์ด้วยวิธีการเคลือบไอระเหยทางเคมีในแนวตั้งแบบโอทมอก ด้วยความร้อนที่อุณหภูมิ 950 องศาเซลเซียส จากนั้น นำฟิล์มบาง Fe-CNT ออบในบรรยากาศอากาศ เพื่อเปลี่ยน Fe เป็น Fe₂O₃ เครื่องมือที่ใช้ตรวจสอบลักษณะของฟิล์มประกอบด้วย เทคนิคเอ็กซ์เรย์โฟโตอิเล็กตรอนสเปกโทรสโกปี แสดงการเปลี่ยนโลหะเหล็กเป็นเหล็กออกไซด์ชนิดเฟสอัลฟา ผลเทคนิครามานสเปกโทรสโกปี แสดงคาร์บอนนาโนทิวป์เป็นแบบผนังชั้นเดียว ภาพกล้องจุลทรรศน์อิเล็กตรอนแบบส่องกราดและกล้องจุลทรรศน์อิเล็กตรอนแบบส่องผ่าน แสดงให้เห็นลักษณะสัณฐานวิทยาของฟิล์มบาง Fe-CNT คือ โครงตาข่ายคาร์บอนนาโนทิวป์โดยที่ผนังของคาร์บอนนาโนทิวป์จะยึดติดกับอนุภาคโลหะเหล็ก (ขนาดเฉลี่ย 7.33 นาโนเมตร) สำหรับพฤติกรรมทางความร้อนของฟิล์มถูกศึกษาโดยใช้เทคนิควิเคราะห์การสูญเสียน้ำหนักเชิงความร้อนและอนุพันธ์ความร้อนโน้มถ่วง (TGA/DTG) โดยศึกษาที่อุณหภูมิตั้งแต่ 150 องศาเซลเซียส ถึง 550 องศาเซลเซียส พบว่า ที่อุณหภูมิ 350 องศาเซลเซียส เป็นอุณหภูมิที่เหมาะสมในการเปลี่ยน Fe เป็น Fe₂O₃ และการอบที่อุณหภูมิดังกล่าวฟิล์ม Fe₂O₃-CNT มีค่าความต้านทานไฟฟ้าที่เหมาะสมในการนำไปสร้างเป็นเซ็นเซอร์ที่อุณหภูมิห้อง การเปรียบเทียบการสังเคราะห์ Fe₂O₃-CNT โดยกระบวนการแบบแห้งและแบบเปียก ผลจากภาพกล้องจุลทรรศน์อิเล็กตรอนแบบส่องผ่านแสดงให้เห็นว่าฟิล์มบาง Fe₂O₃-CNT ที่ได้จากกระบวนการแบบเปียกมีลักษณะสัณฐานวิทยาเป็นโครงสร้างคล้ายตาข่าย และฟิล์ม Fe₂O₃-CNT ที่ได้จากกระบวนการแบบแห้งมีโครงสร้างคล้ายกิ่งก้าน ผลกราฟกระแสและแรงดันของฟิล์ม Fe₂O₃-CNT หลังจากการอบอ่อนแสดงพฤติกรรมที่ไม่เป็นเชิงเส้น แสดงให้เห็นว่าเกิดเหล็กออกไซด์เกิดขึ้นบนพื้นผิวของคาร์บอนนาโนทิวป์ นอกจากนี้ กล้องจุลทรรศน์แรงอะตอมแสดงความขรุขระพื้นผิว (RMS) ของ Fe₂O₃-CNT มีค่าเพิ่มขึ้นตามจำนวน Fe-CNT

ผลการทดสอบเซ็นเซอร์ที่อุณหภูมิห้อง (28 องศาเซลเซียส) พบว่า เซ็นเซอร์ที่สร้างจาก ฟิล์มบาง $\text{Fe}_2\text{O}_3\text{-CNT}$ ซึ่งเตรียมด้วยกระบวนการแบบเปียก อบที่อุณหภูมิ 350 องศาเซลเซียส และจำนวน Fe-CNT ที่เวลาสะสมที่ 45 นาที แสดง ค่าการตอบสนองสูงสุด และเวลาในการตอบสนองและการคืนกลับสภาพเดิมเร็วที่สุด (ทดสอบด้วยแอลพีจีความเข้มข้น 5 vol.% , $S = \sim 5.5\%$, $T_{\text{resp.}} = 14 \text{ s}$, $T_{\text{rec.}} = 14 \text{ s}$) นอกจากนี้ เซ็นเซอร์สามารถตรวจจับความเข้มข้นของแอลพีจี ต่ำกว่าค่า 25% ของ สารไวไฟ (Lower Explosive Limit; LEL) โดยมีเวลาการตอบสนองและเวลาคืนกลับสภาพเดิมน้อยกว่า 30 วินาที จากผลการทดลองดังกล่าวนี้แสดงให้เห็นว่า ฟิล์ม $\text{Fe}_2\text{O}_3\text{-CNT}$ สามารถใช้งานได้ในการตรวจสอบแอลพีจี อย่างรวดเร็วที่อุณหภูมิห้อง



Thesis	FABRICATION OF ROOM TEMPERATURE OPERATING LPG SENSOR BASED ON Fe ₂ O ₃ -CNT COMPOSITE FILMS
Student	Miss. Buaworn Chaitongrat
Student ID.	60601159
Degree	Doctor of Engineering
Program	Electrical Engineering
Year	2021
Thesis Advisor	Assoc. Prof. Dr. Sutichai Chaisitsak

ABSTRACT

LPG sensor is the important device to prevent fire and explosion of LPG gas. Fe₂O₃-CNT hybrid thin films are promising candidates for gas sensor with high sensitivity, rapid response/recovery, and operating at room temperature. The search for the novel fabrication strategies of Fe₂O₃-CNT hybrid thin films is one alternative to improve gas-sensing performance. This dissertation presents the fabrication of Fe₂O₃-CNT composite films as LPG sensors for operating at room temperature. Fe₂O₃-CNT thin films were successfully produced by using the Fe-CNT as a primary material and then annealed in air. This primary material is already originated as thin films that help reduce the thin films' fabrication procedure. Transmission Electron Microscopy (TEM) and Field-emission Scanning Electron Microscopy (FE-SEM) images represented that primary films consisted of randomly oriented entangled CNTs and were adhered with Fe nanoparticles (average particle size of ~7.33 nm). CNTs and Fe₂O₃ with alpha (α) phase were confirmed by Raman spectroscopy and X-ray Photoelectron Spectroscopy (XPS), respectively. The thermal behavior of mixed powders was characterized by thermogravimetric analysis and derivative thermogravimetric analysis (TGA/DTG) to obtain the calcination temperature range. For various annealing temperatures, at 350°C was the optimum annealing temperature for the transformation of metallic Fe to Fe₂O₃ with high purity of CNTs. The optimum synthesis process of Fe₂O₃-CNT thin films was the wet process when compared with the dry process (without any using solution). FE-SEM presents that the surface morphology of Fe₂O₃-CNT films obtained in the wet process was the mat-like structure and obtained in the dry process was the branch-like structure. Moreover, I-V curves for both dry-transferred and wet-transferred films after annealing showed the nonlinear behavior. This behavior also indicates that Fe₂O₃ formed on CNT surfaces and caused high resistance for both dry-transferred and wet-transferred films after annealing. The surface morphology (RMS roughness) was further investigated through Atomic Force

Microscopy (AFM). RMS of Fe₂O₃-CNTs thin films increased with an increased deposition time of Fe-CNT films (controlling by mist-CVD method).

For the sensor test at operating room temperature (28°C), Fe₂O₃-CNT films were prepared with the wet process, annealing at 350°C, and deposition time at 45 minutes. This sensor showed the highest sensitivity and the fastest response and recovery times (to 5 vol.% of LPG, S = ~5.5%, T_{resp.} = 14 s, T_{rec.} = 14 s). Moreover, the sensor could detect LPG concentration at a lower value than 25% of LEL with a response and recovery time of less than 30 seconds at room temperature. Furthermore, these results indicate that the Fe₂O₃-CNT films possible applications in fast LPG monitoring at room temperature.



ACKNOWLEDGEMENT

First of all, I gratefully acknowledge the financial support for this work provided by the Higher Education Research Promotion and National Research University Project of Thailand, Office of the Higher Education Commission, and Udon Thani Rajabhat University.

I am very thankful to my thesis advisor, Assoc. Prof. Dr. Sutichai Chaisitsak for providing guidance and feedback throughout this project. I am also grateful to Western Digital (Thailand) for the Raman measurements.

Finally, I would like to express my greatest thanks to my family for their encouragement and support.

Buaworn Chaitongrat



TABLE OF CONTENTS

	Page
THAI ABSTRACT	I
ENGLISH ABSTRACT	III
ACKNOWLEDGEMENT	V
TABLE OF CONTENTS	VI
LIST OF TABLES	VIII
LIST OF FIGURES.....	IX
CHAPTER 1 INTRODUCTION	1
1.1 Motivation.....	1
1.2 Objective.....	3
1.3 Scope of Research.....	3
1.4 Expectation.....	3
CHAPTER 2 LITERATURE REVIEW	4
2.1 Liquefied Petroleum Gas	4
2.1.1 Flashpoint.....	4
2.1.2 Auto-ignition temperature:.....	4
2.1.3 Lower Explosive Limit (LEL).....	4
2.1.4 Upper Explosive Limit (UEL).....	5
2.2 Gas Sensor	5
2.2.1 Gas-sensing properties	6
2.2.2 Gas measurement systems.....	7
2.3 Carbon Nanotubes.....	8
2.3.1 Properties of CNTs	10
2.3.2 CNT synthesis.....	12
2.3.3 Sensing mechanism	13
2.4 Iron oxide.....	13
2.5 MOx-CNT films.....	16
2.5.1 Synthesis of MOx-CNT films.....	16
2.5.3 Sensing mechanism	18
2.6 Characterization	20
2.6.1 Atomic Force Microscopy.....	20
2.6.2 Raman Spectroscopy.....	21

2.6.3 X-Ray Photoelectron Spectroscopy.....	23
2.6.4 Field Emission Scanning Electron Microscopy.....	24
2.6.5 Thermogravimetric Analysis.....	25
CHAPTER 3 RESEARCH METHODOLOGY.....	26
3.1 Synthesis of Fe-CNT films.....	26
3.1.1 Precursor preparation.....	26
3.1.2 Mist-CVD procedures.....	26
3.2 Transfer method.....	29
3.3 Synthesis of Fe ₂ O ₃ -CNT films.....	30
3.4 Comparison with purified CNT films.....	31
3.5 Sensor testing system.....	32
CHAPTER 4 RESULTS AND DISCUSSION.....	34
4.1 Materials.....	34
4.1.1 As grown Fe-CNT films.....	34
4.1.2 Dry and wet methods.....	35
4.1.3 Various temperature annealing.....	41
4.1.5 Comparison with purified CNTs.....	48
4.2.3 Effect of various deposition Times.....	52
4.2.4 Comparison with purified CNTs.....	54
4.2 LPG gas sensing properties.....	50
4.3 LPG sensing mechanism.....	56
4.4 Comparison with other sensors.....	58
CHAPTER 5 CONCLUSIONS.....	60
REFERENCES.....	64
Appendix A.....	74
Appendix B.....	75
Appendix C.....	76
Appendix D.....	77
AUTHOR BIOGRAPHY.....	78

LIST OF TABLES

Table	Page
2. 1 Flammability and explosion properties of selected substances.....	5
4. 1 Nanocomposite material-based LPG sensors operating at room temperature.....	58



LIST OF FIGURES

Figure	Page
2.1 The resistance changes of n-type semiconducting materials during exposure to reducing gases.....	6
2.2 Schematic of sensor testing methods: Flow-through method.....	8
2.3 Schematic of sensor testing methods: Static environment method.....	8
2.4 Structures of (a) a single-walled carbon nanotube with a diameter of 0.5 to 1.5 nm, and (b) a multi-walled carbon nanotube consist of three graphitic sheets with a diameter rather than 100 nm.....	9
2.5 Schematic structure of different configurations of the graphene lattice with chiral vector	9
2.6 Schematic representation of adsorption sites on (a) single carbon nanotubes and (b) carbon nanotube bundles.....	12
2.7 NH ₃ sensing-mechanism of CNT sensors	13
2.8 Typical FE-SEM images of various α -Fe ₂ O ₃ nanostructures.....	14
2.9 Schematic representation of the sensing mechanism of n-type MOx nanostructures under reducing gases.....	15
2.10 Schematic diagram of the spin coating process.....	17
2.11 The screen-printing process.....	17
2.12 (a) SEM image of CNTs decorated with discrete SnO ₂ nanoparticles and (b) analyte gas interaction and charge transport in a CNT-SnO ₂ network. The red dotted line represents the direction of current between electrodes.....	18
2.13 (a) FE-SEM image of a high-concentration hybrid SWNTs/SnO ₂ sensor and (b) a schematic diagram of a hybrid SWNTs/SnO ₂ gas sensor, SWNT bundles are embedded in SnO ₂ -based materials.....	19
2.14 (a) Schematic illustration of an atomic force microscope and (b) Photograph of atomic force microscope AFM XE-100.....	21
2.15 Raman characterization of SWNT; radial breathing mode (RBM) peak at $\sim 100\text{--}350\text{ cm}^{-1}$, G mode at $\sim 1582\text{ cm}^{-1}$, and D mode at $\sim 1350\text{ cm}^{-1}$	22
2.16 Photograph of the Raman spectroscopy (Renishaw inVia Reflex) at Western Digital Thailand.....	23
2.17 Photoelectric effects.....	23
2.18 Photograph of XPS machine.....	24

2.19	Photograph of a scanning electron microscope.....	25
2.20	Photograph of thermogravimetric analyzer (Perkin Elmer; Pyris 1)	25
3.1	Schematic diagram of ethanol-ferrocene precursor solutions preparation process of (a) ethanol solution, (b) ferrocene powder, and (c) ferrocene powder was dissolved in the ethanol solution. For mixing the solution, the solution was ultrasonically stirred for 30 minutes.	27
3.2	(a) Schematic diagram and (b) photographic images of the mist-CVD system used for the synthesis of Fe-CNT films.	28
3.3	Temperature profile in the furnace of the mist-CVD process for the synthesis of Fe-CNT films at 950°C.	28
3.4	As-grown films (Fe-CNT films) on filter membranes after synthesized by mist-CVD method (Deposition time; 15, 30, 45, 60, 90, and 120 min).	29
3.5	Schematic diagram of the dry transfer and wet transfer method. As-grown films (Fe-CNTs) on the membrane filter were transferred onto the substrate by (a) the dry transfer method (the pressing onto a substrate and pilling-off) and (b) the wet transfer method (pressing onto a substrate and removing the membrane filter with dissolving in acetone solutions for 48 h). Subsequently, both dry-transfer film and wet-transfer film were annealed in air at 350°C to create Fe ₂ O ₃	30
3.6	Photograph of 47900 furnaces 950°C was used for annealing of films.	31
3.7	Photograph of films before and after annealing at various temperatures in air. (a) non-annealing, (b) 150 °C, (c) 250 °C, (d) 350 °C, (e) 450 °C, and (f) 550 °C.	31
3.8	Schematic diagram of purification of purified CNTs.	31
3.9	Comparison photograph of (a) Fe-CNTs, (b) Fe ₂ O ₃ -CNTs, and (c) purified CNTs.....	32
3.10	(a) Sensor structure and (b) photograph of Fe ₂ O ₃ -CNT films based on sensors.	33
3.11	Schematic of sensor testing methods.....	33
4.1	(a) Photograph, (b) FE-SEM image, and (c) TEM image of as-grown (or Fe-CNTs) films on the membrane filter.....	34
4.2	Before annealing, (a) typical photograph of as-grown films on glass substrate after transfer process. FE-SEM images of (b) the dry-transferred and (c) wet-transferred (Fe-CNT) films.	35

4.3	After annealing, (a) photograph of Fe ₂ O ₃ -CNT films on substrate. FE-SEM images of (b) the dry-transferred and (c) wet-transferred (Fe ₂ O ₃ -CNT) films.....	36
4.4	XPS spectra for C 1s states. Wet-transferred and dry-transferred films (a) before annealing (Fe-CNT) and (b) after annealing (Fe ₂ O ₃ -CNT).	38
4.5	XPS spectra for Fe2p states. Wet-transferred and dry-transferred films (a) before annealing (Fe-CNT) and (b) after annealing (Fe ₂ O ₃ -CNT).	39
4.6	XPS spectra for O1s states. The wet-transferred and dry-transferred films (a) before annealing (Fe-CNT) and (b) after annealing (Fe ₂ O ₃ -CNT).	40
4.7	Typical I-V characteristic of (a) the dry-transferred and wet-transferred (Fe-CNT) films and (b) the dry- transferred and wet- transferred films (Fe ₂ O ₃ -CNT).	41
4.8	Thermal analysis curves (TGA-DTG) of as-grown (Fe-CNT) films.....	42
4.9	Typical FE-SEM image of the as-grown (Fe/CNTs) films at various annealing temperatures.	43
4.10	Raman spectra ($\lambda_{ex.} = 532 \text{ nm}$) of Fe-CNT films annealed at various annealing temperatures (non-annealed, 150°C, 250 °C, 350°C, 450°C, and 550°C).	44
4.11	Typical surface morphologies of (a) as-grown (Fe-CNT) films and (b) Fe ₂ O ₃ -CNT films on silicon substrates.....	46
4.12	Typical AFM images of the Fe ₂ O ₃ -CNT films prepared with the various deposition times. The 3D images were recorded in a 5 $\mu\text{m} \times 5 \mu\text{m}$ planar in contact mode.....	47
4.13	Morphology of (a) Fe-CNT films, (b) Fe ₂ O ₃ -CNTs), and (c) purified CNTs).	48
4.14	Raman spectra of the samples.....	49
4.15	Comparison of the response of the dry and wet-transferred Fe ₂ O ₃ -CNTs film sensors to 5% of LPG at room temperature.	50
4.16	(a) Typical dynamic resistance curves and (b) corresponding sensor response of sensors annealed at various temperatures (from top-to-bottom: Fe-CNTs (non-annealed), 250°C, and 350°C) in 5 vol.% of LPG.....	52
4.17	Sensing performances of Fe ₂ O ₃ -CNT films prepared under various deposition times of 15, 30, 45, 60 and 90 min.....	53
4.18	Dynamic responses of Fe ₂ O ₃ -CNT films to LPG concentrations varying from 0.1–0.7 vol.%.	54

4.19	Summary of the sensing properties of Fe ₂ O ₃ -CNT films to LPG concentrations varying from 0.1–0.7 vol.%	54
4.20	Dynamic responses of (a) Fe-CNT films, (b) Fe ₂ O ₃ -CNT films, and (c) purified CNTs, to LPG in air atmosphere, and, (d) Sensor responses of various sensor types to concentrations of LPG from 1–5 vol.%.....	56
4.21	Sensing mechanisms of (a) CNTs decorated with discrete Fe ₂ O ₃ particles and CNTs covered with Fe ₂ O ₃ particles.....	58



CHAPTER 1

INTRODUCTION

1.1 Motivation

Liquefied petroleum gas (LPG) is a complex mixture of hydrocarbons, mostly propane (C_3H_8) and butane (C_4H_{10}). LPG is widely used as a fuel in heaters, cooking equipment, and automobiles. Additionally, LPG is one of the most dangerous gases due to its flammable and explosive nature, which makes it potentially quite hazardous to people and the environment. To avoid gas explosions, there is constant need to detect LPG leak while they are below the explosive limit (~ 2.0 vol.% of LPG) [1]. In last few decades, metal oxide (MOx) gas sensing materials have been extensively used as LPG sensors, which have many advantages such as high response (sensitivity), low cost, simple design and compact size [2-4]. Nevertheless, they usually require a sensor heater to perform at their optimal sensing properties to reach operating temperature of 200°C – 500°C [2, 5-7], causing increased power consumption, complexity and higher operating costs. Therefore, LPG sensors were continuously developed and improved for lower working temperature or even room temperature. Moreover, removing the heater from MOx sensors decreases power consumption and reduces the number of fabrication steps and which results in portable and miniaturized gas sensors, and extend their range of applications such as wearable devices and mobile terminals.

Reductions in operating temperature of gas sensor have been successfully done by reducing MOS in nanostructure, new materials, and mixing materials. Hybrid nanomaterials based on MOx and carbon nanotubes (CNTs) are one of the most hybrid materials interested in researchers due to the generating of further properties between MOx and CNTs, such as the electrical conductivity, the porosity, and heterojunction generation in sensing materials [7]. Thus, the MOx-CNT hybrid materials have a higher sensing performance (high response, high selectivity and low-operating temperature) when compared to the sensor fabricated using a single-material sensor [8-10]. For example, Muthukumaran et al. [10] reported an ammonia gas sensor using Fe_2O_3 -CNTs. They found that this material has a higher response than pristine CNTs, at room temperature [10]. MOx-CNT composites-based sensors can be fabricated by both the dry and wet processes. The typical dry process involves synthesizing CNTs and mixing with MOx nanoparticles by plasma treatment and thermally evaporated [8]. Typical

wet-process for fabricating hybrid material-based sensors consists of the MOx-CNT combination by probe sonication and magnetic stringing, film coating process, and heat treatment [5]. MOx-CNTs in a liquid are usually coated onto a substrate with spin-coating, screen-coating, and spray-coating. However, Andio et al. [11] found that the aggregation of metal oxide nanoparticles in hybrid films occurred during the coating process, leading to a decrease in the active sites, subsequently decreasing their sensitivity. The search for the suitable fabrication strategies of MOx-CNT hybrid materials is one alternative to improve gas-sensing performance operating at room temperature. However, there are no reports available on the comparison of dry- and wet- processes of Fe₂O₃-CNT hybrid materials.

Particularly, the mixing materials of carbon nanotubes (CNTs) and MOx have attracted much attention to improve the gas sensing performances such as sensitivity, selectivity, response speed. Due to their unique physical and chemical properties [12]. These include such conductance changes, increased surface reaction sites, and the interface between MOx and CNTs [12]. Various methods are used to synthesize MOx-CNTs composite. This includes surfactant wrapping sol-gel method, in situ chemical vapor deposition (CVD) synthesis route, high-intensity ultrasonic radiation method, chemical precipitation and controlled hetero-aggregation method [13]. These methods are popular with researchers due to their simplicity and cost comparing to others. Subsequently, composite materials are coated as films onto a substrate using a variety of techniques, including spin-coating, drop-coating, screen-printing, and dip-coating. However, MOx-CNTs composite will be closely grouped together during the films coating process which is disadvantage for gas diffusion in them [2]. The surface morphologies of sensing materials is significantly by the synthesize MOx-CNTs composite. According to our mist-CVD [14], which has attracted much attention for use in the synthesis of CNTs to achieve networks of CNT films. Fe catalyst particles adhere to as-grown CNTs are usually found after synthesis CNTs. CNTs films are directly coated onto a glass substrate without those coating techniques. These as-grown CNTs with Fe can be easily synthesized as Fe₂O₃-CNT composite materials via air annealing.

This dissertation reports the simple fabrication and fast-LPG gas sensing performance at operating room temperature of Fe₂O₃-CNT nanocomposite films. The vertical floating catalyst chemical vapor deposition method is used to prepare Fe₂O₃-CNT films because they are simple, inexpensive, and suitable for large-scale production. In the mist-CVD process, both metal-Fe particles and the CNT were simultaneously synthesized with the adhesion of Fe on the wall of CNTs. Moreover, Fe-CNT thin films

are formed and coated on substrates by self-assembly during CVD-processed, without any coating method. Subsequently, metallic-Fe particles on CNTs were changed into α -Fe₂O₃-CNT via annealed in air. The sensing performance of Fe₂O₃-CNT films shows significant high sensitivity, and fast response/recovery times, compared with the purified CNT films. Fe₂O₃-CNT films showed that it could detect LPG concentration at lower value than 25% of LEL with response/recovery time of less than 30 seconds at room temperature. These results suggest that the Fe₂O₃-CNT films are challenging materials for monitoring LPG operating at room temperature. Furthermore, the effect of deposition time, temperature annealing, and sensing mechanism of Fe₂O₃-CNT films on LPG sensing are investigated in this dissertation.

1.2 Objective

1.2.1 To study the prepared conditions while the synthesis of Fe₂O₃-CNT films via the vertical floating catalyst chemical vapor deposition method.

1.2.2 To characterize the properties of Fe₂O₃-CNT films using the transmission and scanning electron microscopy, and X-ray photoelectron spectroscopy.

1.2.3 To fabricate sensing layer of Fe₂O₃-CNT films for LPG sensor device.

1.2.4 To measure the LPG-sensing performance of Fe₂O₃-CNT films sensor at operating room temperature.

1.3 Scope of Research

1.3.1 Study the influence of prepared conditions while the synthesis of Fe₂O₃-CNT films via the vertical floating catalyst chemical vapor deposition method.

1.3.2 Fabricate sensing films of Fe₂O₃-CNTs for LPG sensor application.

1.4 Expectation

1.4.1 Understand the principle and method of the vertical floating catalyst chemical vapor deposition method to synthesize the Fe₂O₃-CNT nanostructure.

1.4.2 Understand the preparation parameters that affect to the structural property of Fe₂O₃-CNT via the vertical floating catalyst chemical vapor deposition method.

1.4.3 Understand the thin film fabrication technique to prepare Fe₂O₃-CNT film as sensing layer of the LPG sensor.

1.4.4 Understand the sensing mechanism of Fe₂O₃-CNT LPG sensor device.

CHAPTER 2

LITERATURE REVIEW

2.1 Liquefied Petroleum Gas

Liquefied Petroleum Gas (LPG) is produced during the refining of crude oil and through the natural gas separation process. The component gases are readily liquefied under pressure at atmospheric temperatures and are used in the vapor phase as a fuel with air or oxygen. LPG is a flammable mixture of hydrocarbon gases, mostly propane (C_3H_8) and butane (C_4H_{10}). It provides a high heating value and a clean environmentally friendly energy that is low cost and easily transported in various sized pressure vessels. Thus, LPG is widely used as a fuel in heaters, cooking equipment and automobile. However, it is very flammable. Its combustible gases can vigorously burn and cause explosion. Evaluating the hazardous potential of a combustible gas is based on the following considerations of properties of combustible gases [15].

2.1.1 Flashpoint

The flashpoint is defined as the minimum temperature at which a substance generates a sufficient amount of vapor to ignite near the surface of the liquid. More flammable liquids have lower flashpoints.

2.1.2 Auto-ignition Temperature:

The auto-ignition point refers to the minimum temperature at which a chemical will spontaneously ignite in a normal atmosphere with no external ignition source. Normally, ignition results from an electrical spark, static spark, or contact with hot surfaces.

2.1.3 Lower Explosive Limit (LEL)

Lower Explosive Limit (LEL) is defined as the minimum concentration of a flammable gas that will explode if an ignition source is introduced in its vicinity.

Table 2. 1 Flammability and explosion properties of selected substances [16, 17].

Material	Flash Point (°C)	Auto ignition (°C)	Lower Limit (% vol. in air)	Upper Limit (% vol. in air)
Butane	N/A (Gas)	365	1.6	8.4
Propane	N/A (Gas)	470	2.1	9.5
Methane	N/A (Gas)	595	5	15
Ethane	N/A (Gas)	515	2.7	15.5
Ethanol	-11	425	3.1	20
Methanol	11	470	5.5	36.5
Acetone	-18	400	2	12

2.1.4 Upper Explosive Limit (UEL)

An Upper Explosive Limit (UEL) is defined as the maximum concentration of a gas that will burn in the air. The National Institute for Occupation Safety and Health (NIOSH) and the Occupational Safety and Health Administration (OSHA) are agencies that determined the LEL of propane as 2.1% and butane 1.6% gas (%vol. air). The UEL of propane and butane are 9.5 % and 8.4 % gas in air (%vol. air), respectively, as shown in Table 2. 1.

2.2 Gas Sensor

Gas sensors [18] or gas detectors, are sensing devices that measure the concentration of gases in the environment, as well as in factories, laboratories, hospitals and in numerous technical installations. The concentration of gases can be measured via converting changes in physical or chemical properties into electric signals.

Various types of gas sensors developed so far and their working principles such as solid state sensor (i.e., chemiresistive and chemical field effect transistors (FET)) , mass sensitive sensors, and optical sensors [18]. Among these, semiconductor-based chemiresistors sensors are the most attractive used to detect combustible and toxic gases due to their inexpensive and simple fabrication methods. The principle of chemiresistive gas sensors is measurement of a change in electrical resistance due to an interaction between the semiconductor materials and a gas. Other benefits of semiconductor sensors are their high sensitivity to a range of gases, operating speeds and small sizes.

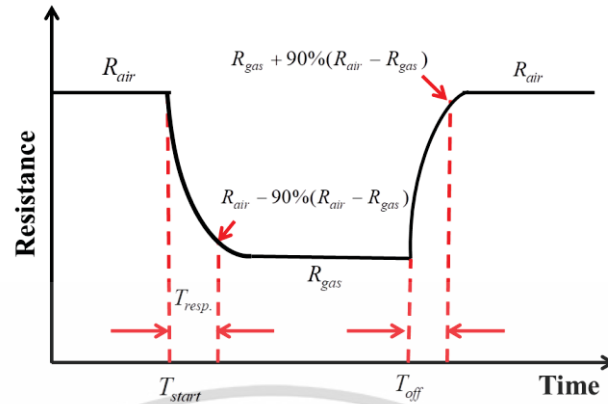


Figure 2.1 The resistance changes of n-type semiconducting materials during exposure to reducing gases.

2.2.1 Gas-sensing properties

A sensing device's basic operating parameters are sensitivity (or sensor response), response and recovery times and selectivity. These parameters are further discussed below.

Sensitivity (or sensor response)

Sensitivity (S) is a change of measured signal per unit of gas concentration measured [19]. Sensitivity (or response) is defined using several ratios depending on the type of a semiconductor (n- or p-type), and the analyte gas (oxidizing or reducing gases). In this experiment, the sensitivity of sensors can be defined as follows:

$$S(\%) = \frac{|\Delta R|}{R_g} \times 100 \quad (2.1)$$

$S(\%)$ is the percent sensor response. ΔR is $R_a - R_g$, where R_g and R_a denote the electric resistance value of sensors when exposed to LPG gas and a N_2 (or zero air), respectively [20-23].

Response time

Response time is defined as the sensor's time to respond to a step concentration change from zero to a specific level [19, 24]. Typically, the response times can vary from a few seconds to a few minutes. Up to 5 min may be acceptable, but this may be too long if the time exceeds 10 min. $T_{resp.}$ is defined as the time required until 90 % of the response signal is achieved, as illustrated in Figure 2.1 [20].

Recovery time

The recovery time is the time that elapses before a sensor is ready to be used for another measurement [24]. The resulting response time may be immediate, or it may require some time interval to allow the sensor system to return to a base equilibrium before it can make the next reading. Short response and recovery times are indicative of good operating sensor performance. Normally, the recovery time, T_{rec} denotes the time needed until 90 % of the original baseline signal is recovered. The response and recovery time can be calculated as follows:

$$T_{resp.} = T_{start} - T_{[R_{air} - 90\%(R_{air} - R_{gas})]} \quad (2.2)$$

$$T_{rec} = T_{off} - T_{[R_{gas} + 90\%(R_{air} - R_{gas})]} \quad (2.3)$$

Selectivity

Selectivity is defined as a sensor's ability to respond primarily to only one species in the presence of other species [18, 24]. This factor is the essence of all sensors. It is difficult to find a sensor, which will respond to only one analyte, although some exist. It is more frequent to find a sensor selective for one analyte, with a limited sensitivity for other similar analytes.

2.2.2 Gas measurement systems

Figure 2.2 shows the gas measurement systems that are widely used to investigate of sensing-performance of the LPG sensor.

(a) Flow-through method: This method's concept is schematically shown in Figure 2.2. The resistance changes are recorded under a continuous flow of a known concentration of analyte gas. The concentration of the analyte gas (Gas-1) is mixed in the desired concentration with the carrier gas Nitrogen or inert gas (Gas-2) using a mass-flow controller (MFC). Subsequently, the flow of the analyte gas is closed to measure

the recovery times of sensors. This method's advantage is that the sensor response can be recorded repeatably as a function of various concentrations.

(b) Static environment method: The sensor is placed inside an enclosed test chamber of a known volume, as depicted in Figure 2.3. A known amount of gas is injected into the chamber of the apparatus using a micro-syringe to measure the sensor resistance to the analyte gas's concentration. The resistance of the sensor as a function of time is measured until steady-state is achieved. The recovery of the sensor is studied by removing the sensor from chamber and exposing it to air.

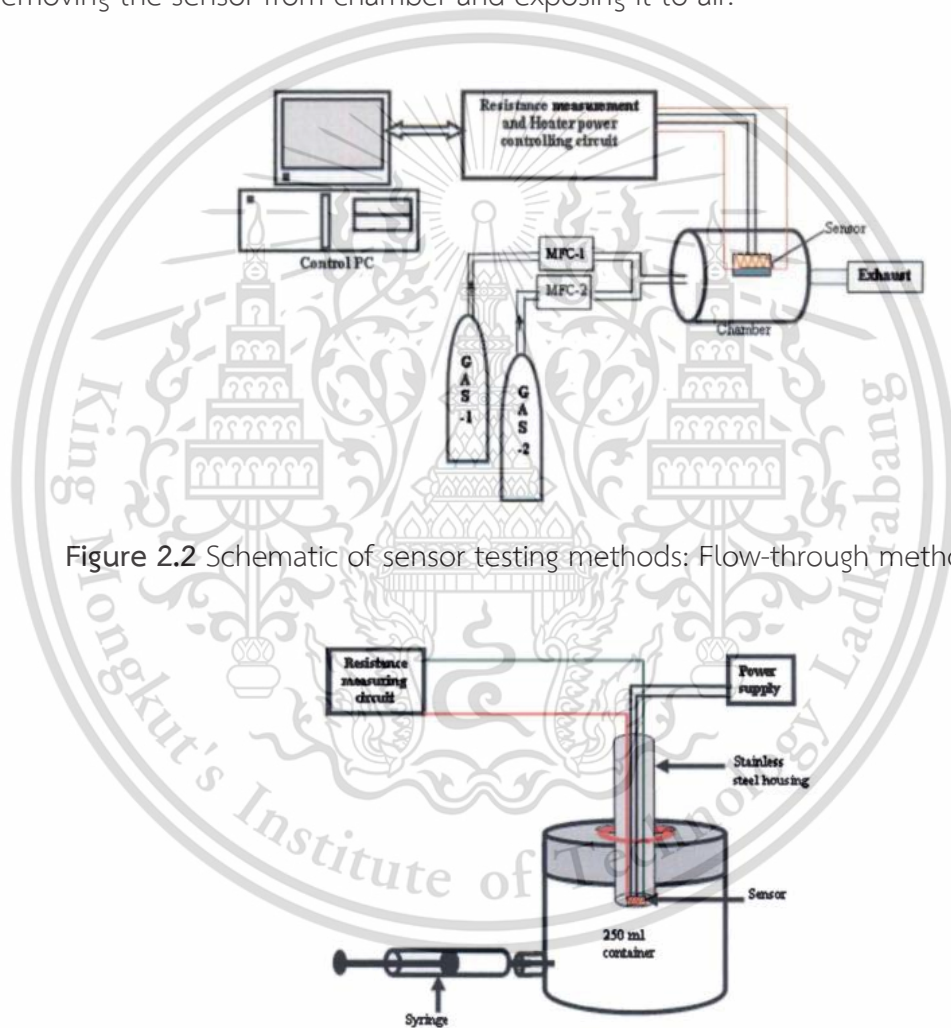


Figure 2.2 Schematic of sensor testing methods: Flow-through method.

Figure 2.3 Schematic of sensor testing methods: Static environment method.

2.3 Carbon Nanotubes

Carbon nanotubes (CNTs) were discovered and described by S. Iijima of Japan, in 1991 [25]. CNTs have been attracted much attention for applications in various devices

such as field emitters [26], gas storage, separation [27], nano probes [28], gas sensors [29], high strength composites [30], and fuel cells [31]. This is due to their high conductivity, high thermal stability, and high surface area. Types of carbon nanotubes are depicted in Figure 2.4. Single-walled carbon nanotubes (SWCNTs) (Figure 2.4 (a)), consisting of a single graphene layer wrapped to form a hollow cylinder. The other type of nanotubes is multi-walled carbon nanotubes or MWNTs (Figure 2.4 (b)) are made of a large number of concentric cylindrical graphene shells.

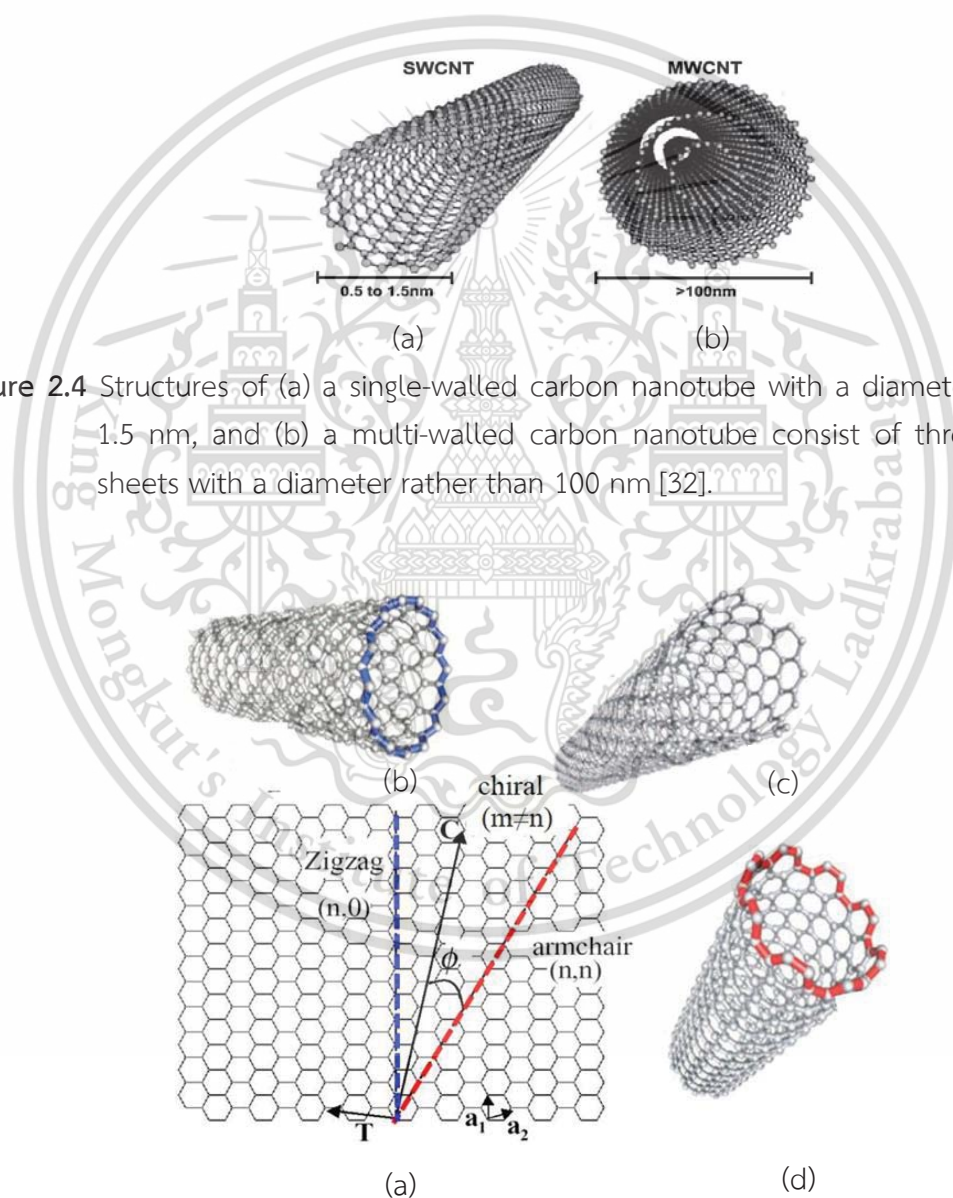


Figure 2.4 Structures of (a) a single-walled carbon nanotube with a diameter of 0.5 to 1.5 nm, and (b) a multi-walled carbon nanotube consist of three graphitic sheets with a diameter rather than 100 nm [32].

Figure 2.5 Schematic structure of different configurations of the graphene lattice with chiral vector [33].

CNTs can be classified into three types; armchair, zigzag and chiral carbon nanotubes. The difference in these carbon nanotubes depend on how the graphene sheets are formed into a tube. Figure 2.5 shows the rolling direction (or chiral vector) of a graphene sheet [34]. The chiral vector is explained by the pair of integers (n, m). When m=0, the nanotube is called zigzag, when n=m, the nanotube is called armchair, and all other configurations are chiral.

2.3.1 Properties of CNTs

Thermal stability of CNTs [35]

Carbon nanotubes were found to withstand high temperatures, relative to most organic carbon forms. Wei et al. [36] investigated the thermal stability of multiwall carbon nanotubes in a high vacuum. Their results indicated that MWNTs with a 60-nm-diameter could withstand temperatures of up to 3400 K. Xu et al. [37] reported that CNTs were more thermally stable when they had diameters of 60-100 nm. CNTs with diameters of less than 60 nm had decreased thermal stability. However, Peng et al. [38] indicate that 0.4 nm diameter CNTs could withstand temperature as high as 1,100°C in a vacuum. Under oxidizing conditions, Bom et al. [39] report that CNTs the formed defects such as edges, 5,7-membered ring defects, vacancies, dislocation dangling bonds, Y-junctions and kinks. These are inherently present in as-grown and acid-purified CNTs and contribute to a decreased oxidative stability of CNTs.

Furthermore, the oxidative stability of CNTs in the air is dramatically decreased when catalysts are present. Zhou et al. [40] studied the oxidation of CNT during synthesis in which traces amounts of catalyst (Fe) were present. They found that the thermal stability of CNTs decreased dramatically at 350°C due to a catalytic effect. Amorphous carbon was removed during air oxidation of CNTs at 400°C without damaging the tube structure. Moreover, Fe-encapsulated carbon was destroyed followed by Fe oxidation to Fe₂O₃ at 400°C [41].

Electrical properties of CNTs [42]

Carbon nanotubes are well known as highly conductive materials at room temperature. The resistivity for SWNT and MWNT has been reported to be as low as 10–6 Ω cm⁻¹ and 5 × 10⁻⁶ Ω cm⁻¹, respectively[43]. MWNT resistivity is lower than for SWNTs, probably because MWNTs typically have larger diameters than SWNTs. These values were obtained from experiments that examined material densities from those of carbon nanotubes ~ 1.3 g cm⁻³ for SWNT and ~ 2.1 g cm⁻³ for MWNT. Copper and aluminum have densities of ~ 8.96 g cm⁻³ and 2.7 g cm⁻³, respectively. At room

temperature, the maximum current density measured experimentally in individual SWNTs at room temperature reached 10^9 – 10^{10} A cm⁻². The major performance-limiting factor in the conductivity of CNTs arises from disorders. These include structural defects formed during synthesis processes or physical distortions, such as those caused by strong mechanical forces.

Semiconducting SWNTs (S-SWNTs) are intrinsic semiconductors, but their behavior usually appears to a p-type semiconductor behavior under ambient conditions. It has been established that the hole-doping of S-SWNTs results from molecular oxygen adsorption onto the SWNT surfaces. The removal of oxygen molecules in a vacuum returns the material to the intrinsic semiconductor behavior of S-SWNTs [44].

Adsorption mechanism of CNTs

A schematic of the adsorption of gas molecules on isolated carbon nanotubes and carbon nanotube bundles is depicted in Figure 2.6. Figure 2.6 (a) shows that the most favorable locations for adsorption of gas molecules on CNTs are the top surface, hollow sites, zigzag, and the axial locations. Figure 2.6 (b) shows four surface sites that physically adsorb various gas molecule [45, 46]. These are (1) the external surface of the bundle, (2) the groove formed at the contact between adjacent tubes on the outside of the bundle, (3) interior pores of individual tubes and (4) interstitial channels formed between adjacent tubes within a bundle. Adsorption of a gas analyte on these sites leads to local modifications of the work function. Some of these sites will not be available for certain gases due to unfavorable gas molecule dimensions relative to the site diameters.

Moreover, chemical adsorption on carbon nanotube surfaces occurs due to CNT defectives, including topological defects, vacancies, and impurities. These defects strongly affect the electronic and transport properties of CNTs [47]. Furthermore, numerous studies reported that CNTs-based gas sensors with defects achieved higher sensitivity those having no imperfections. This is due greater interaction of the adsorbing species at defect sites.

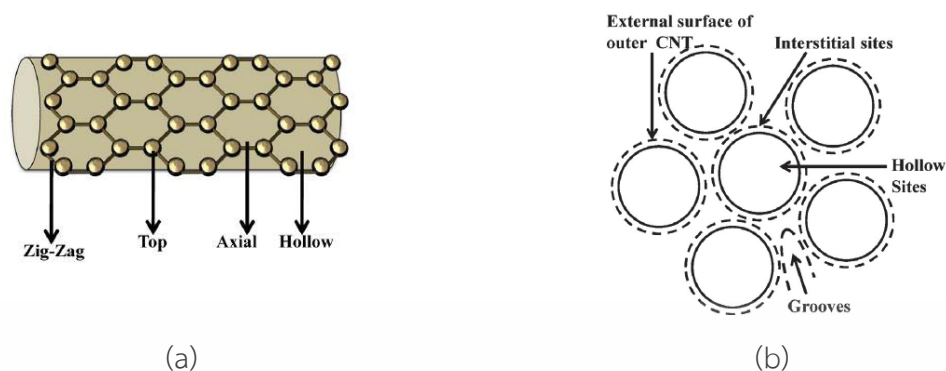


Figure 2.6 Schematic representation of adsorption sites on (a) single carbon nanotubes and (b) carbon nanotube bundles [48].

2.3.2 CNT synthesis

CNTs have been synthesized through various methods [49]. These include arc discharge [50], laser ablation [51], chemical vapor deposition (CVD) [52], high pressure carbon monoxide (HiPco), electrolytic [53], hydrothermal [54], and template method [55]. Among these, arc discharge, laser ablation, and CVD methods are the most favored and used to synthesis of CNTs. As-grown CNTs obtained from both arc discharge and laser ablation, CNTs are high-quality nanotubes such as high purity, long tube, and perfectly straight. However, neither the arc discharge nor laser ablation methods are suitable for commercial production because its difficulty to scale-up nanotube production and expensive [56].

Chemical vapor deposition

Chemical vapor deposition (CVD) method is used to synthesis CNT since its large-scale production, including, various substrates, ease of control over the chemical impurities, and low-cost. In the CVD process, hydrocarbon gas volatiles (carbon source) carried into a high temperature reactor (approximately 700- 900 °C) [56]. Ethylene, methane, or acetylene is widely used as sources of hydrocarbon. At high temperatures in the reactor, the decomposition of hydrocarbon gas has occurred, and then, carbon atom deposit on the metal catalyst to formed-CNTs. The catalysts particle such as Ni, Fe, or Co, is widely used to fabricate CNTs. The CVD method can synthesize both MWNTs and SWNTs depending on the temperature employed. SWNTs are synthesized at higher temperatures than MWNTs [57].

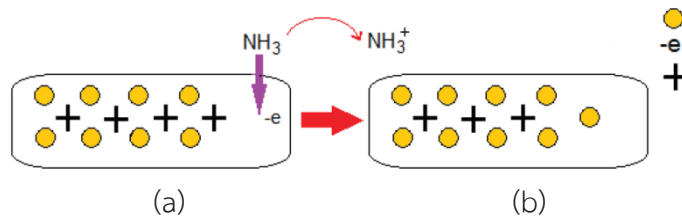


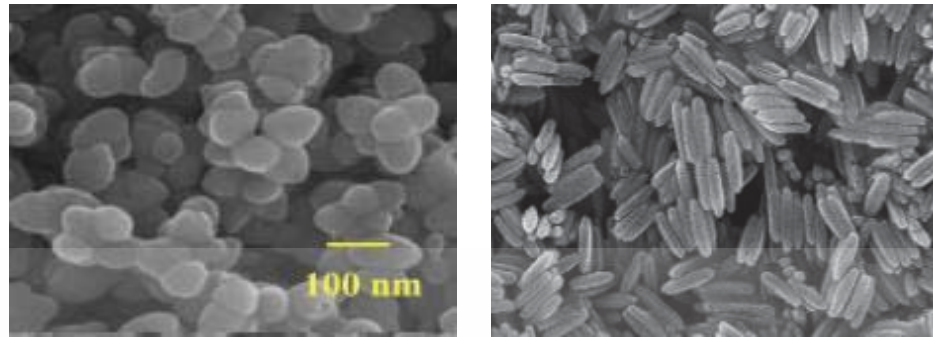
Figure 2.7 NH₃ sensing-mechanism of CNT sensors [58, 59].

2.3.3 Sensing mechanism

The sensing mechanism of CNT is based on the changes in electrical conductivity. This is due to the physical adsorption of gas molecules on the pristine CNT surface is depicted in Figure 2.6. The sensing behavior of CNTs presents both p and n behaviors, depending on analyte gas. CNTs present an n-type behavior when exposed with NH₃ while p-type behavior for CO₂, CO, NO, NO₂, and O₂. Figure 2.7 depicts the adsorption of NH₃ (reducing gas) on CNTs surface. NH₃ donates electrons to CNTs, leading to an increased hole carrier and decreased resistance in CNTs.

2.4 Iron Oxide

Iron oxide is a metal oxide semiconductor and is utilized in several applications such as magnetic devices, pigments, photo catalysis, gas sensors, and biomedicine [55] due to its high chemical, good thermal stability, easy synthesis, and low-cost [60]. Iron oxides are chemical compounds, which consisting of iron(Fe) and oxygen(O) [7]. Additionally, iron oxides have many phases, such as hematite (α -Fe₂O₃), maghemite (γ -Fe₂O₃), magnetite (Fe₃O₄), and wüstite (FeO) with different chemical and physical properties. Among these, α -Fe₂O₃ is the most favored and used to detect combustible and toxic gases (e.g., LPG, propane, butane, and methane) due to their high sensitivity and selectivity [60]. In the current research, the nanostructure of Fe₂O₃ materials (i.e., nanoparticles, nanopores, and nanorod) has attracted much attention for gas sensing applications with low concentrations, as shown in Figure 2.8. This due to their high surface activities, high surface-to-volume ratios, and high carrier mobility [61]. Moreover, the increase in gas sensing-performance of Fe₂O₃ nanostructures is successfully improved by the mixing of Fe₂O₃ in other materials. Various metal oxides (e.g., Pt, Au, Zn, Pd, or RuO₂) have been mixed into Fe₂O₃ to make it selective for particular gases [62] [63]. For example, ZnO mixed Fe₂O₃ works as a selective NH₃ sensor that can operate at room temperatures [64]. When mixed with Pt, Pd, or RuO₂, the Fe₂O₃ sensors can detect acetone, which finds utility in medical diagnostic applications [62].

(a) α -Fe₂O₃ nanoparticles [65](b) α -Fe₂O₃ nanorods [66]**Figure 2.8** Typical FE-SEM images of various α -Fe₂O₃ nanostructures.

However, most Fe₂O₃ nanostructure-based sensors require an operating temperature of ~200°C to 500°C [67, 68]. The nanoparticles' growth and aggregations at these temperatures often hinder the sensing ability of the template free MOx nanoparticles [69].

Sensing mechanism

Figure 2.9 shows a schematic represent of the sensing mechanism of n-type semiconducting metal oxide-based resistive sensors. For air ambient, absorbed-oxygen molecules extract electrons from the conduction band (E_c) at the surface layer. This results in formation of chemisorbed-oxygen ions, such as O_2^- , O^- , and O^{2-} . This result is band bending and an electron depleted region with generated-potential barriers. Thus, the conductivity of n-type MOx decreases, resulting in increased resistance.

It is notable that various types of chemisorbed oxygen ions function at different operating temperatures. At operating temperatures below 100 °C, chemisorbed-oxygen ions are mainly O_2^- . At the temperature of around 100°C to 300°C, O_2^- ions will capture electrons and then be transforming into O^- ions. The O^- can be converted into O^{2-} ions at working temperature higher than 300°C. The formation process of oxygen ions can be summarized as follows [70]:

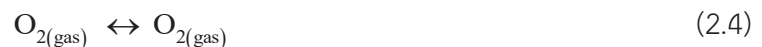




Figure 2.9 depicts a schematic diagram for a reducing gas sensing mechanism using n-type MOx materials at room temperature. In the air, O₂ molecules are adsorbed onto the surfaces of MOx. Then, they extract electrons from the conduction band E_c and trap them at the surface in the form of O₂⁻ ions. This leads to band bending and generation of an electron depleted layer. When the MOx sensor is exposed to the target gas molecules, the gas molecules are absorbed onto the MOx's surface with O₂⁻ ions. For reducing gases, such as H₂S, H₂, NH₃, HCHO, or C₂H₅OH, the chemical reaction between reducing gases and O₂ ions, releases electrons to the electron depleted layer. This reverses the band bending (i.e., it reduces the potential barrier energy: ΔΦ) and, thus, increases electrical conductivity. In contrast, when gas sensors are exposure to oxidizing gas with NO, NO₂, Cl₂ and O₃, reactions with chemisorbed oxygen ions will capture electrons. This will widen the electron depleted layer, resulting in increased potential barrier energy (ΔΦ). Accordingly, the surface resistance of the MOx sensor is increased.

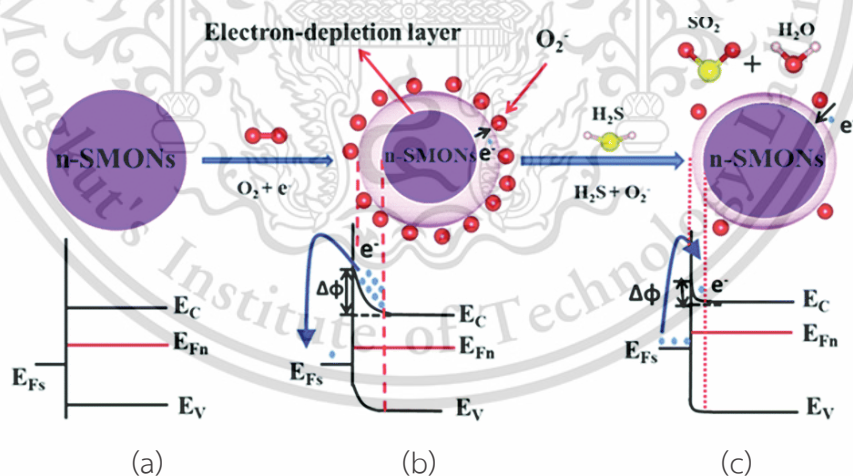


Figure 2.9 Schematic representation of the sensing mechanism of n-type MOx nanostructures under reducing gases [71].

2.5 MOx-CNT Films

MOx-CNT films are the combinations of MOx and CNT composite [49]. Their combined properties can improve the efficiency, enhance sensitivity to target gases, and effectively operate at lowered temperatures, even room temperature. Furthermore, hybrid materials consisting of CNTs and MOx provide higher gas-sensing performance than their single component.

2.5.1 Synthesis of MOx-CNT films

MOx nanoparticles could adhere at sidewalls of CNTs via bonded interactions. For example, carboxyl or hydroxyl groups were formed on a sidewall of CNTs using strong acids such as hydrochloric acid (HCL). Such functional groups can directly interact with the oxygen of MOx nanoparticles via hydrogen bonding. Bonded interactions between such functional groups with metal atoms through the electron pairs on oxygen molecules are also possible.

2.5.2 Typical Coating methods.

After the synthesis of MOx-NT films, a mixed solution of the nanocomposite is coated onto a substrate. Usually, a spinning and screen-printing method is employed [10, 72].

Spin-coating

Spin-coating is the simplest method for fabricating a hybrid thin-film on a substrate. These procedures are convenient, fast, and reproducible and use low-cost equipment. Figure 2.10 shows the spin coating process's schematic diagram [73-75]. These are i) the deposition, ii) spin up, iii) spin-off stages, and iv) evaporation. In the first stage, a coating liquid material is deposited onto the top of a wafer or flat substrate, using typically a pipette. The amount of applied liquid depends on the liquid viscosity and the size of the substrate to be coated. In the second stage, spin up, the liquid is spread across the wafer substrate using centrifugal force. The substrate is spun at a specific rate depending on the desired film thickness. At this stage, most of the solution is forced from the substrate surface. In the third stage, the substrate is spun at a constant rate. Viscous fluid forces control the fluid thinning characteristics. In the final stage, solvent evaporation controls the thinning characteristics of the coating. After completing evaporation of the solvent, a solid film results.

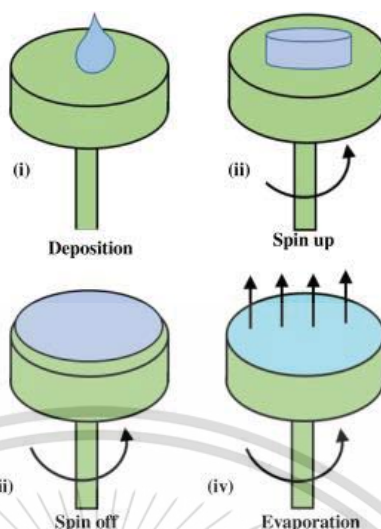


Figure 2.10 Schematic diagram of the spin coating process [73].

Screen printing

The screen printing method is widely used for coating films on the substrate due to its inexpensive in the production of sensing elements for gas sensors. The screen-printing process is 'capable of printing any ink onto any substrate.' The process of screen printing method [76] is depicted in Figure 2.11. The MOx-CNTs inks (paste) are deposited onto a mesh mask, and then are pressed through the screen using a squeegee. After leveling, the printed wet film is dried at a specific temperature. The thickness of the screen-printed film depends on the viscosity of the paste, the applied pressure, the speed of the squeegee, the snap-off distance between the screen and the substrate, and the mesh size of the screen.

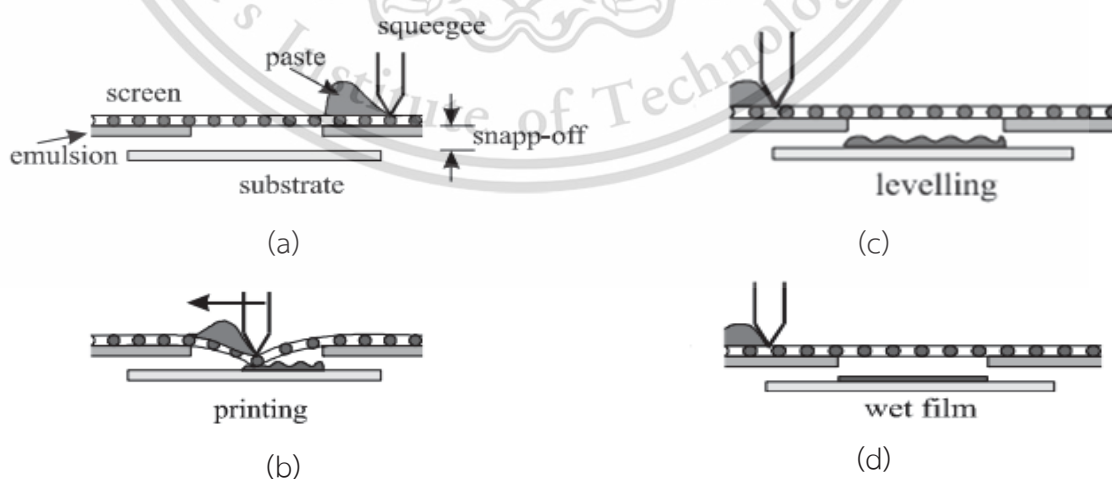


Figure 2.11 The screen-printing process.

2.5.3 Sensing mechanism

Generally, the sensing behavior of many MOx is n-type, while CNTs are p-type semiconductor [29]. When the CNTs and MOx are combined, MOx-CNT nanocomposites' sensing behaviors can be either p-type or n-type semiconductors, depending on the amount of MOx and CNT in composite materials. Figure 2.12 shows the case with a small amount of MOx nanoparticles trapped on a CNT wall. The decoration of MOx is the discrete structures on CNTs. The sensing behavior of this structure is p-type. Figure 2.13, shows the case of a large amount of MOx nanoparticles trapped on CNTs. The MOx decorations are indiscrete structures on CNTs. The sensing behavior of this structure is n-type. Electrical conductivity of such MOx-CNT sensors increases reducing gases are adsorbed (H_2 , CO, or NH_3) [69] [8, 77].

CNTs decorated with discrete SnO_2 nanoparticles[69] depicted in Figure 2.12 (a) and (b). In a network, CNTs act as conducting channels for the gases. For example, a gas sensor shows a sensing behavior at room temperature as a p-type semiconductor when its surface absorbs ammonia or ethanol. Since ethanol is an electron donor, exposure of CNTs- SnO_2 to this analyte gas increases the resistance of the p-type sensing material. In the present case, both CNTs and SnO_2 have nearly similar work functions, and the Schottky barrier between them is very small [78]. This enables easy electron transfer between the CNT and the SnO_2 .

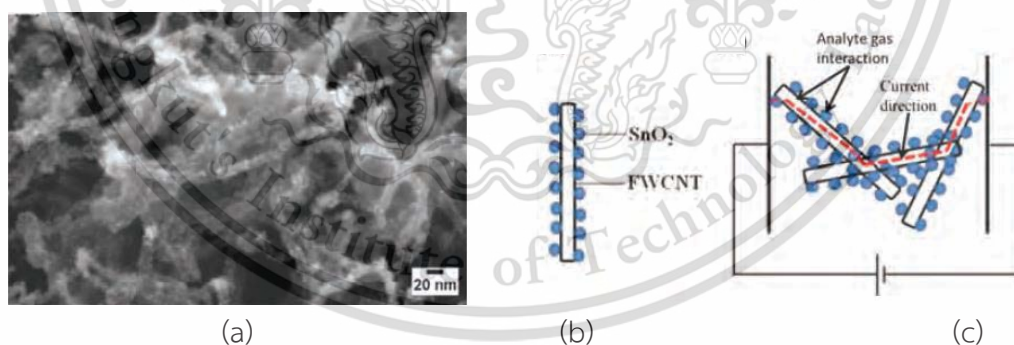


Figure 2.12 (a) SEM image of CNTs decorated with discrete SnO_2 nanoparticles and (b) analyte gas interaction and charge transport in a CNT- SnO_2 network. The red dotted line represents the direction of current between electrodes [69].

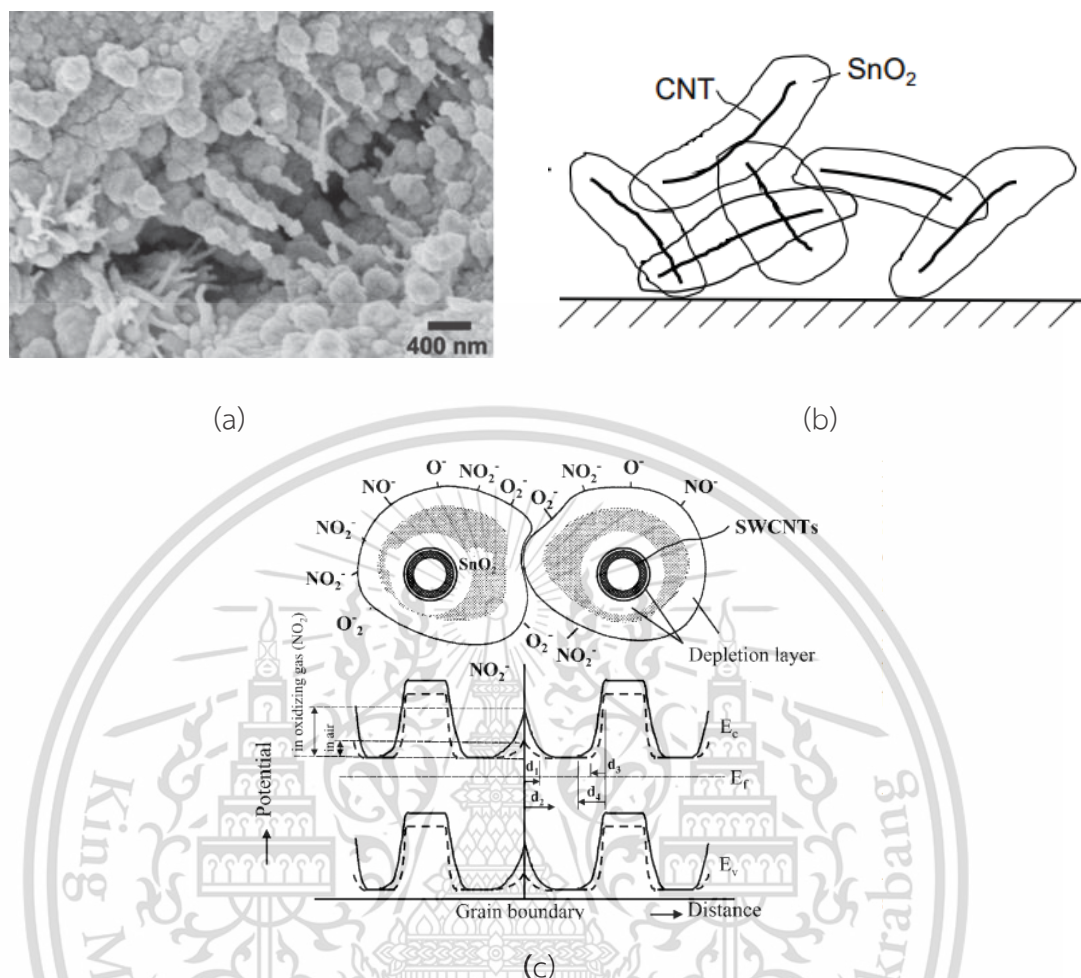


Figure 2.13 (a) FE-SEM image of a high-concentration hybrid SWNTs/SnO₂ sensor and (b) a schematic diagram of a hybrid SWNTs/SnO₂ gas sensor, SWNT bundles are embedded in SnO₂-based materials [77].

The direction of transfer is determined by the prevailing analyte atmosphere. However, the sensing behavior is changed to n-type when the operating temperature is increased to 200 °C and 400 °C. Such switching from p-type to n-type behavior at elevated temperatures reveals the dominance of SnO₂ in the process [79, 80]. An oxygen species chemisorbed (\bar{O}) on a MO_x surface is activated in the operating temperature range of 200°C to 400°C. When SnO₂ is exposed to an analyte, it adsorbs gas molecules, catalytically decomposes them, and releases electrons in the network, enhancing conductivity.

CNTs embedded in MO_x or CNTs-coated with MO_x lead to a buildup p/n heterojunctions [81], which are formed by (n-oxide)/(p-CNT)/(n-oxide). The exact mechanism of the high response of the MO_x-CNTs composites as a sensing material is still not clear.

However, there are many reports [81, 82] that describe its using the model of a potential barrier to electronic conduction at the grain boundary. This was proposed by B.-Y. Wei and et al [77], and is depicted in Figure 2.13 (c). This model presents the changes of the electronic energy bands for two depletion layers, one on the surface of the MO_x, and the other is in the interface between the CNT and mixed oxide. When the mixed oxide is exposed to ethanol gas, ethanol molecules react with oxygen ions on the surface of the mixed oxide. Additionally, the nanotubes embedded in MO_x film will provide for easy diffusion of chemical gas through the bulk material. This change of the depletion layer in the p–n heterojunctions of CNT/MO_x has been used to explain the enhanced response of the film at low operating temperatures. It is due to amplification effects of the junction structure combined with a gas reaction. Moreover, the formation of CNTs in the MO_x matrix can also introduce nano-channels through bulk material. This achieves a greater surface area to volume ratio, providing good gas-adsorption sites inside and outside of the CNTs. The gas molecules can easily be transported into the gas-sensing layers, leading to increasing sensitivity.

2. 6 Characterization

2.6.1 Atomic Force Microscopy

Atomic force microscopy or AFM is widely used for the study of morphological and topographical, which provides quantitative information on sample height or thickness [83]. Atomic force microscopy works by moving the sample in an x-y grid beneath a sharp tip attached to the free end of a cantilever passed over the surface of a material under examination. This process is demonstrated in Figure 2.14 (a). The probe approaches the sample surface, a small interaction force forms between the probe and sample. The cantilever position is usually measured using an optical lever method. Using an appropriate feedback system in the control unit, the distance between the probe and sample is accurately regulated by the sample height variation. A piezoelectric xyz-scanner is usually used both to control the vertical position of the sample (z) and to raster-scan the sample in the x-y-plane. Images produced by the feedback voltage are called constant force images (or height images). Atomic force microscopy is utilized in this dissertation as shown in Figure 2.14 (b).

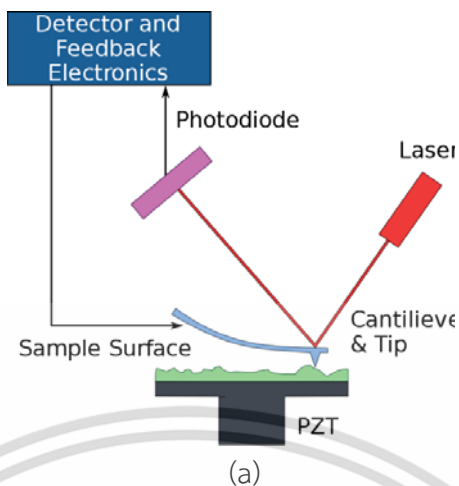


Figure 2.14 (a) Schematic illustration of an atomic force microscope [83] and (b) Photograph of atomic force microscope AFM XE-100 [123].

2.6.2 Raman Spectroscopy

Raman spectroscopy is widely used to investigate the structure, purity, and quality of CNTs. Raman spectroscopy is based on inelastic scattering of a monochromatic light source (laser). In Raman spectroscopy, photons of electromagnetic radiation interact with a sample and are absorbed by the molecules of the sample and re-emitted. The frequency of re-emitted photons is shifted up or down compared to the photons of incident light depending on the quantized vibrational or rotational energy levels (phonons) in the molecules.

Typically, the Raman spectra of a CNT consist of several characteristic peaks, as shown in Figure 2.15. The dominant peak is at around 1582 cm^{-1} , is defined as the G band [84]. It originates from the in-plane vibrations in a graphene lattice, reflecting the graphitic nature of CNTs. However, due to curvature of SWNTs, G mode is divided into G^+ and G^- sub-bands representing vibrations along the nanotube axis and its circumferential direction respectively. The peak at around 1350 cm^{-1} is known as D mode. It is defined as defects or disorder structures in the crystal lattice.

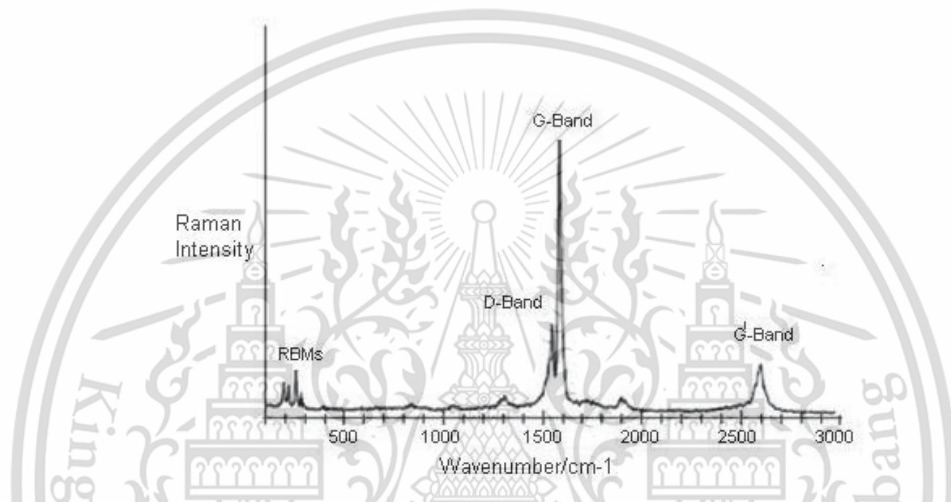


Figure 2.15 Raman characterization of SWNT; radial breathing mode (RBM) peak at $\sim 100\text{--}350\text{ cm}^{-1}$, G mode at $\sim 1582\text{ cm}^{-1}$, and D mode at $\sim 1350\text{ cm}^{-1}$ [85].

At Raman spectra peak of around $100\text{--}350\text{ cm}^{-1}$ is known as a radial breathing mode (RBM). It is only observed in single-walled carbon nanotubes. The RBM corresponds to the vibration of the C atoms in the radial direction. It arises from the out-of-plane vibrational modes in the crystal lattice and is attributed to radial expansions and contractions in the SWNTs. It has been found that the RBM frequency (ω_{RBM}) is inversely proportional to the diameter (d_t) of SWNTs [86]. The wavenumber ω_{RBM} of the RBMs inversely dependent on the tube diameter, which can be calculated as follows:

$$d_t = \frac{248}{\omega_{RBM}} \quad (2.8)$$

In this experiment, the characteristics of $\text{Fe}_2\text{O}_3\text{-CNT}$ films were analyzed by Raman spectroscopy (Renishaw inVia Reflex) with an Ar laser (514.5 nm) as the excitation source, as depicted in Figure 2.16.



Figure 2.16 Photograph of the Raman spectroscopy (Renishaw inVia Reflex) at Western Digital Thailand [124].

2.6.3 X-Ray Photoelectron Spectroscopy

X-Ray Photoelectron Spectroscopy (XPS) [87, 88] is used to analyze chemical composition on the top surface of the materials with a depth of less than 10 nm. Elements present on the material's surface are identified using binding energy, are examined from survey scan results. Subsequently, high-resolution scans (XPS deconvolution) of the peaks can be obtained to give more information, such as the chemical bonding of elements. Moreover, comparing the areas under the peaks gives the relative percentages of elements detected in the sample. The principle of XPS is based on the photoelectric effect, as depicted in Figure 2.17. The material is exposed to radiation (light rays), resulting in electron emission. This electron is known as a photoelectron and has characteristic kinetic energies proportional to the energy of the radiation, according to Equation (2.12), where ϕ is the work function.

$$E_{\text{binding}} \approx E_{\text{photon}} - (E_{\text{kinetic}} + \phi) \quad (2.9)$$

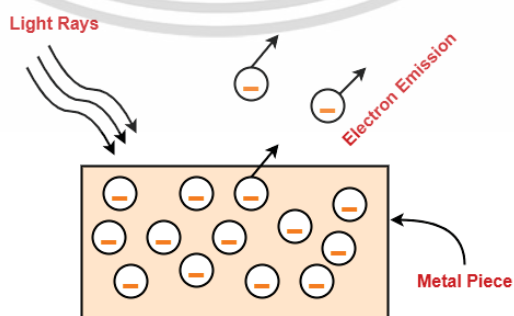


Figure 2.17 Photoelectric effects [126].



Figure 2.18 Photograph of XPS machine [127].

In this experiment, the surface composition changes of as grown Fe-CNT and Fe₂O₃-CNT films were measured by X-ray photoelectron spectroscopy (XPS; PHI 5700), which were carried out on an AXIS Ultra DLD-X-ray photoelectron spectrometer using a monochromatic Al K α source (1486.6 eV), and are shown in Figure 2.18

2.6.4 Field Emission Scanning Electron Microscopy

Field emission scanning electron microscopy (FE-SEM) is a widely used technique for considering thin films' morphology due to it provided high-resolution imaging of thin films. The sample is examined using FE-SEM. They must be conductive (if not, they need to be coated with conductive material such as C, Cr, Au, Pt) to avoid charging (local accumulation of electrons) from the electron beam. In this experiment, carbon nanotube films are usually ready for imaging directly, with no special sample preparation. In the case of Fe₂O₃-CNT films with many Fe₂O₃ in CNTs, films were Pt-coated to examine using FE-SEM. In this experiment, the morphology of Fe₂O₃-CNT was investigated via the field emission scanning electron microscopy with Hitachi model S-4700, as shown in Figure 2.19.



Figure 2.19 Photograph of a scanning electron microscope [128].

2.6.5 Thermogravimetric Analysis

Thermogravimetric analysis (thermal gravimetric analysis, TGA) is used to investigate the composition and thermal stability of CNTs [89]. In the process, the changes in the weight of CNTs at various temperatures can be caused by various factors such as decomposition, degradation, sublimation, vaporization, adsorption, desorption, oxidation, and reduction [89]. A derivative weight loss (DTG) curve can identify the point where weight loss is most apparent. Thermogravimetric and derivative thermogravimetric analyses are frequently used to examine the purity and thermal stability of CNTs. In this experiment, the thermal analysis of films was examined using thermogravimetric analyzer (Perkin Elmer; Pyris 1), as depicted in Figure 2.20.



Figure 2.20 Photograph of thermogravimetric analyzer (Perkin Elmer; Pyris 1) [125].

CHAPTER 3

RESEARCH METHODOLOGY

There are four parts in this chapter consisting of the synthesis of the Fe-CNT films, the preparation of Fe-CNT films on a substrate, synthesis of the Fe₂O₃-CNT films, and the sensing test. In the first part, the Fe-CNT films were produced by the mist-CVD method, including the preparation of Fe-CNT films with the various deposition times. In the second part, the wet and dry processes were employed to prepare the Fe-CNT films on the substrate. In the three parts, the Fe₂O₃-CNT films were synthesized by air annealing, including the synthesis of Fe₂O₃-CNT with the various deposition times. In the last part, the measurement of sensors to detect an LPG gas operating at room temperature.

3.1 Synthesis of Fe/CNT Films

In this part, the Fe-CNT films were produced by the mist-CVD method, including the precursor preparation, and procedure of the mist-CVD method with the various deposition times.

3.1.1 Precursor preparation

Ethanol solution (C₂H₅OH, purity 99.8%, Sigma-Aldrich, Figure 3.1 (a)) and ferrocene powder (Fe(C₅H₅)₂, purity 98%, Sigma-Aldrich, Figure 3.1 (b)) were used as a carbon source and a catalytic source, respectively [14]. The precursor solutions were prepared by dissolving ferrocene powder in ethanol solution; the solution was ultrasonically stirred for 30 minutes (Figure 3.1 (c)), and then transferred into a container attached to the atomizer. The ratio of ferrocene to ethanol solution was fixed at 0.25 wt.%.

3.1.2 Mist-CVD procedures

The mist-CVD apparatus consisted of a furnace (500 mm in length), a quartz tube (55 mm outer diameter and 1200 mm in length), a mass-flow controller (MFC), an atomizer (~1.7 MHz, 20–30 W), Ar carrier gas (purity 99.99%) and a precursor solution, as shown in Figure 3.2. When the system was heated to 960°C under atmospheric pressure, the precursor solution was injected into the tube furnace at a rate of 1000 SCCM using argon gas as the carrier gas. The change in temperature furnace of the mist-CVD process for the synthesis of Fe-CNT films at 950°C, as shown in Figure 3.3. As-grown Fe-CNTs in

the high-temperature zone moved downstream and were collected onto a mixed cellulose ester (MCE) membrane filter at the bottom of the reactor under room temperature (from now on called “ as-grown films”). The diameter of MCE is 4.7 cm with 0.45 μm pore size. Moreover, the density of as-grown films was controlled by adjusting deposition time (for the current study; 15, 30, 45, 60, 90, and 120 min), as presented in Figure 3.5. After the completion of deposition, the atomizer was turned off and the reactor cooled to room temperature under an argon gas atmosphere.



Figure 3.1 Schematic diagram of ethanol-ferrocene precursor solutions preparation process of (a) ethanol solution, (b) ferrocene powder, and (c) ferrocene powder was dissolved in the ethanol solution. For mixing the solution, the solution was ultrasonically stirred for 30 minutes.

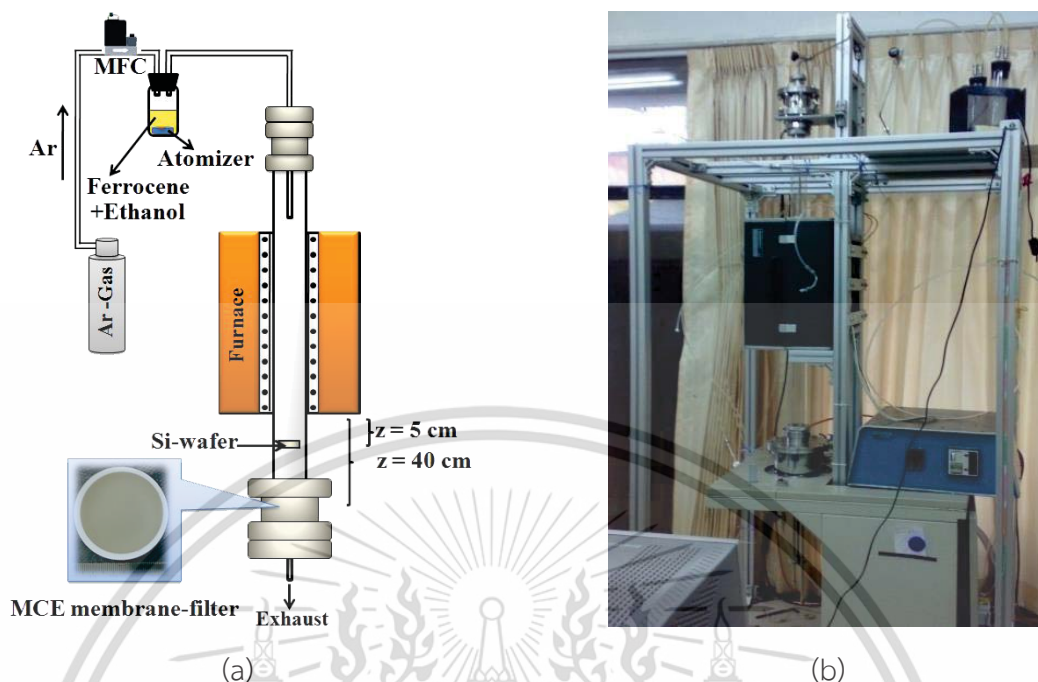


Figure 3.2 (a) Schematic diagram and (b) photographic images of the mist-CVD system used for the synthesis of Fe-CNT films.

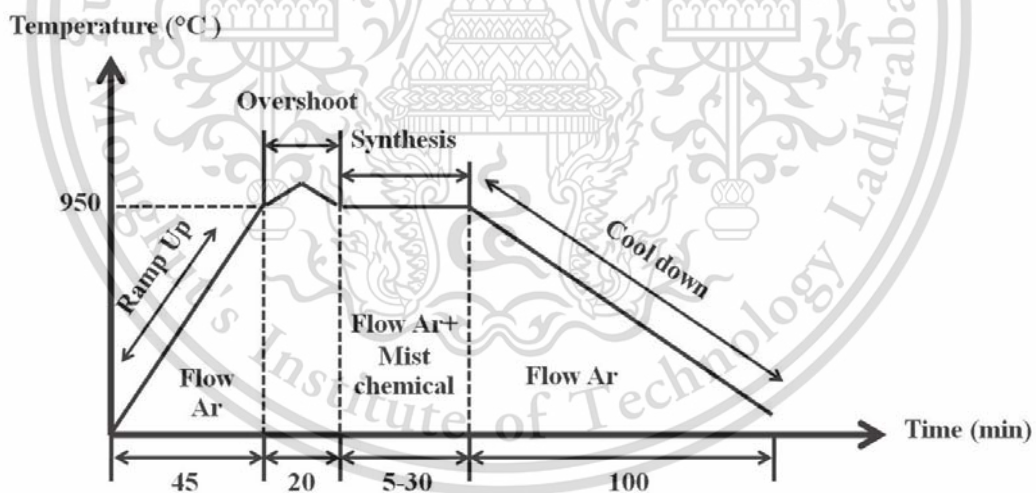


Figure 3.3 Temperature profile in the furnace of the mist-CVD process for the synthesis of Fe-CNT films at 950°C.

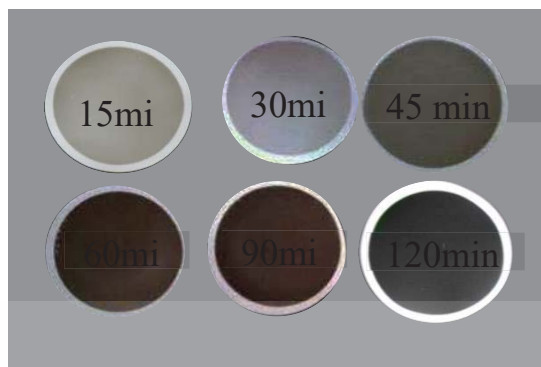


Figure 3.4 As-grown films (Fe-CNT films) on filter membranes after synthesized by mist-CVD method (Deposition time; 15, 30, 45, 60, 90, and 120 min).

3.2 Transfer method

In the above part, the Fe-CNT films were produced by mist-CVD method. These films coated on the membrane filter (from now on called “as-grown films”). In this part, the as-grown films were transferred on the substrate by using the dry and wet transfer methods, as presented in Figure 3.5. The dry transfer method consists of the pressing of films onto glass substrate without the use of any solvent (deionized water, acetone, or ethanol) (from now on called “dry-transfer films”), as shown in Figure 3.5 (a). Compared with the dry transfer method, the wet transfer method is the transferring of as-grown films with deionized water, acetone, and ethanol. As-grown films were transferred onto glass substrates by pressing onto substrate, and then, MCE were removed with dissolving in acetone solutions for 48 h. Subsequently, as-grown films were washed with ethanol and deionized water several times (from now on called “wet-transfer films”), as shown in Figure 3.5 (b).

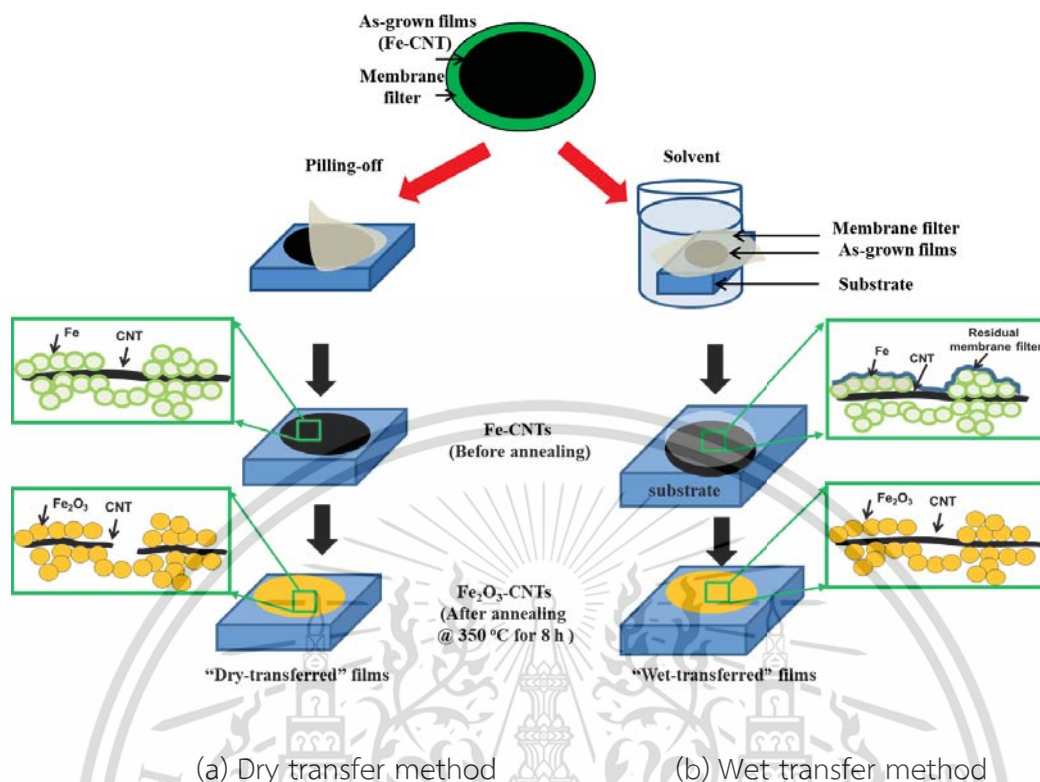


Figure 3.5 Schematic diagram of the dry transfer and wet transfer method. As-grown films (Fe-CNTs) on the membrane filter were transferred onto the substrate by (a) the dry transfer method (the pressing onto a substrate and pilling-off) and (b) the wet transfer method (pressing onto a substrate and removing the membrane filter with dissolving in acetone solutions for 48 h). Subsequently, both dry-transfer film and wet-transfer film were annealed in air at 350 °C to create Fe₂O₃.

3.3 Synthesis of Fe₂O₃-CNT films

After transferring on substrates, the as-grown films were annealed in air at the various annealing temperature for 8 h. with 47900 furnaces, as presented in Figure 3.6. After annealing at 150, 250, 350, 450, and 550 °C, the photograph of films was presented in Figure 3.7. Photographs of the Fe-CNT films (non-annealing) compared to the Fe₂O₃-CNTs with various annealing temperatures. It can be seen that Fe-CNT films are black in color. After annealing at temperatures up to 350 °C, the black color clearly changes to orange-red, which is indicative of α -Fe₂O₃ phase formation [90].

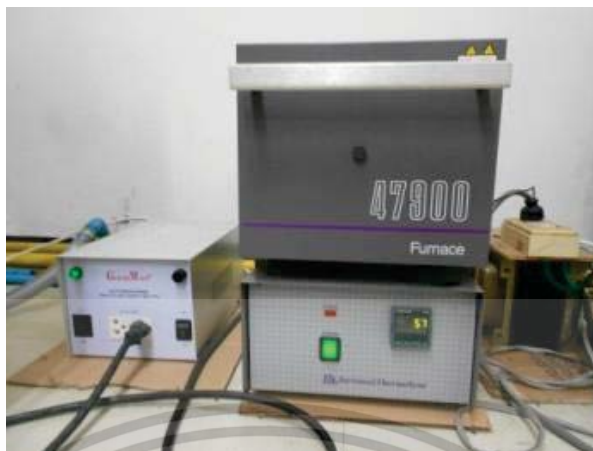


Figure 3.6 Photograph of 47900 furnaces 950°C was used for annealing of films.

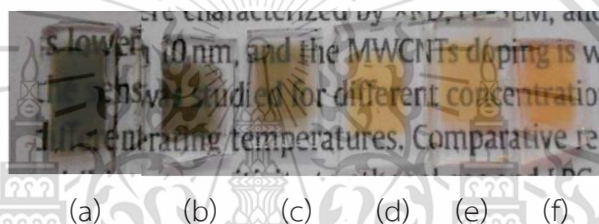


Figure 3.7 Photograph of films before and after annealing at various temperatures in air. (a) non-annealing, (b) 150°C, (c) 250°C, (d) 350°C, (e) 450°C, and (f) 550°C.

3.4 Comparison with purified CNT films

In experiment, Fe_2O_3 -CNTs was prepared using wet transferred and annealed in air at 350°C. Subsequently, Fe_2O_3 in Fe_2O_3 -CNTs was removed to fabricate pure CNTs via immersing in the HCL solution. Further, fabrication of pure Fe_2O_3 can be made via the removal of CNTs in Fe_2O_3 -CNTs, using annealing in air at 550°C. Characterizations of these films are examined via FE-SEM and Raman spectroscopy.

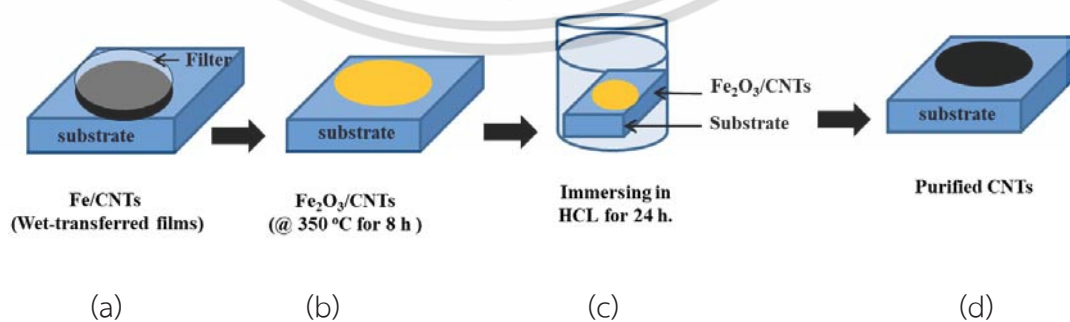


Figure 3.8 Schematic diagram of purification of purified CNTs.

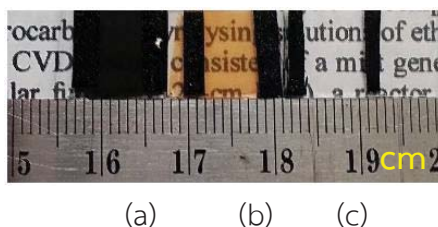


Figure 3.9 Comparison photograph of (a) Fe-CNTs, (b) Fe₂O₃-CNTs, and (c) purified CNTs.

3.5 Sensor testing system

Figure 3.10 presents the sensor structure (1.0 cm x 1 cm). These simple electrodes were made from two carbon taps (0.8 cm x 1 cm), which were placed on the surface of sensing films. Then silver (Ag) layer was dropped on the top of carbon taps to make electrical measurements. Sensor performance was examined in a home-built apparatus at room temperature, as depicted in Figure 3.11. The sensor system consisted of a sensing test chamber, gas cylinders, a mass-flow controller (MFC), computer, data acquisition card (NI-DAQ 6008), Kelley 2004 source meter, and operating in a LabVIEW program.

The gas sensors were placed inside a stainless-steel test chamber (800 cm³ inner volume) to investigate LPG gas sensing properties. The sensors operated with at a constant voltage of 5 V. LPG concentrations (ranging from 500 ppm to 500,000 ppm) were controlled using a mass-flow controller. LPG gas was introduced into a gas flow meter, and it was diluted with N₂ (or zero air) inside a gas mixer and injected into the test chamber with the controlled flow meter. The total flow rate into the test chamber was set to 1000 ml/min and kept constant for the entire measurement process. The electrical current signal of the sensors was measured and recorded via Kelley 2004 source meter. Then the real-time data will be displayed directly on the computer via a General Purpose Interface Bus (GPIB). After each series of successive injections, the sensor chamber was flushed using pure dry air or nitrogen for 1 h. This ensured cleaning of both the chamber and sensor surfaces. Once the sensors had recovered their baseline resistance, a new set of measurements was made.

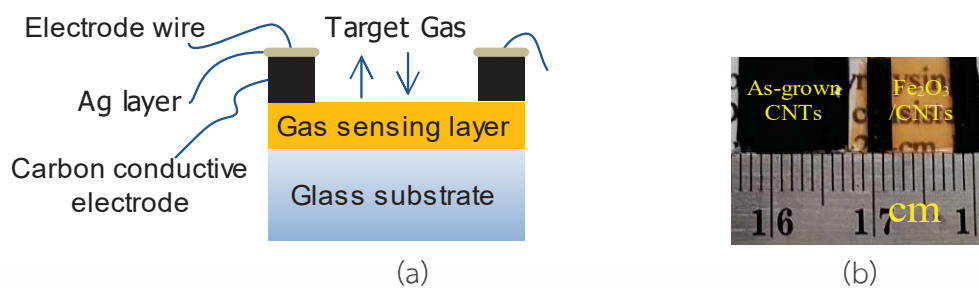


Figure 3.10 (a) Sensor structure and (b) photograph of Fe₂O₃-CNT films based on sensors.

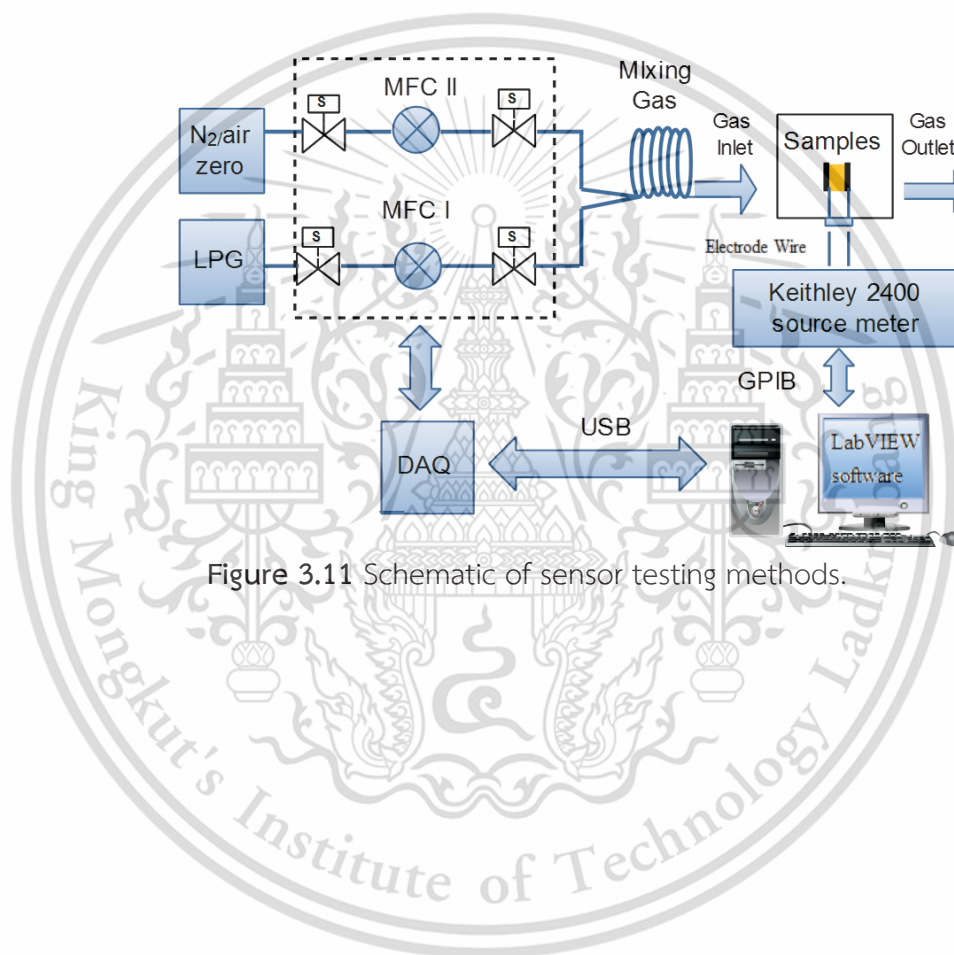


Figure 3.11 Schematic of sensor testing methods.

CHAPTER 4

RESULTS AND DISCUSSION

4.1 Materials

4.1.1 As grown Fe-CNT films

Figure 4.1 (a) illustrates the photograph of as-grown films (Fe-CNT films) on the membrane filter. The color of films is black, which refers to CNTs. FE-SEM image (Figure 4.1 (b)) presents the randomly oriented entangled CNT with adhering of nanoparticles onto CNTs. Raman results (Figure 4.10 (a)) indicate single-walled carbon nanotube (SWNTs) with diameters in the range of 0.9 to 1.9 nm. Those nanoparticles were covered with a graphitic shell or carbon cages with average diameter of 7.33 nm, estimated from TEM results (Figure 4.1 (c) and Appendix A). It is notable that determination of nanoparticles in as-grown films were examined using XPS. XPS results (Figure 4.5 (a)) indicate that the nanoparticles in as-grown films (before annealing) were mostly metallic Fe. From this morphology, the metal-Fe particles on the CNT walls were well separated and decorated in an isolated fashion.

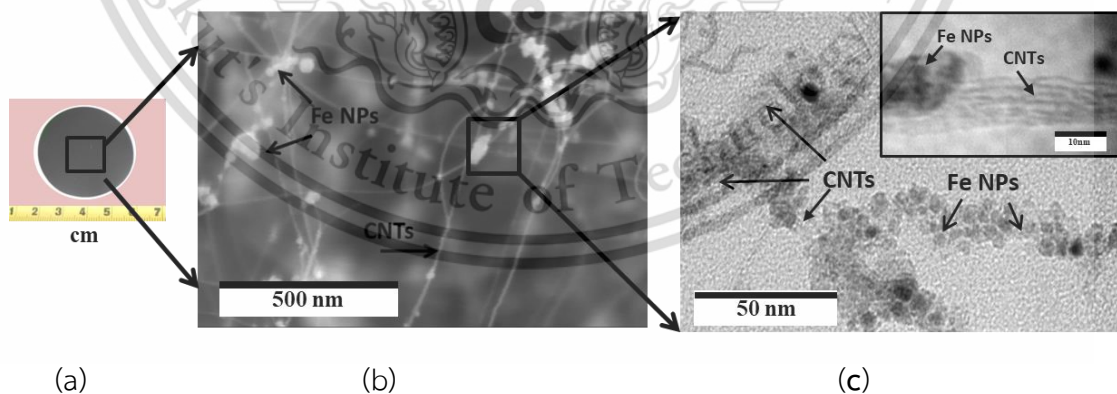


Figure 4.1 (a) Photograph, (b) FE-SEM image, and (c) TEM image of as-grown (or Fe-CNTs) films on the membrane filter.

4.1.2 Dry and wet methods

In this section, the effects of the dry and wet preparation on the morphological changes in Fe_2O_3 -CNTs and LPG sensing-performance were examined.

FE-SEM

Figure 4.2 presents that the typical surface morphologies of dry-transferred and wet-transferred films before annealing. Dry-transfer films before annealing (Figure 4.2 (b))) presents a highly porous morphology with large volume among the CNTs, which was similar to that obtained from as-grown films, as shown in Figure 4.1. CNTs were formed as web-like structures by accumulating individual CNTs, which were generally attached to small Fe nanoparticles on their surfaces. The obtained similar surface morphology is reasonable because dry-transfer films before annealing were from the bottom (near the surface of the MCE membrane filter) of as-grown films.

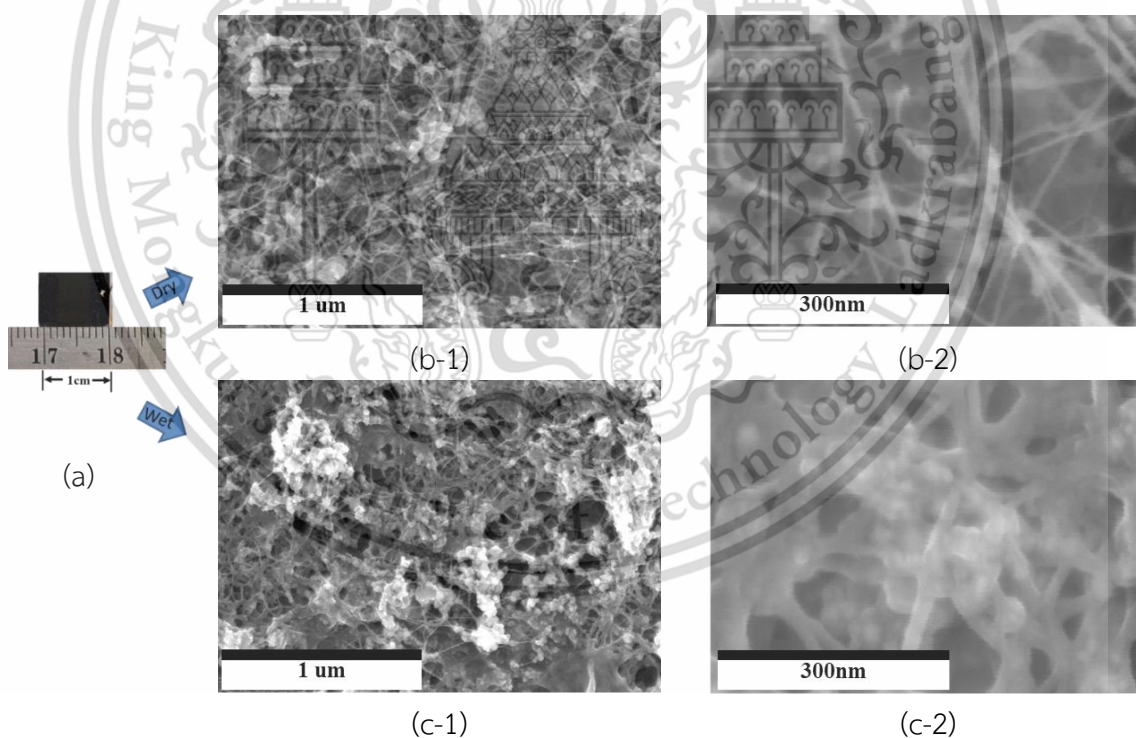


Figure 4.2 Before annealing, (a) typical photograph of as-grown films on glass substrate after transfer process. FE-SEM images of (b) the dry-transferred and (c) wet-transferred (Fe -CNT) films.

Typical surface morphologies of the wet-transferred film before annealing (Figure 4.2 (c)) is a compact mat-like structure after immersion in solutions (DI water, acetone, and ethanol) due to Van der Waals forces between individual tubes in the solution [91-93]. Moreover, the impurity (thin jelly-like materials) -covered on CNT films was also observed as the residual MCE membrane filter, which was detected C-O bond from the XPS spectra for C1s states (Figure 4.4 (a); upper) and C=O bond from O1s states (Figure 4.6 (a); upper). The residual MCE membrane filter was not completely removed during immersion in solutions due to the high porosity of CNTs; the MCE membrane filters diffused into the as-grown films and then were linked to Fe and CNTs during immersion in acetone solutions.

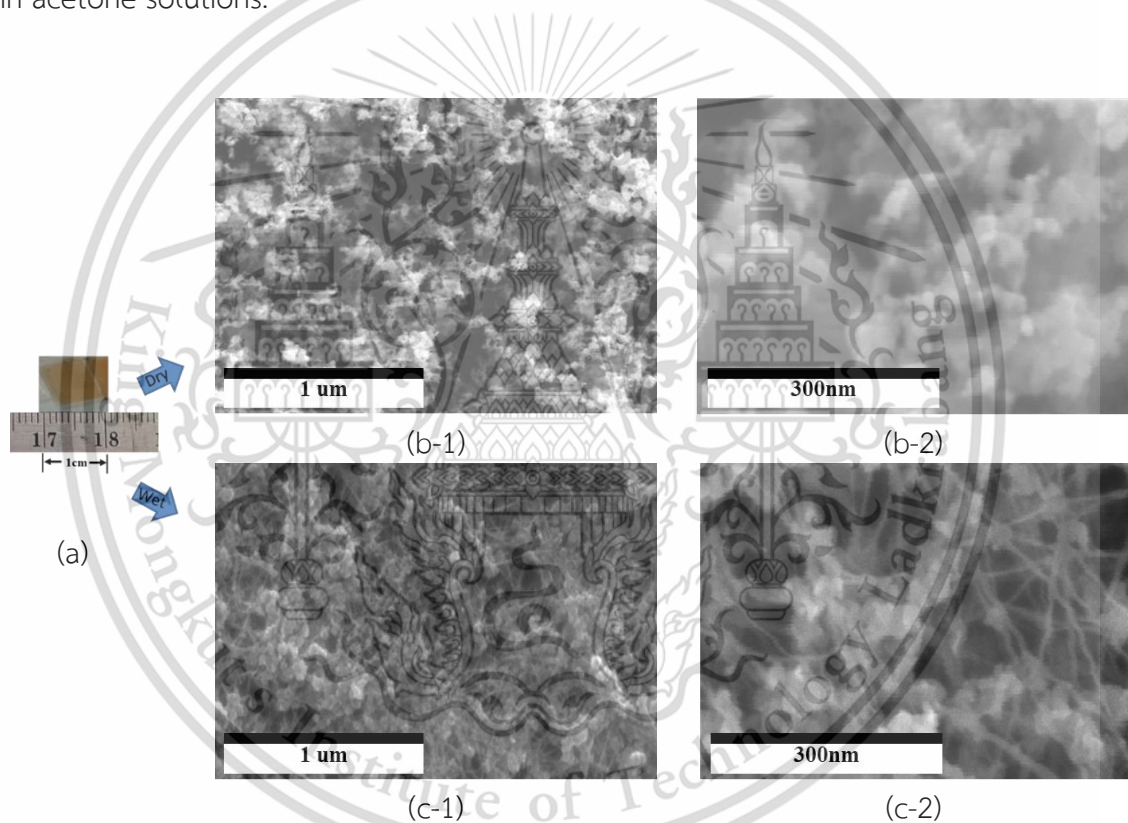


Figure 4.3 After annealing, (a) photograph of Fe_2O_3 -CNT films on substrate. FE-SEM images of (b) the dry-transferred and (c) wet-transferred (Fe_2O_3 -CNT) films.

However, the residual MCE membrane filter could be eliminated after annealing in air at 350°C (Figure 4.3 (c)), resulting in the morphology of the films becoming web-like structures. Moreover, Raman results (Figure 4.10 (b)) present that the I_G/I_D ratio of the wet-transfer films before annealing was approximately 4.2 before annealing; however, the wet-transferred film after annealing was 12.5, indicating the removal of the residual MCE membrane filter and carbon impurities from the Fe₂O₃-CNT thin films after annealing in air at 350°C. Furthermore, dry-transferred film (Figure 4.3 (b)) presented the discontinuity of CNTs due to the burn out of CNT during annealing at high temperature, resulting in the branch-like structure.

XPS analysis

The XPS technique was used to analyze the chemical composition on the top surfaces of the materials (depth < 10 nm). Elemental composition can be identified by the peak positions in terms of binding energy. XPS results of the dry and wet-transferred Fe-CNT films before and after annealing in air at 350°C are illustrated in Figure 4.4 and Figure 4.5.

Figure 4.4 (a) illustrates the carbon atom in the dry-transferred and wet-transferred (Fe-CNT) films. All films exhibited the main peak of 284.9 eV, which were ascribed to the sp² (C-C) bonds in CNTs. This indicates that the most carbon atom in all films was CNTs. Minor peak at 284.3, 285.4, 286.3, 288.5, and 291.2 eV, which were ascribed to the C-Fe*, sp³ C-C bonds, C-O-C, C-O or O-C=O, and the shake-up satellite peak of sp² carbon, respectively [94]. Compared to the wet-transferred films, XPS C1s spectra of wet-transferred films before annealing (Figure 4.4 (a): upper panel) occurred at a new peak of 287.2 eV (C=O), which were assigned to the compound of the membrane filter that remained in the sample after being dissolved in solution. However, this peak (287.2 eV) was easily eliminated after annealing at 350°C. After this, the wet and dry-transferred (Fe₂O₃-CNT) films had similar peaks upon annealing, as shown in Figure 4.4 (b).

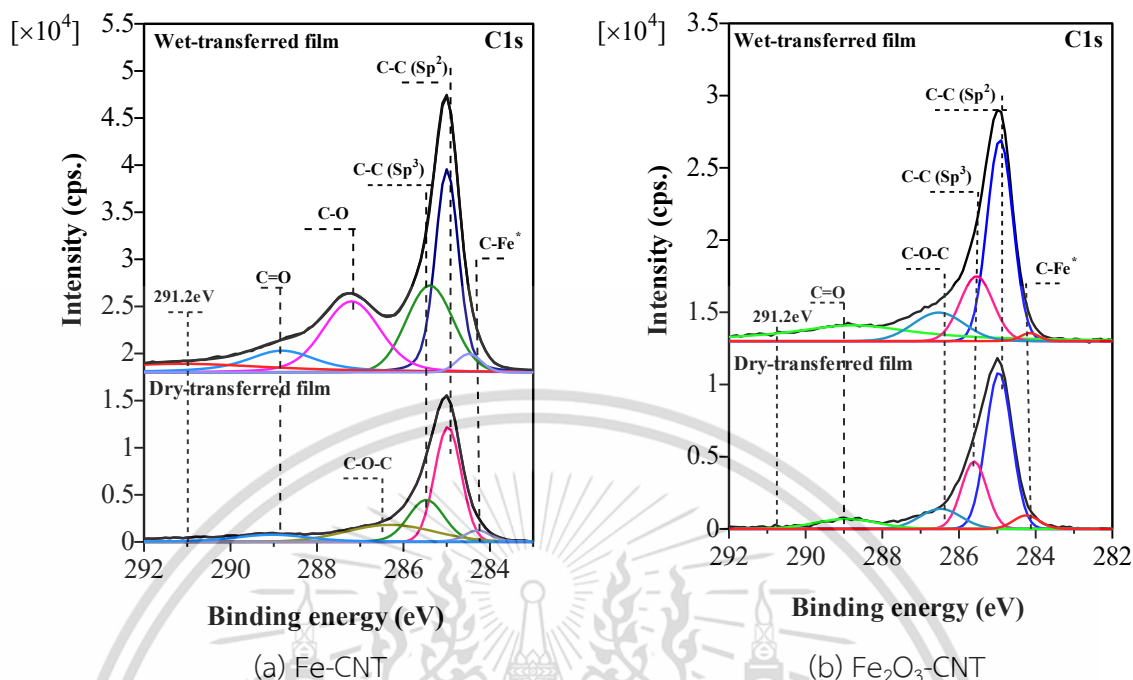


Figure 4.4 XPS spectra for C 1s states. Wet-transferred and dry-transferred films (a) before annealing (Fe-CNT) and (b) after annealing (Fe₂O₃-CNT).

Figure 4.5 (a) presented the Fe2p spectra of dry and wet-processed Fe-CNT films. They exhibit the same six peaks. The Fe⁰ peak at 707.4 eV is related to the presence of metallic iron on the Fe-CNTs [95]. The peak at 708.2 eV can be assigned to a carbide species [96]. A Fe²⁺ species is represented at binding energies (BE) of 709.4 eV, which is related to FeO [97]. A Fe³⁺ ion is represented by two peaks at BE of 711.4 eV and 713.0 eV, which is assigned to Fe₂O₃ and FeOOH, respectively. The binding energies of the shake-up satellites of Fe²⁺ (2p_{3/2}) and Fe³⁺ (2p_{3/2}) are 715.1 eV and 720.5 eV, respectively, which is consistent with experimental data reported by previous authors [98]. According to the phase content, Fe2p spectra, a main Fe2p_{3/2} peak is observed at 711.3 eV for all samples. This indicates that the surfaces of the NPs are predominantly Fe₂O₃, and included FeO and FeOOH. Moreover, the Fe₂O₃-CNTs prepared using both dry and wet processes, are similar in terms of their C and O spectral components after annealing (Figure 4.5(a) and (b)). The strongest O1s and C1s components at 530.4 eV and 284.9 eV correspond to the O-Fe of Fe₂O₃ and sp² of CNTs, respectively. Overall, these results demonstrate that Fe₂O₃-CNTs are formed from Fe-CNTs under an annealing at 350°C. Additionally, the atomic percent (At %) (see in Appendix C) demonstrates that the O:Fe atomic ratio on the Fe₂O₃-CNT films was close to 2:3, which is probably from Fe₂O₃ [10].

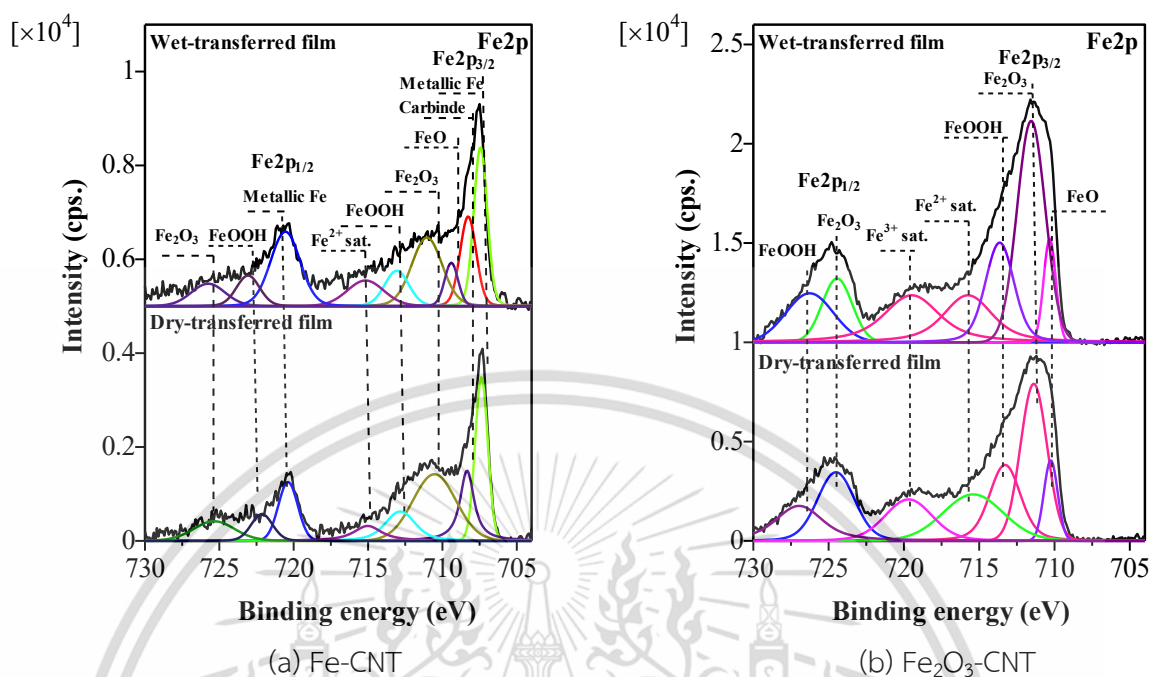


Figure 4.5 XPS spectra for Fe2p states. Wet-transferred and dry-transferred films (a) before annealing (Fe-CNT) and (b) after annealing (Fe₂O₃-CNT).

Before annealing, deconvoluted XPS O1s spectra of both in dry-transferred and wet-transferred (Fe-CNT) films were shown in Figure 4.6 (a). There are two similar peaks in both dry and wet films, 530.1 eV and 533.5 eV, which were ascribed to O-Fe (lattice oxygen species) and H₂O, respectively. The peaks at 531.5 eV (chemisorbed and dissociated oxygen species) and 534.5 eV (C=O) were observed for the wet-transferred films only. There was a peak at 532.3 eV (C-O) for the dry-transferred films. After annealing at 350°C, however, the wet and dry-transferred films had similar O1s peaks, as depicted in Figure 4.6 (b).

The deconvoluted C1s and O1s regions indicate that there are significant differences between the oxygen and carbon states on the surfaces of the dry and wet-transferred films. However, the wet and dry-transferred films presented similar oxygen and carbon states after annealing at 350°C.

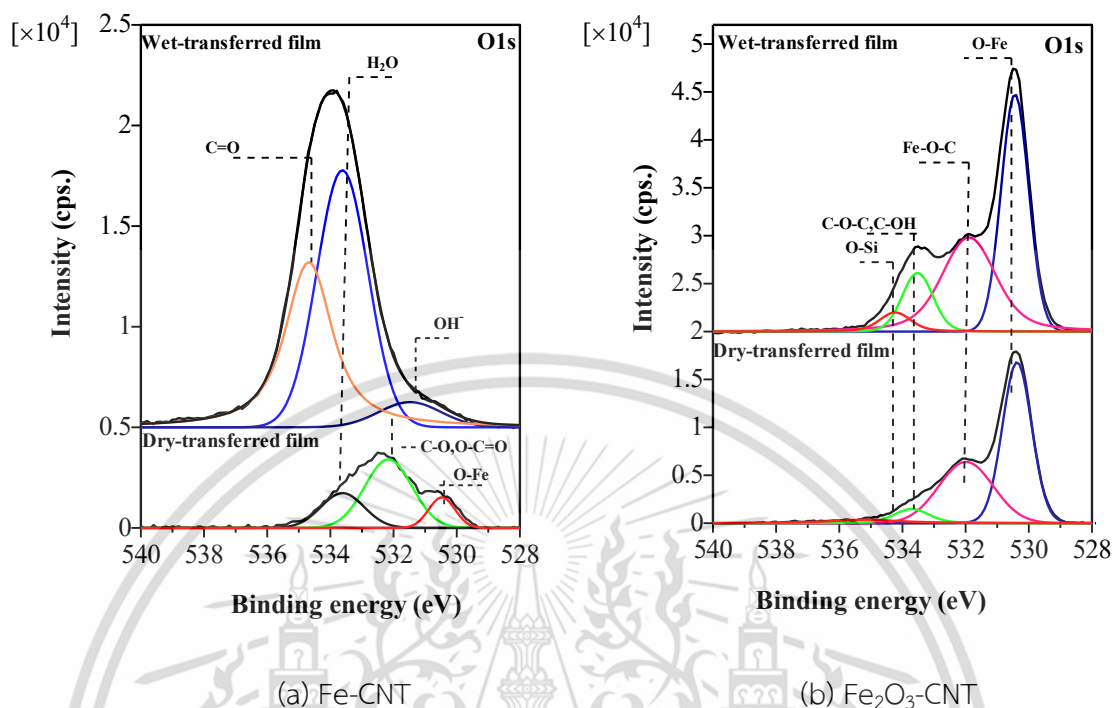


Figure 4.6 XPS spectra for O1s states. The wet-transferred and dry-transferred films (a) before annealing (Fe-CNT) and (b) after annealing (Fe_2O_3 -CNT).

Current–Voltage characteristic

The resistance of films was measured via using the two-probe resistance measurements, which used to investigated the effects of surface contamination on the conduction characteristics of CNTs [99]. Figure 4.7 (a) and (b) present the current–voltage (I–V) characteristic of the films before and after annealing in air at room temperature, respectively. For both dry-transferred and wet-transferred films before annealing (Figure 4.7 (a)), the current increased linearly depending on the voltage indicating that the good contact between the Fe-CNTs and carbon tap/Ag electrode is consistent. Resistance values of the wet-transferred films have higher than that of the dry-transferred films. Since the wet-transferred films are a compact mat-like structure (Figure 4.2 (c)), which leads that the interconnected network is established by the individual/bundle CNTs, resulting in numerous electrical paths can be formed [100]. While I–V curves for the both dry-transferred and wet-transferred films after annealing showed the nonlinear behavior (Figure 4.7 (b)) [99]. The observed nonlinear behavior indicates that Fe_2O_3 formed on CNT surfaces and caused high resistance for both dry-transferred and wet-transferred films after annealing.

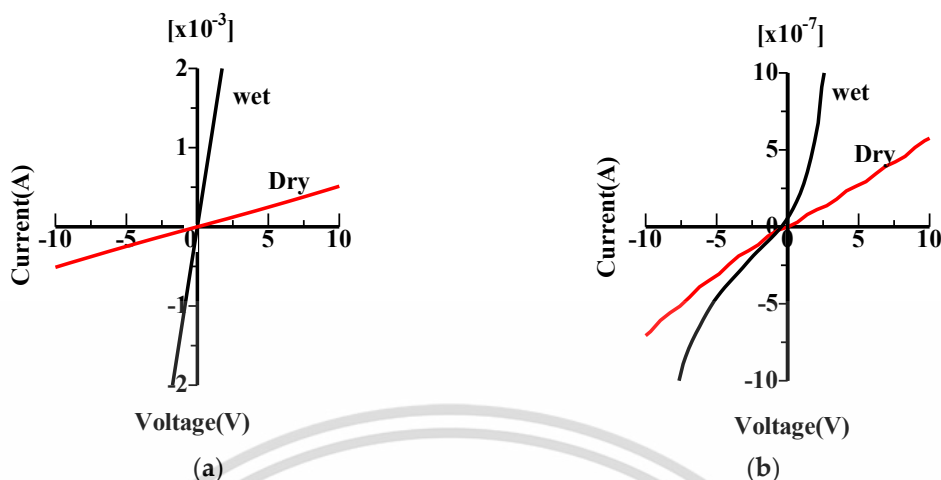


Figure 4.7 Typical I-V characteristic of (a) the dry-transferred and wet-transferred (Fe-CNT) films and (b) the dry- transferred and wet- transferred films ($\text{Fe}_2\text{O}_3\text{-CNT}$).

4.1.3 Various temperature annealing

In this section, optimized temperature for the synthesis of Fe_2O_3 incorporated within CNT films is examined using TGA, FE-SEM and Raman spectroscopy.

TGA

The purity and thermal stability of as-grown (Fe-CNT) films were examined via thermogravimetric and derivative thermogravimetric analysis (TGA-DTG), which is determined by changes in weight at increasing temperatures. In experiment, the as-grown (Fe-CNT) films were prepared by the wet transfer method. They contained impurities at various levels, such as moisture, amorphous carbon, CNT covered with the membrane filter layers, and catalytic metal particles in a graphitic shell. Figure 4.8 shows a TGA - DTG curve revealing three main weight loss peaks at 200°C , 400°C , and 550°C . Initiation of weight lost at 200°C is attributed to the removal of moisture from the sample. The second weight loss at 400°C is attributed to the decomposition of CNT films by air oxidation. This occurred in the temperature range of 350°C - 500°C . The rate of weight change of sample shows maximal weight loss at 400°C and the CNTs are completely decomposed at nearly 500°C . In this work, the decomposition temperature of CNTs is lower than the purified-CNTs due to residual growth catalyst-Fe that acts as an oxidation catalyst [101-103]. Finally, the very small mass loss at temperatures near

550°C may be attributed to the burning of graphite, indicating the presence of very few graphitic shells on films. Additionally, a weight gain was observed at 270°C. This was due to a transformation of Fe metal to iron oxide [41], indicating that a mild oxidative procedure destroys the graphitic shells that encapsulate Fe. The oxidizing the agent reacts with Fe to form Fe₂O₃. Furthermore, an amorphous layer was removed in the temperature range of 300°C - 350°C [41, 102, 104, 105].

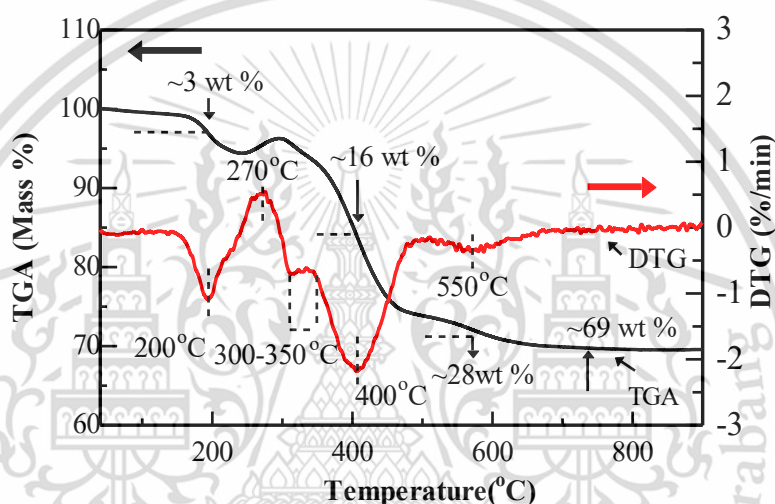


Figure 4.8 Thermal analysis curves (TGA–DTG) of as-grown (Fe-CNT) films.

FE-SEM

Figure 4.9 (a) shows FE-SEM images of as-grown (Fe-CNT) films (or non-annealing) after being transferred onto glass substrates by dissolving them in acetone followed by washing in ethanol and deionized water (the wet transfer). Figure 4.9 (b)-(f) presented FE-SEM images of films annealed at various temperatures, 150, 250, 350, 450, and 550°C, respectively. For the films annealed at 150°C and 250°C, Fe nanoparticles and CNTs stick to each other when subjected to these low annealing temperatures. The films annealed at 350°C and 450°C, show a uniform composite of CNT connected Fe nanoparticles and much void space in materials that provide for good adsorption of gases. However, the films annealed at 550 °C present only Fe nanoparticles due to removal of CNTs by oxidization. As seen in the Figure 4.9 (e) and (f), the nanoparticles had irregular shapes and were aggregated more with increased annealing temperature.

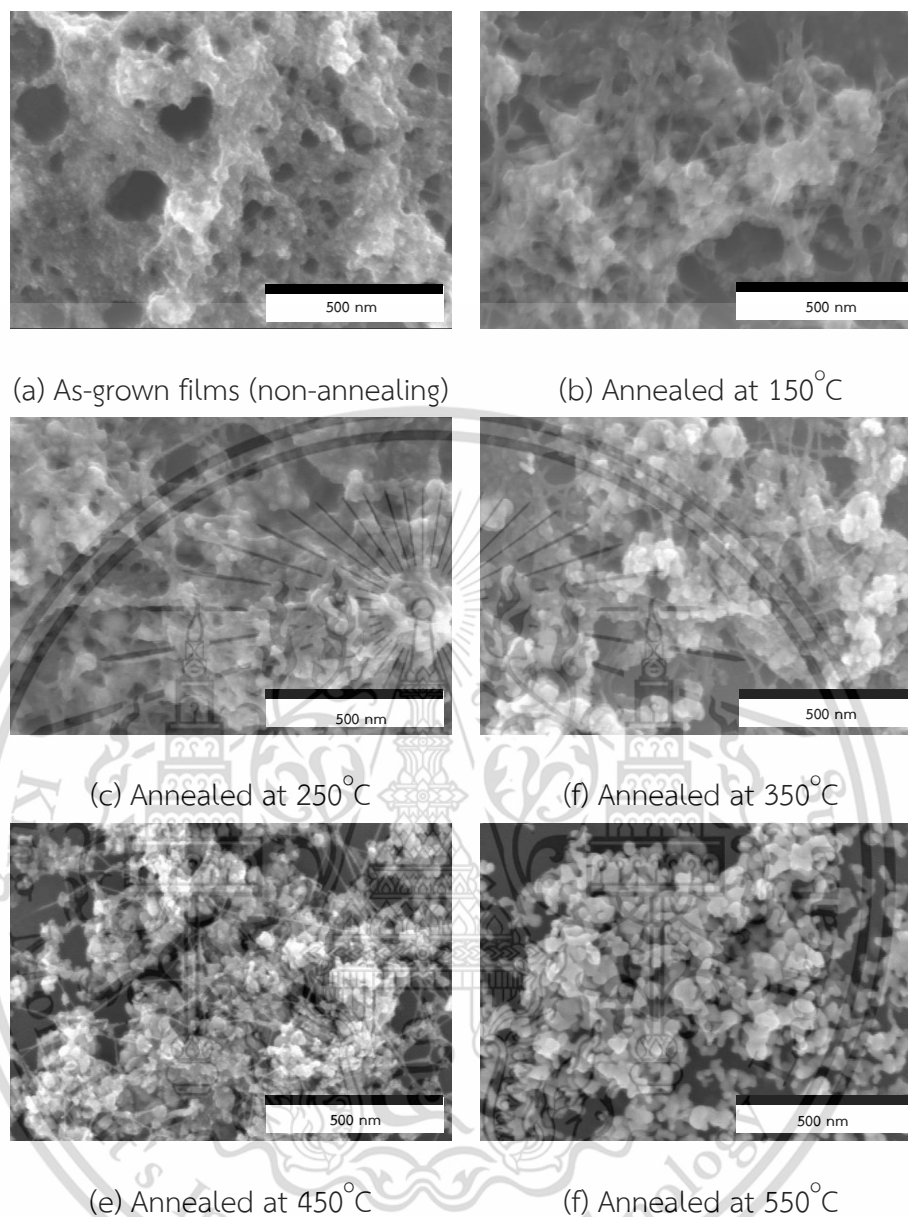
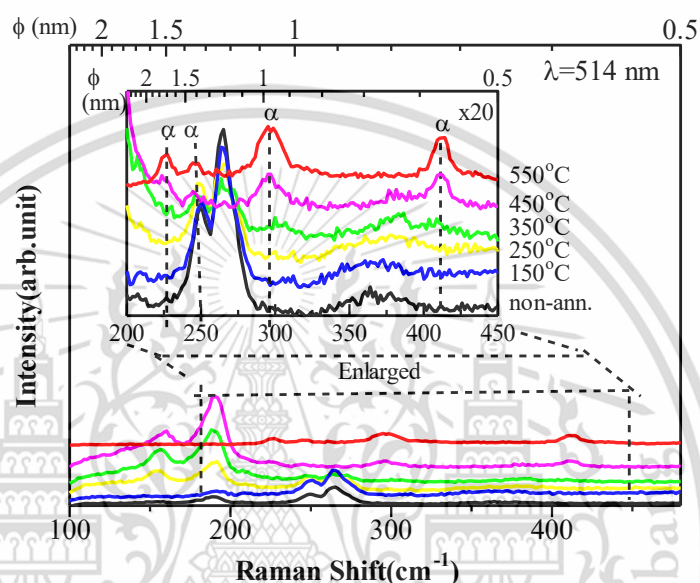


Figure 4.9 Typical FE-SEM image of the as-grown (Fe/CNTs) films at various annealing temperatures.

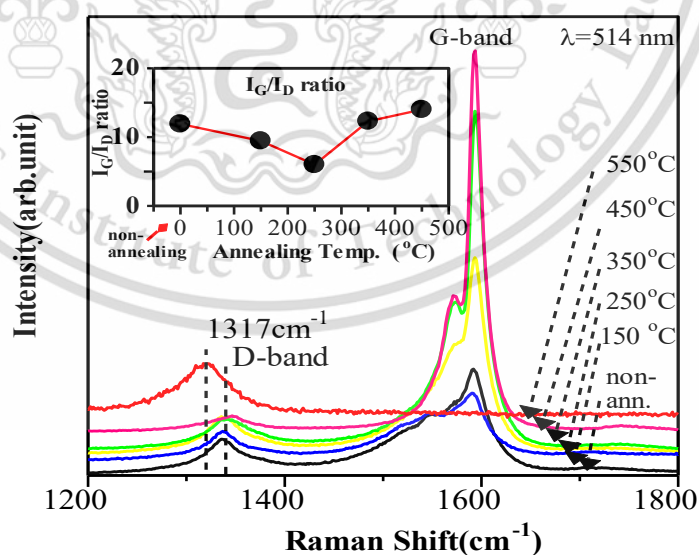
Raman spectroscopy

Characterization of carbon nanotubes was done using Raman spectroscopy. In Figure 4.10 (a), Raman spectra of films were observed in a radial breathing mode (RBM) at $\sim 160 - 265 \text{ cm}^{-1}$, which indicates the single-walled carbon nanotubes with diameters in the range of 0.9 to 1.9 nm. In the inset of Figure 4.10 (a), Raman spectra of purified Fe_2O_3 were also observed in RBM with main peaks at 298 cm^{-1} , 414 cm^{-1} and 1317 cm^{-1} .

(this peak can be seen in Figure 4.10 (b)). Minor peaks at 227 cm^{-1} and 244 cm^{-1} were identified as a hematite ($\alpha\text{-Fe}_2\text{O}_3$) nanostructure [106, 107]. It is notable that purified Fe_2O_3 was obtained from annealing at 550°C , since the CNTs were completely removed by oxidation process. Furthermore, the Raman spectra of Fe_2O_3 were also obtained for CNT films annealed at 350°C - 450°C .



(a) Low-energy region ($100 - 350\text{ cm}^{-1}$)



(b) High-energy region ($1200 - 1700\text{ cm}^{-1}$)

Figure 4.10 Raman spectra ($\lambda_{\text{ex.}} = 532\text{ nm}$) of Fe-CNT films annealed at various annealing temperatures (non-annealed, 150°C , 250°C , 350°C , 450°C , and 550°C).

Figure 4.10 (b) shows the high energy region of a nanotube in a Raman spectrum: D-peak ($\sim 1350 \text{ cm}^{-1}$) and G-peak ($\sim 1580 \text{ cm}^{-1}$). At various annealing temperatures, I_G/I_D is ~ 11.90 (non-annealed), ~ 9.45 (150°C), ~ 6.00 (250°C), ~ 12.33 (350°C), and ~ 14.02 (450°C). The I_G/I_D was found to decrease with increasing annealing temperature over the range of 150°C to 250°C in these experiments. This might have arisen because at these annealing temperatures, the CNT-covered filters became amorphous carbon during the mild oxidation process. However, at higher annealing temperatures ($350\text{--}450^\circ\text{C}$), amorphous carbon was combusted, which is indicated by an increased I_G/I_D ratio. Therefore, this work chose an annealing temperature of 350°C to form Fe_2O_3 in subsequent experiments.

4.1.4 Effect of various deposition times

From the XPS and Raman spectroscopy results, it was confirmed that as-grown (Fe/CNT) films were decorated with metallic Fe. Metallic Fe easily forms $\alpha\text{-Fe}_2\text{O}_3$ in air during annealing at 350°C . In this section, the variation of deposition time affect the morphology of Fe_2O_3 -CNTs was investigated with varying deposition times of 15, 60, and 90 min of as-grown (Fe/CNT) films.

FE-SEM and AFM

Figure 4.11 (a) compared the morphology of as-grown (Fe-CNT) films before, prepared with varying deposition times of 15, 60, and 90 min. As can be seen in the Figure 4.11 (a), the density of as-grown (Fe-CNT) films increased with the deposition time used.

Typical surface morphologies of Fe_2O_3 -CNT films are shown in the Figure 4.11 (b). It can be seen that a CNT network is formed with interconnected Fe_2O_3 nanoparticles. Additionally, small aggregations of Fe_2O_3 particles are observed at the interconnections of network structures, leading to the formation of a highly porous surface. This highly porous Fe_2O_3 /CNT structure is beneficial in LPG sensing applications because the gas molecules are able to easily enter through such a structure.

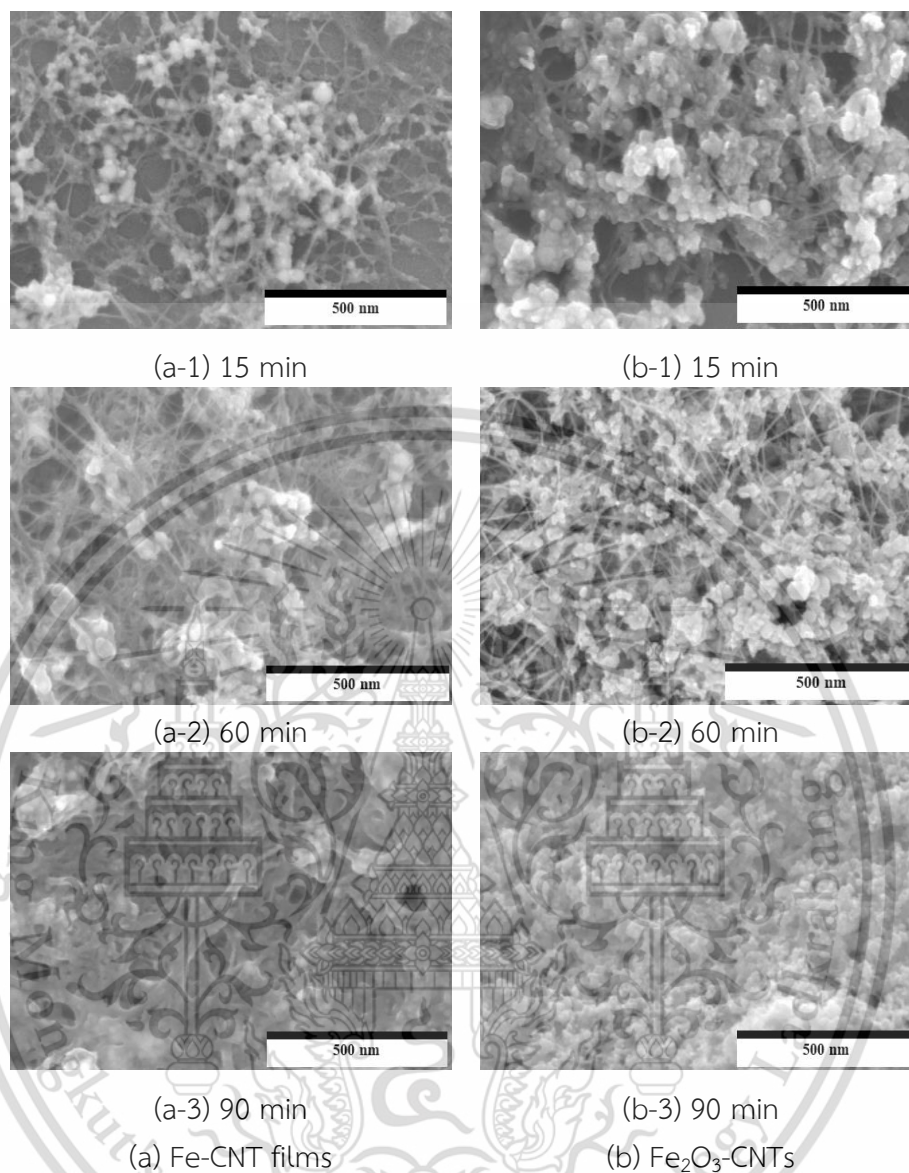


Figure 4.11 Typical surface morphologies of (a) as-grown (Fe-CNT) films and (b) Fe₂O₃-CNT films on silicon substrates.

Figure 4.12 (a) - (c) shows that the AFM images of Fe₂O₃-CNT films. Root mean square (RMS) roughness values of Fe₂O₃-CNT films are ~42, ~120 and ~2 nm for Fe₂O₃-CNT films prepared using deposition times of 15, 60 and 90 min, respectively. In a previous report [108], the sensor response of an LPG sensor increased as a result of its high RMS value. This is because of the increased number of active adsorption sites for oxygen or hydrocarbon molecules on the sensor surfaces.

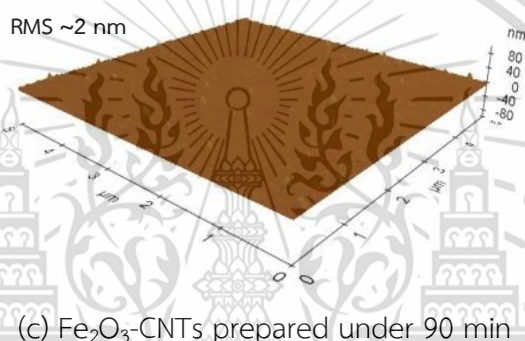
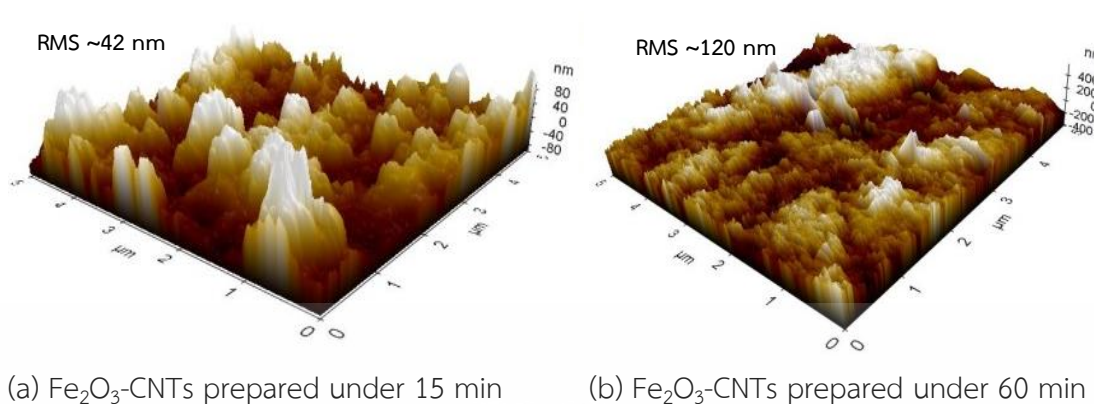


Figure 4.12 Typical AFM images of the Fe_2O_3 -CNT films prepared with the various deposition times. The 3D images were recorded in a $5 \mu\text{m} \times 5 \mu\text{m}$ planar in contact mode.

According to FE-SEM and AFM observations, the porous structure and surface roughness of Fe_2O_3 -CNT films were controlled by deposition time along with the spatial distribution of CNTs and Fe_2O_3 particles. FE-SEM and AFM imagery (Figure 4.11 (f) and Figure 4.12 (c)) of the Fe_2O_3 -CNT films prepared with a deposition time of 90 min clearly indicate that they have a bulk structure and their surfaces are of low roughness. Due to the lower distribution of small particles and CNTs, the material was easily aggregated into a flat surface during the annealing process. The obtained results indicate that choosing a suitable deposition time is necessary to generate useful Fe_2O_3 -CNT films with highly porous structures and high surface roughness.

4.1.5 Comparison with purified CNTs

In this section, the effects of the Fe_2O_3 on the LPG sensing-performance are examined. The LPG sensing-performance of Fe_2O_3 -CNTs is compared with Fe-CNT, purified CNTs, and pure Fe_2O_3 .

Figure 4.13 (a) - (c) illustrate the surface changes of Fe-CNT, Fe_2O_3 -CNTs, and purified CNTs, respectively. Fe_2O_3 -CNTs are network on films connected α - Fe_2O_3 nanoparticles with irregular pores morphologies. The annealed films showed that the many small island-like structures represent nanoparticles directly connected to the nanotube surfaces, which CNTs act as a bridge.

The Fe_2O_3 -CNTs was then purified using HCl, resulting primarily in CNT bundles and smooth surface, as shown in Figure 4.13 (c). The most of the Fe_2O_3 nanoparticles were removed by HCl. However, the purified CNTs were mostly bundle-shaped and contained some metal catalyst particles.

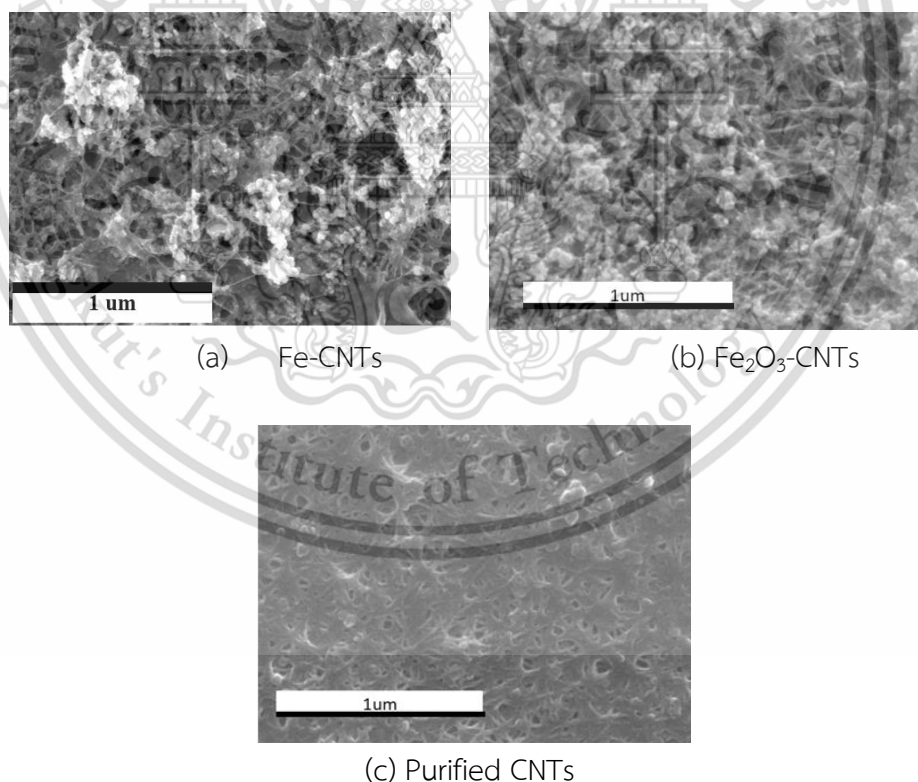


Figure 4.13 Morphology of (a) Fe-CNT films, (b) Fe_2O_3 -CNTs), and (c) purified CNTs).

Figure 4.14 presents the Raman spectra of Fe and CNTs in films. To characterize CNTs, Figure 4.14 (a) depicts the Raman spectra of all the films observed at low-energy or RBM mode ($100 - 350 \text{ cm}^{-1}$), except for purified Fe_2O_3 . The Raman spectra were presented in the range of 100 to 350 cm^{-1} , which confirmations that SWNTs were mixed in the films. The diameter of SWNTs was calculated from the Raman peaks at $\sim 160 - 265 \text{ cm}^{-1}$, corresponding to diameters varying from $\sim 0.9 \text{ nm}$ to 1.5 nm . However, 0.5 nm diameters CNTs are easily removed by oxidizing in air at 350°C . As for the purified Fe_2O_3 , the RBM peaks of SWNTs were not observed. Small peaks at 227 cm^{-1} , 248 cm^{-1} , 298 cm^{-1} , and 414 cm^{-1} were observed that were ascribed to $\alpha\text{-Fe}_2\text{O}_3$, similar to those reported in previous $\alpha\text{-Fe}_2\text{O}_3$ studies. Figure 4.14 (b) presents Raman spectra in a high-energy region ($1200 - 1700 \text{ cm}^{-1}$). The peak intensity of the G-band ($\sim 1590 \text{ cm}^{-1}$) indicates formation of well-graphitized carbon nanotubes. These were observed in Fe-CNT films, Fe_2O_3 -CNTs, and purified CNTs. The D-band ($\sim 1350 \text{ cm}^{-1}$) is associated with disordered graphite structures or amorphous carbon. The purity of CNTs is evaluated using the intensity ratio of the G and D bands (I_G/I_D). A higher ratio indicates a lower level of defects, and therefore better structural quality [86]. The I_G/I_D ratios of Fe-CNT films and Fe_2O_3 -CNTs are 11.9 and 12.3 , respectively. It can be seen that the I_G/I_D of Fe_2O_3 -CNT films was greater than that of Fe-CNT films. The I_G/I_D results indicate that the purity of CNTs increased and that the structure of the CNTs was not damaged even with air annealing. Moreover, the ratio I_G/I_D increased to ~ 14.8 after the removal of Fe_2O_3 , which was observed in purified-CNT films.

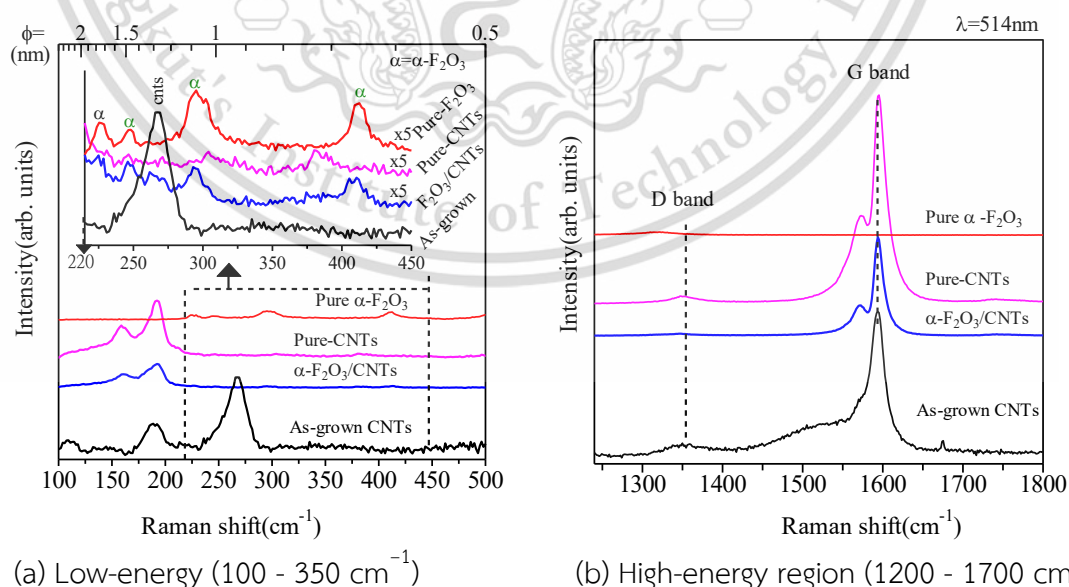


Figure 4.14 Raman spectra of the samples.

4.2 LPG gas sensing properties

4.2.1 Effect of dry and wet methods

To determine the LPG sensing-performance, the dry and wet-transferred films before and after the formation of Fe_2O_3 were exposed to 5 vol.% of LPG at operating room temperature, as depicted in Figure 4.15.

Sensitivity of dry-transferred Fe-CNTs was found to be $\sim 0.6\%$, higher than for the wet-transferred Fe-CNTs ($\sim 0.4\%$). While, Figure 4.15 (b) depicts that the Fe_2O_3 -CNT composite films are n-type gas-sensing materials. The sensitivity of the wet-transferred $\text{Fe}_2\text{O}_3/\text{CNTs}$ was found to be $\sim 3.0\%$, higher than for the dry-transferred Fe_2O_3 -CNTs ($\sim 0.6\%$). The Fe_2O_3 -CNT films obtained from the wet process showed significantly rapid response and recovery times that are $\sim 10\text{s}$ and 59s , respectively. The dry process exhibited longer response and recovery times ($\sim 90\text{s}$ and N/A). It can be seen that the wet-transferred Fe_2O_3 -CNTs provide higher gas-sensing performance than dry-transferred Fe_2O_3 -CNTs. This is attributed to mesoporous morphology of wet-transferred Fe_2O_3 -CNTs, which is present in Figure 4.3 (b). In contrast, the morphology of dry-transferred Fe_2O_3 -CNTs is a compact mat-like structure. These compact structures reduce an area of adsorption, resulting in decreased sensitivity and long recovery time. Furthermore, there are reported that the sensitivity of gas sensors is increased with the functional groups on CNTs [59].

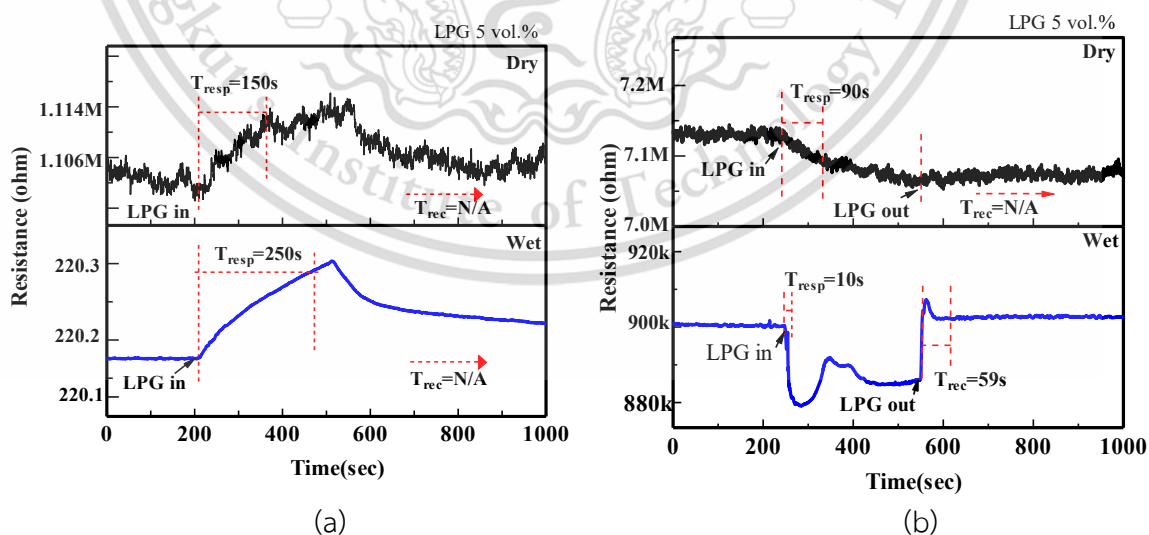


Figure 4.15 Comparison of the response of the dry and wet-transferred Fe_2O_3 -CNTs film sensors to 5% of LPG at room temperature.

Additionally, the sensing mechanisms of films are examined. Both of the dry and wet-transferred films before the formation of Fe_2O_3 exhibited the increased resistance upon exposure to a reducing gas like LPG. This indicates that Fe-CNT composite films are p-type gas-sensing materials, as depicted in Figure 4.15 (a). The p-type LPG sensing behavior observed in raw Fe-CNT, which resulted from the CNT sensing while the Fe catalyst was encapsulated within carbon cages [109]. P-type material, that has a large number of hole carrier. The level of holes will be decrease dramatically with reducing gas (LPG) exposure. This is due to an electron injection by the reducing gas into a p-type material resulting in increased resistance of the sensor [110].

Fe_2O_3 -CNT films display an n-type sensing behavior due to the formation of Fe_2O_3 that are n-type gas-sensing materials, and are shown in Figure 4.15 (b). For Fe_2O_3 -CNT films, both the CNTs and Fe_2O_3 can be sensing materials. Thus the sensing mechanism of Fe_2O_3 -CNT films is examined via the removal of Fe_2O_3 in Fe_2O_3 -CNT films, which explained in next section. Moreover, the LPG-sensing process of the Fe_2O_3 -CNT nanocomposite generates a charge between Fe_2O_3 and LPG molecules to electron transport through the CNT nanostructure. The CNT behaves as the electrical conduction pathway between Fe_2O_3 grain boundaries due to the high carrier mobility of CNT. Furthermore, Fe_2O_3 -CNT thin films obtained wet transfer had a significant rapid response and recovery occurs. It is attributed to the rapid changes in p-n heterojunction of n- Fe_2O_3 and p-CNTs hybrid films, during LPG atmosphere.

4.2.2 Effect of various temperature annealing

Figure 4.16 (a) depicts all the Fe_2O_3 -CNT films' dynamic resistance curves compared to the Fe-CNT films (non-annealed) when exposed to LPG (5 vol% LPG). It is notable that the films annealed at 450°C and 550°C had an extremely high resistance at room temperature, but outside the limit of our instrument's operating range. All Fe_2O_3 -CNTs exhibited decreased resistances, showing n-type behaviors. The purity of CNTs annealed at 150°C was higher than at 250°C . However, the Fe_2O_3 -CNTs was annealed at 250°C demonstrated a greater sensor response than those produced at 150°C . This may be attributed to incomplete combustion of cellulose on the Fe_2O_3 -CNT sensing films, as demonstrated in the FE-SEM imagery of in Figure 4.9 (c). Moreover, the films annealed at 350°C demonstrated a maximal sensor response and rapid response and recovery times ($\sim 3\%$, $\sim 10\text{s}$ and 60s), as shown in Figure 4.16 (b).

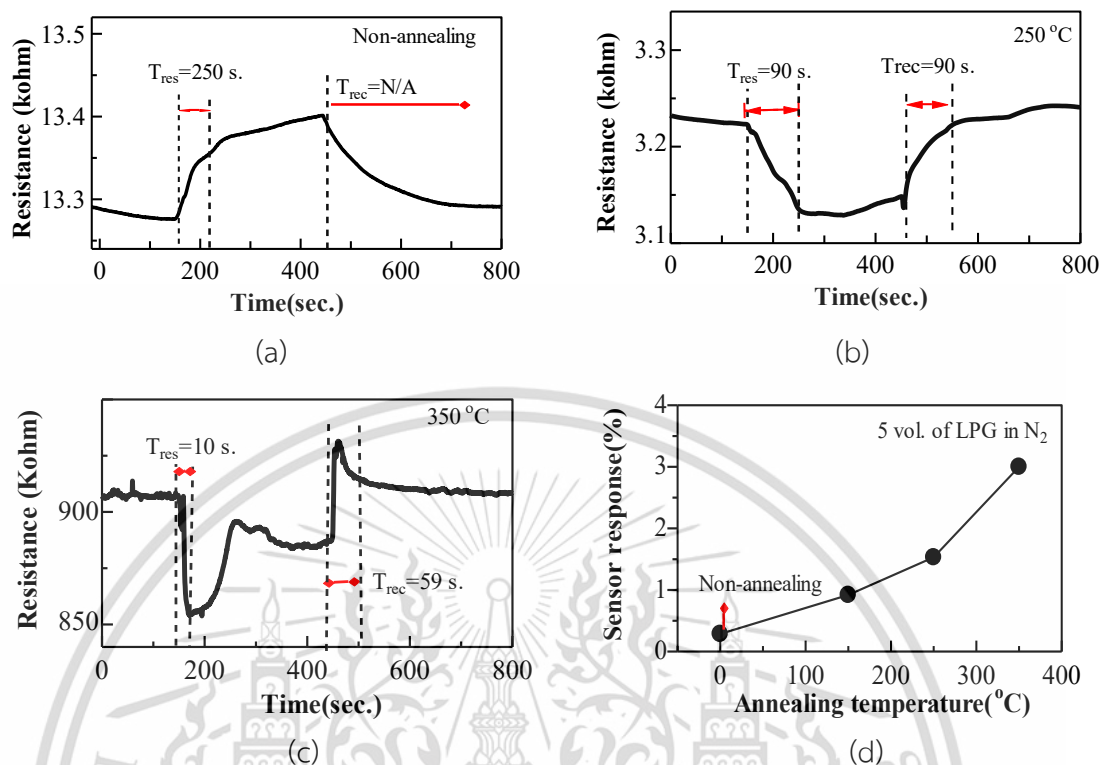


Figure 4.16 (a) Typical dynamic resistance curves and (b) corresponding sensor response of sensors annealed at various temperatures (from top-to-bottom: Fe-CNTs (non-annealed), 250 °C, and 350 °C) in 5vol.% of LPG.

4.2.3 Effect of various deposition Times

In this section, the effect of deposition time on LPG sensing is investigated. In an experiment, Fe₂O₃-CNT films were prepared using varying deposition times of 15, 30, 45, 60, 90, and 120 min. The LPG sensing-performance of all Fe₂O₃-CNT films were examined with LPG concentration of 5 vol.%, as depicted in Figure 4.17. The results indicate that the sensitivity of sensors is increased with the increase in deposit times. Fe₂O₃-CNT films prepared with a deposition time of 45 min yielded a maximal response of ~ 5.5 % at 5 vol. % of LPG. This is attributed to a highly porous structure and high roughness, which is increased with deposition times. However, the Fe₂O₃-CNT films' surface is a pack structure when it is fabricated with a long deposition time such as 90 min, as depicted in FE-SEM (Figure 4.11 (f)) and AFM images (Figure 4.12 (c)), which results in decreased sensitivity of sensors. The sensing film with short (15 min) and long deposition (90 min) showed the lower sensitivity with fast response times (15 min, $S \sim 0.9$ % , $T_{resp.} = 6.5$ s and 90 min, $S = \sim 1.0$ % , $T_{resp.} = 6.5$ s). Note that the Fe₂O₃-

CNT films with a deposition time of 120 min had a high thickness of the film that results in their extremely high resistance at room temperatures; instruments (in this work) were unable to measure this parameter.

To examine multiple-cycle sensing performance under an air environment, the Fe_2O_3 -CNT films were measured under various LPG concentrations of 0.1, 0.4 and 0.7 vol.% diluted in zero air. These results are depicted in Figure 4.18. The electrical resistance of these sensors decreased upon LPG exposure and increased after replacing LPG laden air with zero air. The sensor response, response and recovery times of Fe_2O_3 -CNTs are shown in Figure 4.18 are summarized in Figure 4.19. It is observed that sensor response, response and recovery times were stable and nearly equal at each concentration, indicating a good reproducibility of sensing performance. Moreover, the Fe_2O_3 -CNT films could detect LPG at concentrations of less than 0.5 vol.%, which corresponds to the 25% lower explosive limit (LEL) of LPG. The LEL is defined as the minimum concentration of LPG contained in the air which sufficient to propagate a flame when exposed to a source of ignition.

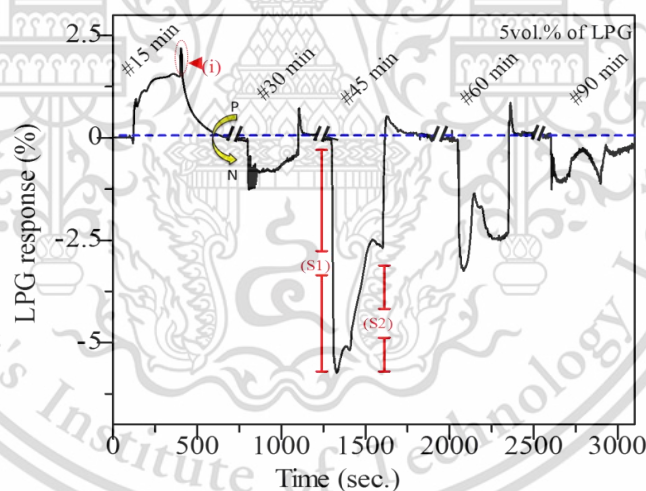


Figure 4.17 Sensing performances of Fe_2O_3 -CNT films prepared under various deposition times of 15, 30, 45, 60 and 90 min.

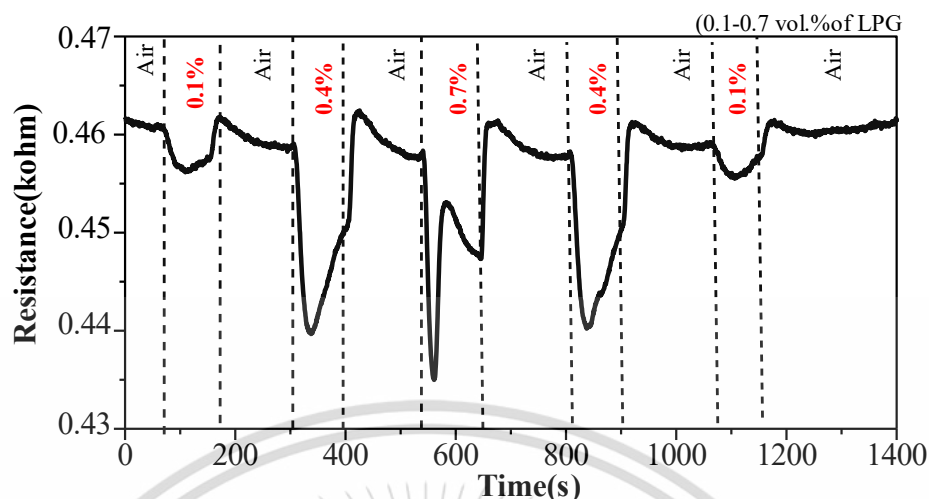


Figure 4.18 Dynamic responses of Fe_2O_3 -CNT films to LPG concentrations varying from 0.1–0.7 vol.%.

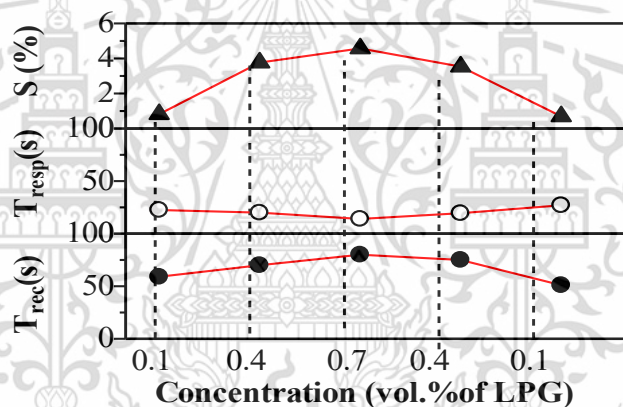


Figure 4.19 Summary of the sensing properties of Fe_2O_3 -CNT films to LPG concentrations varying from 0.1–0.7 vol.%.

4.2.4 Comparison with purified CNTs

The LPG sensing-performance of films before and after removed Fe_2O_3 in Fe_2O_3 -CNTs is depicted in Figure 4.20. Change in the resistance of as-grown CNTs, α - Fe_2O_3 -CNTs, and purified CNTs sensors in the presence of LPG at various concentrations. The baseline resistances in N_2 for as-grown CNTs, Fe_2O_3 -CNTs, and purified CNTs were approximately 2.5 k Ω , 1.9 M Ω and 360 k Ω , respectively. Figure 4.20 (a) presents that the p-type LPG sensing behavior is observed for as-grown films, which resulted from the CNTs sensing while the Fe catalyst was encapsulated with carbon [109]. Meanwhile, Fe_2O_3 -CNT films display an n-type sensing behavior due to the formations of Fe_2O_3 that

act as an LPG sensing. It is well known that the sensing behavior of gas sensor has been related to the properties of sensing materials such as p-type material, which had a hole majority carriers. The amount of hole will be decreased dramatically when reducing gas (LPG) exposure, due to an electron of reducing gas was injected to p-type material resulting in increased resistance of the sensor [110]. This could explain the sensing behavior of as-grown CNTs and Fe₂O₃-CNTs composite-based on LPG sensor. Figure 4.20(c) clearly depicts that the sensing behavior of CNTs without α -Fe₂O₃ is p-type.

Figure 4.20 (d) presents the sensor response, Fe₂O₃-CNT films showed the maximum in response along with fast response/recovery time, while as-grown films and purified CNT films had a low response. This was due to the fact that high bonding energy among LPG atoms allows limited electron transfer from LPG molecules to the CNTs [111]. However, the purified-CNTs had a quick response/recovery time because of the highly purified CNTs than that of CNT films. These results indicate that the Fe₂O₃-CNT films had an excellent responsive to detect the LPG.

Moreover, we observed that the time response of Fe₂O₃-CNTs was faster than that of as-grown CNTs. This observation can be explained by the different sensing mechanism. For as-grown films, the response is attributed to the adsorption between the LPG and the surface of the carbon nanotube. On the other hand, the fast-response of Fe₂O₃-CNT films might be due to the sensing process of the interface between the CNTs and the Fe₂O₃. According to this mechanism, the quick response of Fe₂O₃-CNT-based sensors could be attributed the Schottky barrier formed at α -Fe₂O₃ and CNTs junction [112]. Moreover, the annealing in air could be improved the response time of Fe₂O₃-CNT films[80].

Furthermore, the sensitivity of sensors (purified CNT materials) reduced after the removal of Fe₂O₃ from Fe₂O₃/CNT films. The sensitivity value reduced from ~3.0% to ~0.4% (for 5vol.% of LPG), as shown in Figure 4.8 (d). This indicates that the main contributor for the charge exchange during LPG adsorption of Fe₂O₃-CNT films is the n-type Fe₂O₃. The sensing mechanism of n-type Fe₂O₃ can be describes using following paragraph.

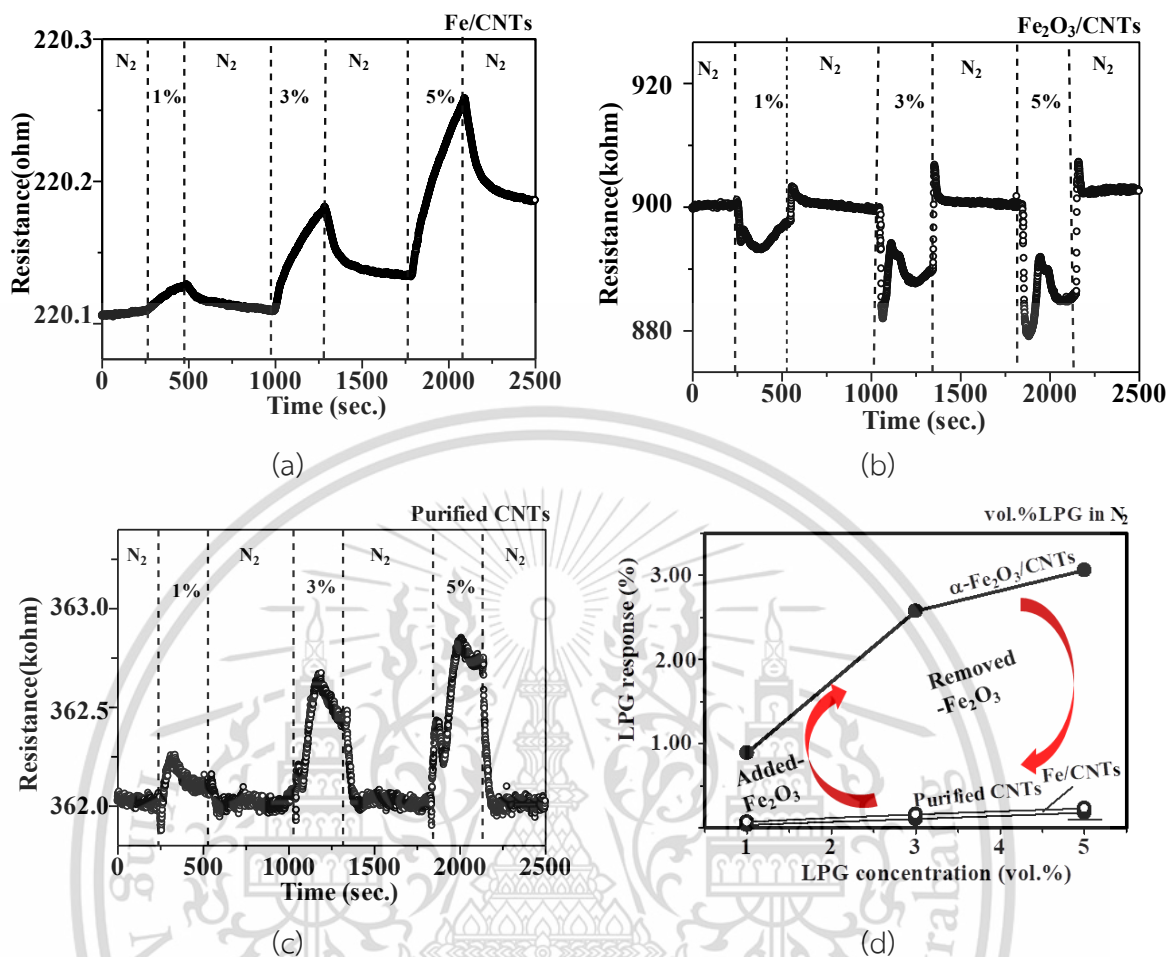


Figure 4.20 Dynamic responses of (a) Fe-CNT films, (b) Fe₂O₃-CNT films, and (c) purified CNTs, to LPG in air atmosphere, and, (d) Sensor responses of various sensor types to concentrations of LPG from 1–5 vol.%.

4.3 LPG sensing mechanism

As-grown Fe-CNT films and purified CNTs

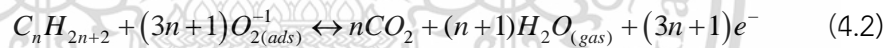
From the results, the resistance changing behaviors of Fe-CNT films and purified CNT films may be attributed to the physical adsorption of LPG molecules on the CNTs. P-type CNT sensing behavior is attributed to charge transfer or electronic interactions between CNTs and adsorbed molecules [113]. For interaction between CNTs and LPG (reducing gas: electron donor), the LPG molecules transfer electrons to the CNTs, which recombined with hole carriers. Therefore, the hole carrier density in the CNTs was reduced and consequently increased the electrical resistance.

Fe₂O₃-CNT films

The resistance changing behaviors of Fe₂O₃-CNT hybrid thin films may be attributed to the adsorption and desorption (Chemisorption) of LPG molecules on the Fe₂O₃-CNT nanocomposite sensing film. The LPG-sensing mechanisms at room temperature may be explained based on the formation of p-n heterojunctions between p-type CNT and n-type metal-oxide-semiconductor of Fe₂O₃. In air, ambient oxygen adsorbs and captures electron from the conduction band of Fe₂O₃ and the Fermi level of CNT to generate oxygen adsorbate (O_2^-) at room temperature shown in Eq. (4.1) and leading to the formation of surface depletion layers on the interface of the Fe₂O₃-CNT sensing film and cause the high resistance of the sensor in air.

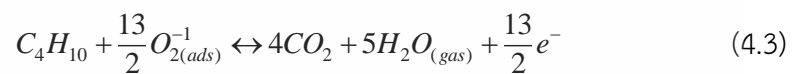


Upon exposure to LPG, LPG molecules as a reducing gas will react with O_2^- according to the reaction [108, 114]

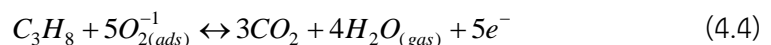


Here, $C_n H_{2n+2}$ represents a mixture of hydrocarbons like propane (C_3H_8 ; $n=3$) and butane (C_4H_{10} ; $n=4$).

For C_4H_{10}



For C_3H_8



This reaction (Eq. (4.3) and Eq. (4.4)) leads to discharge of electrons into the conduction band of Fe_2O_3 on the sensor surface. This process results in a decrease of the thickness of the electron depletion layer leading to decrease in the resistance of the sensors. Moreover, the differences in the sensing mechanism of Fe_2O_3 -CNT films prepared with various deposition times, which are observed in Figure 4.17. Fe_2O_3 -CNT films present both n- and p-type behaviors were observed. "S1" and "S2" are defined as the response of n- and p-type sensors, respectively. Fe_2O_3 -CNT films prepared in 15 min showed p-type sensing behavior while those prepared with deposition times of 30, 45, 60, and 90 min showed n-type sensing behavior. This indicates that specific sensor behaviors were attributed to the deposition time, as shown in Figure 4.12 .



Figure 4.21 Sensing mechanism of (a) CNTs decorated with discrete Fe_2O_3 particles and CNTs covered with Fe_2O_3 particles.

Furthermore, all Fe_2O_3 -CNT films exhibited an excessive recovery (point "i"; Figure 4.17), which was also reported by Dai et al. [115] for a gas sensor made of monolayer Fe_2O_3 . They explained that the origin of the excessive recovery is due to a one-electron response, one initial electron recovery, and two - electrons eventual recovery. In this work, the one-electron response was received from the LPG molecules. A two-electron recovery might originate from oxygen intermediates gases ($\text{C}_n\text{H}_{2n}\text{O}$) due to the highly active sites on Fe_2O_3 .

4.4 Comparison with other sensors

Moreover, literature review (Table 4.1) shows that various materials were used in LPG sensor applications that can work at room temperature. In this work, Fe_2O_3 -CNT films-based LPG sensors exhibited a fast response/recovery times, and open the door for promising applications in LPG leak detection at room temperature.

Table 4.1 Nanocomposite material-based LPG sensors operating at room temperature

Years ^[Ref.]	Materials	LPG(vol.%)	S (%)	T _{resp.} @90%	T _{rec.} @90%
2011 ^[1]	Ferric oxide	2.0	5100.0	~120 s	~150 s
2013 ^[116]	Ppy/TiO ₂	0.10	55.0	~112 s	~130 s
2013 ^[117]	PTh/SnO ₂	0.5-2.5	~9.5-56.2	~196-94 s	~182-466 s
2014 ^[118]	CuO-SnO ₂	0.5	~4200.0	~180 s	~200 s
2014 ^[119]	PANI/ γ -Fe ₂ O ₃	0.02	~140	~60 s	N/A
2014 ^[21]	ZnFe ₂ O ₄	5.0	~1600.0	~120 s	~150 s
2014 ^[120]	Cu ₂ ZnSnS ₄	0.12	~20.0	~70 s	~40 s
2016 ^[121]	Cu ₂ ZnSnS ₄	0.1	~60.0	~40 s	~40 s
2017 ^[122]	BaTiO ₃	0.5	50	~30 s	~60 s
This Study	Fe-CNTs	5.0	~0.25	~290 s	N/A
	Purified CNTs	5.0	~0.25	~20 s	~45 s
	Fe ₂ O ₃ -CNTs	0.1-5.0	~1.0-6.0	~25-13 s	~30-80 s

CHAPTER 5

CONCLUSIONS

LPG is widely used in daily life; however, LPG is a flammable gas. To avoid gas explosions, LPG sensors are needed. Conventional LPG sensors are fabricated using metal oxide (MOx), which require the heater (or temperature of 200°C – 500°C) for their optimal sensing performance. This could cause an increase in power consumption, complexity, and higher operating costs. In the present, the choosing a suitable material have attracted much attention to reducing the operating temperature of LPG sensor.

5.1. Materials

In this dissertation reports the fabrication of Fe₂O₃-CNT films as room-temperature LPG sensor. The vertical floating catalyst chemical vapor deposition method is used to prepare Fe₂O₃-CNT films because they are simple, inexpensive, and suitable for large-scale production. Transmission Electron Microscopy (TEM) images represent that primary films consist of randomly oriented entangled CNTs and are adhered with Fe nanoparticles (average particle size of ~7.33 nm). CNTs and Fe₂O₃ with alpha (α) phase were confirmed by Raman spectroscopy and X-ray Photoelectron Spectroscopy (XPS), respectively. Thermogravimetric analysis (TGA) and derivative thermogravimetric analysis (DTG) was used to investigate the composition and thermal stability of CNTs. For various annealing temperatures (150, 250, 350, 340, 550°C), at 350°C is the optimum annealing temperature for the transformation of metallic Fe to Fe₂O₃ with high purity of CNTs. The optimum synthesis process of Fe₂O₃-CNT thin films is the wet process when compared with the dry process (without any using solution). Field-emission Scanning Electron Microscopy (FE-SEM) presents that the surface morphology of Fe₂O₃-CNT films obtained in the wet process was the mat-like structure and obtained in the dry process was the branch-like structure. Moreover, I-V curves for both dry-transferred and wet-transferred films after annealing showed the nonlinear behavior. This behavior also indicates that Fe₂O₃ formed on CNT surfaces and caused high resistance for both dry-transferred and wet-transferred films after annealing. The surface morphology (RMS roughness) was further investigated through Atomic Force Microscopy (AFM). RMS of Fe₂O₃-CNTs thin

films increased with an increased deposition time of Fe-CNT films (controlling by mist-CVD method). Prior to the sensing test, the sensing films were placed on substrates (1 cm x 1 cm), and then the two carbon tap/Ag electrodes were placed on sensing films for electrical measurement.

5.2. LPG gas sensing properties

5.2.1 Effect of sensing material on LPG sensing

As-grown film (Fe-CNTs), Fe₂O₃-CNTs, purified CNT, and purified Fe₂O₃ was used as the LPG gas sensors. The gas sensing performances of films were investigated for 5 vol.% of LPG with the operating at room temperature. For sensor test, the as-grown film and purified CNT sensors had p-type response to these LPG. The Fe₂O₃-CNTs sensors had n-type response to LPG with rapid response and recovery times within seconds. The Fe₂O₃-CNTs sensor showed higher sensitivity and shorter response time ($S = \sim 3\%$, $T_{\text{resp.}} = 10$ s, $T_{\text{rec.}} = 59$ s). The purified CNT sensor showed the poor sensitivity with dramatic response and recovery time ($S = \sim 0.25\%$, $T_{\text{resp.}} = \sim 20$ s, $T_{\text{rec.}} = \sim 45$ s). The as-grown Fe-CNT sensor showed the lower sensing characteristics such as the lower sensitivity and the slower response and recovery times ($S = \sim 0.25\%$, $T_{\text{resp.}} = \sim 20$ s, $T_{\text{rec.}} =$ incomplete recovery times). The sensor's characteristics to reducing LPG gas were found to be significantly dependent on the type of materials. This is because the LPG-sensing process of the Fe₂O₃-CNT nanocomposite generates a charge between Fe₂O₃ and LPG molecules to electron transport through the CNT nanostructure. The CNT behaves as the electrical conduction pathway between Fe₂O₃ grain boundaries due to the high carrier mobility of CNT. Furthermore, Fe₂O₃-CNT thin films obtained wet transfer had a significant rapid response and recovery occurs. It is attributed to the rapid changes in p-n heterojunction of n-Fe₂O₃ and p-CNTs hybrid films, during LPG atmosphere.

5.2.2 Effect of synthesis Fe₂O₃-CNTs films (by the wet and dry process)

Fe₂O₃-CNTs sensing films were synthesized by wet and dry process. The sensing reaction was measured under 5 vol.% of LPG with the operating at room temperature. Before annealing, as-grown Fe-CNTs was prepared on substrate by wet and dry process. Under 5 vol.% of LPG, the sensing behaviors of both types of as-grown Fe-CNTs sensing films (wet and dry) had p-type response to these LPG. The response and recovery times of both types of sensing films were long response and incomplete recovery time. The sensing behaviors of both types of Fe₂O₃-CNTs sensing films (the wet and dry process)

had n-type response to these LPG. The response and recovery times of Fe₂O₃-CNTs sensing films (dry process) was long response and incomplete recovery time. The Fe₂O₃-CNTs (the wet process) sensor showed higher sensitivity and shorter response time (to 5vol.% of LPG, $S = \sim 3\%$, $T_{\text{resp.}} = 10$ s, $T_{\text{rec.}} = 59$ s) than Fe₂O₃-CNTs (the dry process) sensor (to 5vol.% of LPG, $S = \sim 1.4\%$, $T_{\text{resp.}} = 90$ s, $T_{\text{rec.}} =$ incomplete recovery). The process had effects on the surface morphology and sensor characteristics.

5.2.3 Effect of various annealing temperatures on LPG sensing

Fe₂O₃-CNT sensing films were prepared by various annealing temperatures ranging from 250 to 550°C. The sensor characteristics to reducing LPG gas showed remarkable dependence on the annealing temperatures of films. The sensing reaction was measured in 5 % vol. of LPG. The sensitivity increased with decreasing the annealing temperatures. It can be observed that the annealing temperatures increased with the aggregation of Fe₂O₃ nanoparticles and the removal of amorphous carbon and the remaining MCE membrane gel, which decreased the surface area and connectivity of films due to the discontinuity of CNTs. For the sensor test, the sensing film (annealing at 250°C) showed the sensing characteristics such as the sensitivity and the slower response and recovery time times ($S = \sim 1.5$, $T_{\text{resp.}} = 90$ s, $T_{\text{rec.}} = 90$ s). The sensing film (annealing at 350°C) showed the highest sensitivity and the fastest response times ($S = 3\%$, $T_{\text{resp.}} = 10$ s, $T_{\text{rec.}} = 60$ s).

5.2.4 Effect of various deposition times on LPG sensing

Fe₂O₃-CNT sensing films were prepared from Fe-CNT films which the film deposition time ranged from 15 to 120 min (controlling from the mist-CVD method). The sensitivity and response time drastically increased and decreased respectively with decreasing the film deposition time. It can be observed that the film deposition time increased with the amount of Fe₂O₃ particles and CNTs. The sensor characteristics to reducing LPG gas showed remarkable dependence on the amount of Fe₂O₃ particles and CNTs. The amount of Fe₂O₃ particles and CNTs had effects on the sensor characteristics. For the sensor test, under 5 vol.% of LPG, the sensing film (deposition time 45 min) showed the highest sensitivity and the fastest response and recovery times ($S = \sim 5.5\%$, $T_{\text{resp.}} = 14$ s, $T_{\text{rec.}} = 14$ s). The sensing film with short (15 min) and long deposition (90 min) showed the lower sensitivity with fast response times (for 15 min, $S = \sim 0.9\%$, $T_{\text{resp.}} = 6.5$ s and for 90 min, $S = \sim 1.0\%$, $T_{\text{resp.}} = 6.5$ s). This is because of the increased number of active adsorption sites for oxygen or hydrocarbon molecules on the sensor surfaces.

Furthermore, Fe_2O_3 -CNT films showed that it could detect LPG concentration at lower value than 25% of LEL with response/recovery time of less than 30 seconds at room temperature. Moreover, literature review (Table 4.1) shows that various materials were used in LPG sensor applications that can work at room temperature. These results suggest that the Fe_2O_3 -CNT films are challenging materials for monitoring LPG operating at room temperature. The effect of deposition time, temperature annealing, and sensing mechanism of α - Fe_2O_3 -CNT films on LPG sensing are investigated in this dissertation.



REFERENCES

- [1] Yadav, B., et al. 2011. "Nanonails structured ferric oxide thick film as room temperature liquefied petroleum gas (LPG) sensor." **Applied Surface Science**. 257(6): 1960-1966.
- [2] Sun, Y.-F., et al. 2012. "Metal oxide nanostructures and their gas sensing properties: a review." **Sensors**. 12(3): 2610-2631.
- [3] Thomas, B. and B. Skariah 2015. "Spray deposited Mg-doped SnO₂ thin film LPG sensor: XPS and EDX analysis in relation to deposition temperature and doping." **Journal of Alloys and Compounds**. 625: 231-240.
- [4] Pourfayaz, F., et al. 2005. "CeO₂ doped SnO₂ sensor selective to ethanol in presence of CO, LPG and CH₄." **Sensors and Actuators B: Chemical**. 108(1): 172-176.
- [5] Kumar, R., et al. 2020. "Room-Temperature Gas Sensors Under Photoactivation: From Metal Oxides to 2D Materials." **Nano-Micro Letters**. 12(1): 1-37.
- [6] Barsan, N. and U. Weimar 2001. "Conduction model of metal oxide gas sensors." **Journal of electroceramics**. 7(3): 143-167.
- [7] Wang, C., et al. 2010. "Metal oxide gas sensors: sensitivity and influencing factors." **Sensors**. 10(3): 2088-2106.
- [8] Van Hieu, N., et al. 2008. "Highly sensitive thin film NH₃ gas sensor operating at room temperature based on SnO₂/MWCNTs composite." **Sensors and Actuators B: Chemical**. 129(2): 888-895.
- [9] Dai, M., et al. 2017. "Hierarchical assembly of α -Fe₂O₃ nanorods on multiwall carbon nanotubes as a high-performance sensing material for gas sensors." **ACS applied materials & interfaces**. 9(10): 8919-8928.
- [10] Muthukumar, P., et al. 2014. "Fe₂O₃/Carbon nanotube-based resistive sensors for the selective ammonia gas sensing." **Sensor letters**. 12(1): 17-23.
- [11] Andio, M. A., et al. 2012. "Comparison of gas sensor performance of SnO₂ nanostructures on microhotplate platforms." **Sensors and Actuators B: Chemical**. 165(1): 13-18.
- [12] Vuong, N. M., et al. 2016. "CuO-decorated ZnO hierarchical nanostructures as efficient and established sensing materials for H₂S gas sensors." **Scientific reports** 6: 26736.

- [13] Gupta, V. and T. A. Saleh (2011). "Syntheses of carbon nanotube-metal oxides composites; adsorption and photo-degradation." **Carbon Nanotubes-From Research to Applications**. 17: 295-312.
- [14] Jantharamatsakarn, K. and S. Chaisitsak. 2014. "Ferrocene-ethanol-mist CVD grown SWCNT films as transparent electrodes." **Procedia Engineering**. 93: 49-58.
- [15] Monitors, G. 2005. **Fundamentals of Combustible Gas Detection**.
- [16] Gas, L. 2013. "Lower and upper explosive limits for flammable gases and vapors (LEL/UEL)." **Matheson gas products**. 22.
- [17] Dimian, A. C., et al. 2014. Health, safety and environment. Computer Aided Chemical Engineering, Elsevier. 35: 649-678.
- [18] Aswal, D. K. and S. K. Gupta. 2007. **Science and technology of chemiresistor gas sensors**, Nova Publishers.
- [19] Bochenkov, V. and G. Sergeev. 2010. "Sensitivity, selectivity, and stability of gas-sensitive metal-oxide nanostructures." **Metal oxide nanostructures and their applications**. 3: 31-52.
- [20] Singh, S., et al. 2014. "Synthesis and characterization of CuO-SnO₂ nanocomposite and its application as liquefied petroleum gas sensor." **Materials Science in Semiconductor Processing**. 18: 88-96.
- [21] Srivastava, R. and B. Yadav. 2015. "Nanostructured ZnFe₂O₄ thick film as room temperature liquefied petroleum gas sensor." **Journal of Experimental Nanoscience**. 10(9): 703-717.
- [22] Joshi, S., et al. 2008. "Fabrication of n-CdTe/p-polyaniline heterojunction-based room temperature LPG sensor." **Sensors and Actuators B: Chemical**. 132(1): 349-355.
- [23] Mitra, P. and H. S. Maiti. 2004. "A wet-chemical process to form palladium oxide sensitizer layer on thin film zinc oxide based LPG sensor." **Sensors and Actuators B: Chemical**. 97(1): 49-58.
- [24] Eggins, B. R. 2008. **Chemical sensors and biosensors**, John Wiley & Sons.
- [25] Iijima, S. 1991. "Synthesis of carbon nanotubes." **nature**. 354(6348): 56-58.
- [26] Saito, Y., et al. (1997). "Field emission patterns from single-walled carbon nanotubes." **Japanese journal of applied physics**. 36(10A): L1340.
- [27] Cheng, H.-M., et al. 2001. "Hydrogen storage in carbon nanotubes." **Carbon**. 39(10): 1447-1454.

- [28] Jarvis, S. P., et al. 2000. "Local solvation shell measurement in water using a carbon nanotube probe." **The journal of physical chemistry B**. 104(26): 6091-6094.
- [29] Kong, J., et al. 2000. "Nanotube molecular wires as chemical sensors." **Science**. 287(5453): 622-625.
- [30] Ajayan, P. M., et al. 2000. "Single-walled carbon nanotube-polymer composites: strength and weakness." **Advanced Materials**. 12(10): 750-753.
- [31] Wang, C., et al. 2004. "Proton exchange membrane fuel cells with carbon nanotube based electrodes." **Nano Letters**. 4(2): 345-348.
- [32] Martins-Júnior, P., et al. 2013. "Carbon nanotubes: directions and perspectives in oral regenerative medicine." **Journal of dental research**. 92(7): 575-583.
- [33] Tilmaciu, C.-M. and M. C. Morris. 2015. "Carbon nanotube biosensors." **Frontiers in chemistry**. 3: 59.
- [34] Prasek, J., et al. 2011. "Methods for carbon nanotubes synthesis." **Journal of Materials Chemistry**. 21(40): 15872-15884.
- [35] Korotčenkov, G. S. 2014. *Handbook of Gas Sensor Materials: Properties, Advantages and Shortcomings for Applications. New Trends and Technologies*, Springer.
- [36] Wei, X., et al. 2011. "Thermal stability of carbon nanotubes probed by anchored tungsten nanoparticles." **Science and Technology of advanced Materials**. 12(4): 044605.
- [37] Xu, F., et al. 2010. "Thermal stability of carbon nanotubes." **Journal of thermal analysis and calorimetry**. 102(2): 785-791.
- [38] Peng, H., et al. 2000. "Smallest diameter carbon nanotubes." **Applied Physics Letters**. 77(18): 2831-2833.
- [39] Bom, D., et al. 2002. "Thermogravimetric analysis of the oxidation of multiwalled carbon nanotubes: evidence for the role of defect sites in carbon nanotube chemistry." **Nano Letters**. 2(6): 615-619.
- [40] Zhou, W., et al. 2001. "Structural characterization and diameter-dependent oxidative stability of single wall carbon nanotubes synthesized by the catalytic decomposition of CO." **Chemical Physics Letters**. 350(1-2): 6-14.
- [41] Ma, J. and J. N. Wang. 2008. "Purification of single-walled carbon nanotubes by a highly efficient and nondestructive approach." **Chemistry of Materials**. 20(9): 2895-2902.

- [42] Lekawa-Raus, A., et al. 2014. "Electrical properties of carbon nanotube based fibers and their future use in electrical wiring." **Advanced Functional Materials**. 24(24): 3661-3682.
- [43] Baughman, R. H., et al. 2002. "Carbon nanotubes--the route toward applications." **science**. 297(5582): 787-792.
- [44] Chen, R. J., et al. 2001. "Molecular photodesorption from single-walled carbon nanotubes." **Applied Physics Letters**. 79(14): 2258-2260.
- [45] Goldoni, A., et al. 2004. "Spectroscopic characterization of contaminants and interaction with gases in single-walled carbon nanotubes." **Carbon**. 42(10): 2099-2112.
- [46] Williams, K. A. and P. C. Eklund. 2000. "Monte Carlo simulations of H₂ physisorption in finite-diameter carbon nanotube ropes." **Chemical Physics Letters** .320(3-4): 352-358.
- [47] Chico, L., et al. 1998. "Carbon-nanotube-based quantum dot." **Physical review letters**. 81(6): 1278.
- [48] Kumar, S., et al. 2013. "Conductivity modulation of carbon nanotubes through hybridization with quantum dots and gold nanoparticles." **The European Physical Journal-Applied Physics**. 64(2).
- [49] Kerdcharoen, T. and C. Wongchoosuk. 2013. "Carbon nanotube and metal oxide hybrid materials for gas sensing." **Semiconductor Gas Sensors**, Elsevier: 386-407.
- [50] Mirabile Gattia, D., et al. 2006. "Arc-discharge synthesis of carbon nanohorns and multiwalled carbon nanotubes." **Materials science forum**, Trans Tech Publ.
- [51] Batani, D., et al. 2014. "Laser-ablation and induced nanoparticle synthesis." **Laser and Particle Beams**. 32(1): 1-7.
- [52] Dai, H., et al. 1996. "Single-wall nanotubes produced by metal-catalyzed disproportionation of carbon monoxide." **Chemical Physics Letters**. 260(3-4): 471-475.
- [53] Novoselova, I., et al. 2008. "Electrolytic synthesis of carbon nanotubes from carbon dioxide in molten salts and their characterization." **Physica E: Low-dimensional Systems and Nanostructures**. 40(7): 2231-2237.
- [54] Gogotsi, Y., et al. 2000. "Hydrothermal synthesis of multiwall carbon nanotubes." **Journal of Materials Research**. 15(12): 2591-2594.
- [55] Jeong, S.-H., et al. 2002. "Preparation of aligned carbon nanotubes with prescribed dimensions: template synthesis and sonication cutting approach." **Chemistry of Materials**. 14(4): 1859-1862.

- [56] Rafique, M. M. A. and J. Iqbal. 2011. "Production of carbon nanotubes by different routes-a review." **Journal of encapsulation and adsorption sciences.** 1(02): 29.
- [57] Jaaniso, R. and O. K. Tan. 2013. **Semiconductor gas sensors**, Elsevier.
- [58] Akbari, E., et al. 2014. "Analytical calculation of sensing parameters on carbon nanotube based gas sensors." **Sensors.** 14(3): 5502-5515.
- [59] Afrin, R. and N. Shah. 2015. "Room temperature gas sensors based on carboxyl and thiol functionalized carbon nanotubes buckypapers." **Diamond and Related Materials.** 60: 42-49.
- [60] Patil, D., et al. 2011. "Highly sensitive and selective LPG sensor based on α -Fe₂O₃ nanorods." **Sensors and Actuators B: Chemical.** 152(2): 299-306.
- [61] Patil, D., et al. (2011). "Highly sensitive and selective LPG sensor based on α -Fe₂O₃ nanorods." **Sensors and Actuators B: Chemical** 152(2): 299-306.
- [62] Ryabtsev, S., et al. 1999. "Application of semiconductor gas sensors for medical diagnostics." **Sensors and Actuators B: Chemical.** 59(1): 26-29.
- [63] Neri, G., et al. 2002. "CO and NO₂ sensing properties of doped-Fe₂O₃ thin films prepared by LPD." **Sensors and Actuators B: Chemical.** 82(1): 40-47.
- [64] Tang, H., et al. 2006. "A selective NH₃ gas sensor based on Fe₂O₃-ZnO nanocomposites at room temperature." **Sensors and Actuators B: Chemical.** 114(2): 910-915.
- [65] Jadhav, V. V., et al. 2013. "Hematite nanostructures: Morphology-mediated liquefied petroleum gas sensors." **Sensors and Actuators B: Chemical.** 188: 669-674.
- [66] Yang, X.-H., et al. 2017. Two-Step Fabrication of Porous α -Fe₂O₃@ δ -TiO₂ core-shell Nanostructures with Enhanced Photocatalytic Activity. **3rd Annual International Conference on Advanced Material Engineering (AME 2017)**, Atlantis Press.
- [67] Comini, E., et al. 2002. "Stable and highly sensitive gas sensors based on semiconducting oxide nanobelts." **Applied Physics Letters.** 81(10): 1869-1871.
- [68] Tan, Q., et al. 2015. "Acetone sensing properties of a gas sensor composed of carbon nanotubes doped with iron oxide nanopowder." **Sensors.** 15(11): 28502-28512.
- [69] Ranganathan, K., et al. 2016. "Hybrid gas sensing and transport properties of few-walled CNTs decorated with discrete SnO₂ nanoparticles." **Journal of nanoscience and nanotechnology.** 16(1): 1211-1215.

- [70] Li, Z., et al. 2015. "A fast response & recovery H₂S gas sensor based on α -Fe₂O₃ nanoparticles with ppb level detection limit." **Journal of hazardous materials**. 300: 167-174.
- [71] Li, Z., et al. 2019. "Advances in designs and mechanisms of semiconducting metal oxide nanostructures for high-precision gas sensors operated at room temperature." **Materials Horizons**. 6(3): 470-506.
- [72] Jung, D., et al. 2014. "Room-temperature gas sensor using carbon nanotube with cobalt oxides." **Sensors and Actuators B: Chemical**. 204: 596-601.
- [73] Yilbas, B. S., et al. 2019. **Self-Cleaning of Surfaces and Water Droplet Mobility**, Elsevier.
- [74] Ferdous, M. M., et al. 2014. "Design and fabrication of a simple cost effective spin coater for deposition of thin film." **Advances in Environmental Biology**. 8: 729-733.
- [75] Stern, K. H. 1996. **Metallurgical and ceramic protective coatings**, Springer Science & Business Media.
- [76] Burgelman, M. 1998. Thin film solar cells by screen printing technology. **Proceedings of The Workshop Micro technology and Thermal Problems in Electronics**, Citeseer.
- [77] Wei, B.-Y., et al. 2004. "A novel SnO₂ gas sensor doped with carbon nanotubes operating at room temperature." **Sensors and Actuators B: Chemical**. 101(1-2): 81-89.
- [78] Chen, Y., et al. 2006. "The enhanced ethanol sensing properties of multi-walled carbon nanotubes/SnO₂ core/shell nanostructures." **Nanotechnology**. 17(12): 3012.
- [79] Chiu, P., et al. 2003. "Temperature dependence of conductance character in nanotube peapods." **Applied Physics A**. 76(4): 463-467.
- [80] Mao, S., et al. 2012. "Ultrafast hydrogen sensing through hybrids of semiconducting single-walled carbon nanotubes and tin oxide nanocrystals." **Nanoscale**. 4(4): 1275-1279.
- [81] Marichy, C., et al. 2013. "Tin dioxide-carbon heterostructures applied to gas sensing: structure-dependent properties and general sensing mechanism." **The Journal of Physical Chemistry C**. 117(38): 19729-19739.
- [82] Hoa, N. D., et al. 2009. "Nanowire structured SnO_x-SWNT composites: high performance sensor for NO_x detection." **Sensors and Actuators B: Chemical**. 142(1): 253-259.

- [83] Fujita, H. 2003. **Micromachines as tools for nanotechnology**, Springer Science & Business Media.
- [84] Dresselhaus, M. S., et al. 2010. "Perspectives on carbon nanotubes and graphene Raman spectroscopy." **Nano letters**. 10(3): 751-758.
- [85] Graupner, R. 2007. "Raman spectroscopy of covalently functionalized single-wall carbon nanotubes." **Journal of Raman Spectroscopy: An International Journal for Original Work in all Aspects of Raman Spectroscopy, Including Higher Order Processes, and also Brillouin and Rayleigh Scattering**. 38(6): 673-683.
- [86] Dresselhaus, M. S., et al. 2005. "Raman spectroscopy of carbon nanotubes." **Physics reports**. 409(2): 47-99.
- [87] Briggs, D. 1981. Handbook of X-ray Photoelectron Spectroscopy CD Wanger, WM Riggs, LE Davis, JF Moulder and GE Muilenberg Perkin-Elmer Corp., Physical Electronics Division, Eden Prairie, Minnesota, USA, 1979. 190 pp. \$195." **Surface and Interface Analysis**. 3(4): v-v.
- [88] Raja, P. and A. Barron. 2019. "Physical methods in chemistry and nano science." OpenStax CNX.
- [89] Vyazovkin, S. 2002. "Thermogravimetric analysis." **Characterization of Materials**: 1-12.
- [90] Balouria, V., et al. 2013. "Nano-crystalline Fe₂O₃ thin films for ppm level detection of H₂S." **Sensors and Actuators B: Chemical**. 181: 471-478.
- [91] Blagov, E., et al. 2007. "van der Waals interaction between a microparticle and a single-walled carbon nanotube." **Physical review B**. 75(23): 235413.
- [92] Song, H., et al. 2008. "A simple approach to the fabrication of transparent single-wall carbon nanotube films of high electrical and optical performance." **Journal of the Korean Physical Society**. 53(4): 2111-2114.
- [93] Vuong, N. M., et al. 2014. "Ni₂O₃-decorated SnO₂ particulate films for methane gas sensors." **Sensors and Actuators B: Chemical**. 192: 327-333.
- [94] Matrab, T., et al. 2006. "Atom transfer radical polymerization (ATRP) initiated by aryl diazonium salts: a new route for surface modification of multiwalled carbon nanotubes by tethered polymer chains." **Colloids and Surfaces A: Physicochemical and Engineering Aspects**. 287(1-3): 217-221.
- [95] Leedahl, B., et al. 2014. "Structural defects induced by Fe-ion implantation in TiO₂." **Journal of Applied Physics**. 115(5): 053711.
- [96] Bonnet, F., et al. 2002. "Study of the oxide/carbide transition on iron surfaces during catalytic coke formation." **Surface and Interface Analysis: An**

- International Journal devoted to the development and application of techniques for the analysis of surfaces, interfaces and thin films. 34(1): 418-422.
- [97] Fujii, T., et al. 1999. "In situ XPS analysis of various iron oxide films grown by NO₂-assisted molecular-beam epitaxy." **Physical review B**. 59(4): 3195.
- [98] Mekki, A., et al. 1996. "An XPS study of iron sodium silicate glass surfaces." **Journal of non-crystalline solids**. 208(3): 267-276.
- [99] Barnett, C. J., et al. 2018. "Spatial and contamination-dependent electrical properties of carbon nanotubes." **Nano letters**. 18(2): 695-700.
- [100] Maria, K. H. and T. Mieno. 2017. "Production and properties of carbon nanotube/cellulose composite paper." **Journal of Nanomaterials**. 2017.
- [101] Wu, C., et al. 2009. "The effect of the catalyst metals on the thermal-oxidative stability of single-walled carbon nanotubes." **Physica E: Low-dimensional Systems and Nanostructures**. 41(8): 1591-1595.
- [102] Harutyunyan, A. R., et al. 2002. "Purification of single-wall carbon nanotubes by selective microwave heating of catalyst particles." **The journal of physical chemistry B**. 106(34): 8671-8675.
- [103] Chen, L.-T., et al. 2013. "Purification and dispersion of single-walled carbon nanotubes for transparent conducting films." **Integrated Ferroelectrics**. 145(1): 80-87.
- [104] Yahyazadeh, A., et al. 2019. "An investigation into the role of substrates in the physical and electrochemical properties of carbon nanotubes prepared by chemical vapor deposition." **Physica B: Condensed Matter**.
- [105] Furtado, C., et al. 2004. "Debundling and dissolution of single-walled carbon nanotubes in amide solvents." **Journal of the American Chemical Society**. 126(19): 6095-6105.
- [106] Lübbe, M., et al. 2010. "Identification of iron oxide phases in thin films grown on Al₂O₃ (0001) by Raman spectroscopy and X-ray diffraction." **Surface science**. 604(7): 679-685.
- [107] Balouria, V., et al. 2013. "Nano-crystalline Fe₂O₃ thin films for ppm level detection of H₂S." **Sensors and Actuators B: Chemical**. 181: 471-478.
- [108] Chaisitsak, S. 2011. "Nanocrystalline SnO₂: F thin films for liquid petroleum gas sensors." **Sensors** 11(7): 7127-7140.

- [109] Tavakkoli, M., et al. 2016. "Maghemite nanoparticles decorated on carbon nanotubes as efficient electrocatalysts for the oxygen evolution reaction." **Journal of Materials Chemistry A**. 4(14): 5216-5222.
- [110] Roy, R., et al. 2005. "Room temperature sensor based on carbon nanotubes and nanofibres for methane detection." **Vacuum**. 77(3): 223-229.
- [111] Ganji, M. D., et al. 2010. "Theoretical investigation of methane adsorption onto boron nitride and carbon nanotubes." **Science and Technology of Advanced Materials**. 11(4): 045001.
- [112] Suehiro, J., et al. 2006. "Schottky-type response of carbon nanotube NO₂ gas sensor fabricated onto aluminum electrodes by dielectrophoresis." **Sensors and Actuators B: Chemical**. 114(2): 943-949.
- [113] Donato, N., et al. 2011. "Novel carbon nanotubes-based hybrid composites for sensing applications." **Carbon nanotubes-From Research to Applications**. 14: 229-242.
- [114] Reddy, M. S. B., et al. 2019. "MgO@CeO₂ chemiresistive flexible sensor for room temperature LPG detection." **Journal of Materials Science: Materials in Electronics**. 30(18): 17295-17302.
- [115] Dai, Z., et al. 2015. "Highly reversible switching from P-to N-type NO₂ sensing in a monolayer Fe₂O₃ inverse opal film and the associated P-N transition phase diagram." **Journal of Materials Chemistry A**. 3(7): 3372-3381.
- [116] Bulakhe, R., et al. 2013. "Fabrication and performance of polypyrrole (Ppy)/TiO₂ heterojunction for room temperature operated LPG sensor." **Sensors and Actuators B: Chemical**. 181: 417-423.
- [117] Barkade, S., et al. 2013. "Ultrasound assisted synthesis of polythiophene/SnO₂ hybrid nanolatex particles for LPG sensing." **Chemical Engineering and Processing: Process Intensification**. 74: 115-123.
- [118] Singh, S., et al. 2014. "Synthesis and characterization of CuO-SnO₂ nanocomposite and its application as liquefied petroleum gas sensor." **Materials Science in Semiconductor Processing**. 18: 88-96.
- [119] Sen, T., et al. 2014. "Polyaniline/ γ -Fe₂O₃ nanocomposite for room temperature LPG sensing." **Sensors and Actuators B: Chemical**. 190: 120-126.
- [120] Gurav, K., et al. 2014. "Cu₂ZnSnS₄ (CZTS)-based room temperature liquefied petroleum gas (LPG) sensor." **Sensors and Actuators B: Chemical**. 190: 408-413.

- [121] Patil, S., et al. 2016. "Liquefied petroleum gas (LPG) sensing using spray deposited $\text{Cu}_2\text{ZnSnS}_4$ thin film." **Journal of Analytical and Applied Pyrolysis**. 117: 310-316.
- [122] Singh, M., et al. 2017. "Synthesis and characterization of perovskite barium titanate thin film and its application as LPG sensor." **Sensors and Actuators B: Chemical**. 241: 1170-1178.
- [123] ATOMIC FORCE MICROSCOPE AFM XE-100 from Park Systems.
[Online]. Available: <http://www.phys-iasi.ro/en>
- [124] Raman spectroscopy (Renishaw in Via Reflex).
[Online]. Available :<https://www.renishaw.com>.
- [125] Pyris 1 TGA Thermogravimetric Analyzer.
[Online]. Available :<https://www.perkinelmer.com>
- [126] Photoelectric Effect | Einstein's Equation.
[Online]. Available <https://notesclasses.com>
- [127] X-ray photoelectron spectroscopy. [Online]. Available : <http://thep-center.org>
- [128] Thai Microelectronics Center. FE-SEM [Online]. Available : <http://thep-center.org>

Appendix A

Nanoparticle measurements

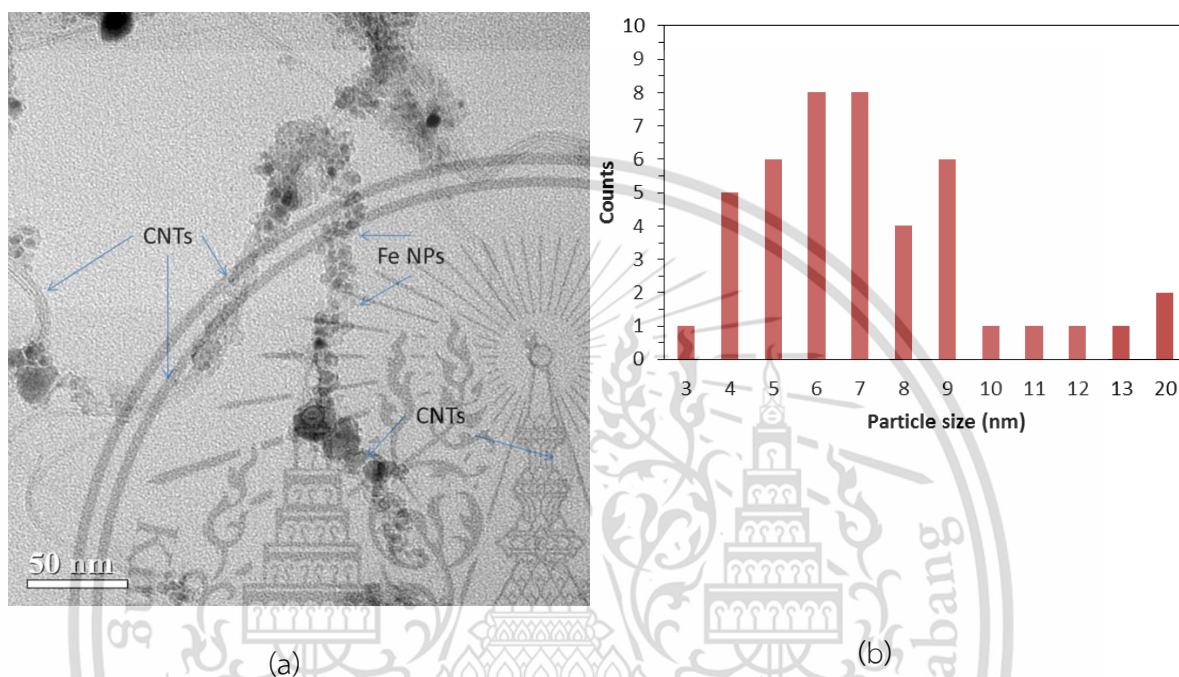
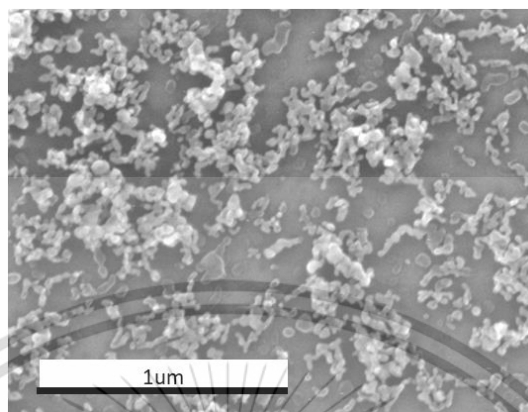


Figure A.1 (a) TEM images represent iron nanoparticles (Fe NPs) at surface of CNTs. (b) Particle-size distribution of the Fe NPs performed by measuring 45 individual NPs on the TEM images.

Figure A.1 (a) depicts the TEM image of the as-grown films or Fe-CNT films. This film consists of randomly oriented entangled CNTs and nanoparticles. Morphology of films depicts that the small-diameter CNTs were coated with nanoparticles, and some of these CNTs were coated with nanoparticle clusters. These nanoparticles (NPs) were metallic iron (using XPS). An estimation of the distribution of Fe NPs' sizes performed by measuring each NP obtained from TEM images yielded an average particle size of ~ 7.33 nm, as shown in Figure A.1 (b).

Appendix B



(c)

Figure B. 1 FE-SEM image of as-grown films annealed in air at 550°C or the purified Fe_2O_3 .

Figure B. 1 demonstrates that the morphology of the purified Fe_2O_3 , which obtained via the annealing in air of as-grown films (Fe-CNT) at 550°C. At this temperature, the CNTs were removed by air oxidation.

Appendix C

SURVEY SCAN

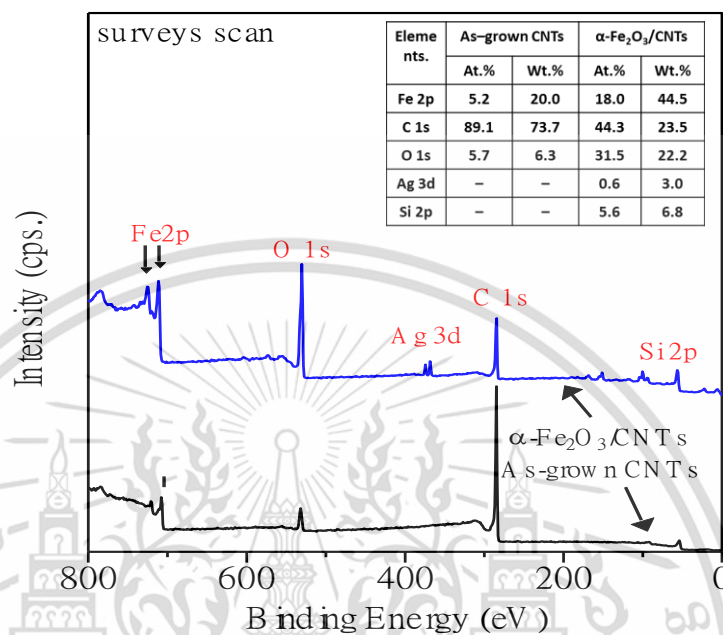


Figure C. 1 XPS survey scan of as-grown Fe-CNT and Fe₂O₃-CNT films. The inset in figure shows the atomic percent (At %) and weight percent (Wt %) of as-grown Fe-CNT and Fe₂O₃-CNT films.

Figure C. 1 demonstrates that the XPS survey spectrum of both as-grown Fe/CNTs and Fe₂O₃-CNT films were carbon (C 1s; ~284 eV), oxygen (O 1s; ~530 eV), silicon (Si 2p; ~100 eV), silver (Ag 3d; ~370 eV), and iron (Fe 2p; ~700 eV). In Fe₂O₃-CNT thin films, peak at 100 eV is observed and corresponds to silicon of silicon substrate; this is because of the ultra-thin films of the Fe₂O₃-CNTs. In addition, the atomic percent (At %) table (see the inset table) demonstrated that O:Fe atomic ratio on the Fe₂O₃-CNT films was close to 2:3, which is probably Fe₂O₃.

Appendix D

LIST OF PUBLICATION

1. B. Chaitongrat and S. Chaisitsak, "Fast-LPG sensors at room temperature by α - $\text{Fe}_2\text{O}_3/\text{CNT}$ nanocomposite thin films," *Journal of Nanomaterials*, vol. 2018, 2018.
2. B. Chaitongrat and S. Chaisitsak, "Hybrid $\text{Fe}_2\text{O}_3/\text{CNT}$ Thin Films for Gas Sensor Applications," in *2018 International Conference on Engineering, Applied Sciences, and Technology (ICEAST)*, 2018, pp. 1-4.
3. B. Chaitongrat and S. Chaisitsak, "Novel Preparation and Characterization of $\text{Fe}_2\text{O}_3/\text{CNT}$ Thin Films for Flammable Gas Sensors," in *Materials Science Forum*, 2019, pp. 47-51.



AUTHOR BIOGRAPHY

Name: Miss. Buaworn Chaitongrat

Date of Birth: August 11, 1981

Educational Background: B.Sc. (Physics), Department of Physics, Faculty of Science, Srinakarinwirot Prasanmitt, Bangkok, Thailand, 2000-2003
M. Eng. (Microelectronics Engineering), Department of Electronics Engineering, Faculty of Engineering, King Mongkut's Institute of Technology Ladkrabang, Bangkok, Thailand, 2005-2007

Working Experience:
2009 -present Lecturer at Udon Thani Rajabhat University.

